A Diesel-Fuelled Solid Oxide Fuel Cell (SOFC) 1 kW Generator: System and Component Studies

by

Harsh Dhingra

A thesis submitted to the Department of Chemical Engineering

in conformity with the requirements for

the degree of Masters of Applied Science

Queen's University

Kingston, Ontario, Canada

(April, 2012)

Abstract

A steady-state simulation of a diesel-fuelled SOFC system was developed using a process simulation software package (VMGSim™). The system was studied by conducting a sensitivity analysis of six independent variables (steam to carbon ratio, oxygen to carbon ratio, fuel utilization, air utilization, reformer pre-heater approach temperature and cathode temperature to the SOFC) and their effect on three response variables (net system efficiency, stack efficiency, system exhaust temperature). The steam to carbon ratio, fuel utilization and air utilization were the most influential independent variables and thus affected the greatest change in the performance metrics. Secondly, a multi-variable study was carried out on the most influential variables and constrained optima for the efficiencies (45% net system, 47% stack) and system exhaust temperature (78 ^{o}C) were obtained.

For the second part of this work, a steam reforming heat-exchange reactor was modeled using COMSOL™. The reactor performance was assessed on the basis of selectivity and residence time for a given conversion. Both the kinetic models of Parmar *et al.* (2010) and Shi *et al.* (2009) for catalytic diesel steam reforming were applied and compared. Differences in performance were attributed to differences in the catalyst support and the reaction mechanisms used for deriving the reforming rate expressions. Finally, a proof of concept multi-scale modeling and design tool was developed by integrating the CFD model with the process simulation. Two-way communication between four different software components; COMSOL™, VMGSim™, Matlab™ and Microsoft Excel™ was achieved.

Acknowledgements

I would like to thank the following people who provided me with the support and information needed to complete this project: My supervisor, Dr. Brant A. Peppley for supporting, guiding and encouraging me all the way through; Adam Tuck from the National Research Council Institute for Fuel Cell Innovation (NRC-IFCI) for the productive discussions and sharing of information on the 1 kW biogas system developed in Vancouver; FCRC colleagues Rajesh Parmar (Ph.D.), Mayur Mundhwa (Ph.D.) and Trevor Wartman (M.Sc.) for helping me with developing transport and system models and through some difficult periods; all the colleagues with whom I interacted with during my studies at Queen's and my old room-mate, Richard, who always had something interesting to talk about and kept me going. I would also like to thank NRC-IFCI and the SOFC Canada NSERC Strategic Research Network for their continued support.

Lastly, I would like to thank my parents, grand-mother, my sister and my brother-in-law for their advice and support, and my year and a half old nephew who reminds me of the beauty of life and what it has to offer.

Table of Contents

List of Figures

List of Tables

Nomenclature

c	concentration	[mol/m^3]
C	heat capacity	[kJ/kg.K]
D	diffusion coefficient	[m^2/s]
E_{act}	activation energy	[J/mol]
F	faraday constant	[C/mol]
h	half-height	[m]
H	enthalpy	[kJ/kmol]
i	current density	[A/m^2]
i_o	exchange current density	[A/m^2]
k	thermal conductivity	[W/m.K]
K	equilibrium constant	
LHV_{CO}	lower heating value CO at anode feed	[kJ/kg]
LHV_{CO_2}	lower heating value CO_2 at anode feed	[kJ/kg]
LHV_{CH_4}	lower heating value CH_4 at anode feed	[kJ/kg]
LHV_{fuelin}	lower heating value fuel feed to SOFC system	[kJ/kg]
$LHV_{fueltoref}$	lower heating value fuel feed to reformer	[kJ/kg]
m_{fuelin}	mass flow rate fuel feed to SOFC system	[kg/s]
$m_{fueltoref}$	mass flow rate fuel feed to reformer	[kg/s]
m_{CO}	mass flow rate CO at anode feed	[kg/s]
m_{CO_2}	mass flow rate CO_2 at anode feed	[kg/s]

m_{CH_4}	mass flow rate CH_4 at anode feed	[kg/s]
n_{CO}	molar flow rate CO at anode feed	[kgmol/s]
n_{CO_2}	molar flow rate CO_2 at anode feed	[kgmol/s]
n_{H_2O}	molar flow rate H_2O at anode feed	[kgmol/s]
n_{H_2}	molar flow rate H_2 at anode feed	[kgmol/s]
n_{CH_4}	molar flow rate CH_4 at anode feed	[kgmol/s]
n_{O_2}	molar flow rate O_2 at anode feed	[kgmol/s]
n_{N_2}	molar flow rate N_2 at anode feed	[kgmol/s]
n_c	weighted average number of carbon atoms per hydrocarbon molecule in diesel feed	
n_e	number of electrons	
n_h	theoretical number of moles of hydrogen produced per mol of hydrocarbon	
n_{cells}	number of cells in SOFC stack	
N	momentum, molar or heat flux	[N/m^2], [$mol/m^2.s$], [$J/m^2.s$]
P	pressure	[Pa]
Q	heat	[kW]
r	rate of reaction	[$mol/m^3.s$]
R	ideal gas constant	[kJ/kmol.K]
R_p	pore radius	[m]

$S\ to\ C$	steam to carbon ratio	
t	layer thickness	[m]
T	temperature	[K]
u	velocity	[m/s]
U_f	fuel utilization in SOFC	
U_a	air utilization in SOFC	
v	diffusion volume	[m^3]
V	voltage	[V]
wt	weight fraction	
W	power	[kW]
x	axial coordinate	
X	mole fraction	
y	transverse coordinate	

Greek Symbols

ε	extent of reaction	[kmol/s]
ρ	density	[kg/m^3]
δ_{cat}	catalyst thickness	
μ	dynamic viscosity	[kg/m.s]
η	effectiveness factor	
κ	permeability	[m^2/s]
ϕ	porosity	

Ω	resistance	[ohm m^2]

Subscripts

act	activation
a	anode
b	boundary
c	cathode
$centre$	channel centre
$COMB$	combustion
$conc$	concentration polarization
eff	effective
$elec$	electric
fg	flue-gas channel
i, j	component (eg. CO, CO_2, H_2)
in	input
k	total number of components
mix	mixture
$parasitic$	SOFC system balance of plant components
o	initial value
out	output
p	constant pressure
r	reforming channel

ref	reference
rxn	reaction
s	catalyst phase
$SOFC$	SOFC
$wall$	plate wall
WGS	water-gas shift
x	axial coordinate
y	transverse coordinate

List of Acronyms

AOGR	Anode Off-Gas Recirculation
APU	Auxiliary Power Unit
ATR	Autothermal Reformer/ing
BoP	Balance of Plant
CFD	Computational Fluid Dynamics
CHP	Combined Heat and Power
CPOX	Catalytic Partial Oxidation
CPR	Catalytic Plate Reactor
DIR	Direct Internal Reforming
DOE	Department of Energy
FCRC	Fuel Cell Research Centre
GHG	Greenhouse Gas
GHSV	Gas Hourly Space Velocity
HC	Hydrocarbon
IIR	Indirect Internal Reforming
LHV	Lower Heating Value
NEDO	New Energy and Industrial Technology Development Organization
NETL	National Energy Technology Laboratory
NOx	Mono-Nitrogen Oxides
O2 to C	Oxygen to Carbon

OCV	Open-Circuit Voltage
PAFC	Phosphoric Acid Fuel Cell
PEM	Polymer Electrolyte Membrane
REE	Rare Earth Elements
S to C	Steam to Carbon
SCFV	Stabilized Cool-Flame Vaporizer
SECA	Solid State Energy Conversion Alliance
SI	Sensitivity Index
SOFC	Solid Oxide Fuel Cell
SOFCC	SOFC Canada
SOx	Mono-Sulfur Oxides
SR	Steam Reformer/ing
TGC	Tail-Gas Combustor
TPB	Triple Phase Boundary
TPOX	Thermal Partial Oxidation
WGS	Water-Gas Shift
YSZ	Yttria-Stabilized Zirconia

Chapter 1

Introduction

1.1 Background

The concept of electrical energy generation directly from chemical energy by electrochemical reactions is not a new one. Electrochemical cells existed as far back as 247 B.C. – 228 A.D., or roughly 2000 years ago. This was thought to be the age of the so called Baghdad Battery discovered in Iraq. The object was an oval jar containing a rolled up copper sheet and an iron rod held in place at the center with asphalt. Traces of corrosion on the copper suggested that the jar was once filled with an acidic agent such as lemon juice or possibly vinegar acting as a liquid electrolyte [1]. The battery falls under the category of electrochemical cells and energy storage devices. It is, however, different from a fuel cell. A fuel cell, in comparison to a battery, is an open system and an energy conversion device that requires a continuous supply of fuel and oxygen to run. It can continue to produce electricity as long as the input reactants are supplied [2].

The first widely accepted prototype of a fuel cell was developed by Sir William Grove in the 1830's. Sir William Grove initially conducted various electrolysis experiments to decompose water into hydrogen and oxygen using an external power source. He eventually foresaw the possibility of the reverse reaction occurring and was able to

observe a potential difference preserved between the electrodes after disconnecting the external power source [3].

The Phosphoric Acid Fuel Cell (PAFC), using a highly concentrated liquid phosphoric acid electrolyte, was the first of its kind to be commercialized on a large scale (200 kW) as part of a Combined Heat and Power (CHP) system developed by United Technologies Corporation [4]. With an operating temperature range between 180 and 200 ^{o}C, the waste heat can be used to generate steam, pre-heat feed streams and for space and water heating, with demonstrated electrical efficiencies >35% and Combined Heat and Power (CHP) efficiencies >80% based on the Lower Heating Value (LHV) of natural gas. Small levels of CO in the fuel (>0.5 vol%) supplied to the anode, however, can be poisonous and requires processing of the fuel using a water gas shift reactor to convert CO into H_2 and CO_2 [4-5].

In contrast, SOFC systems operate at temperature ranging from 600 to 1000 ^{o}C, producing higher quality waste heat for use in CHP processes. With a solid electrolyte, the cell can be cast into various shapes to improve power densities, reduce current paths and additionally alleviate corrosion problems in the cell [4]. More importantly, the system is fuel flexible; that is to say it does not rely heavily on the availability of a highly pure hydrogen stream entering the stack and CO can be directly utilized as a fuel. This eliminates the need for additional fuel processing components in the system. Electrical efficiencies greater than 50% and CHP efficiencies greater than 80% have been demonstrated [4, 6-7], depending on the fuel used. Figure 1.1-1 depicts the general

flow of ions and electrons in a single SOFC cell unit consisting of an anode and cathode electrode, a solid ceramic electrolyte (ZrO_2 stabilized Y_2O_3 or YSZ) and interconnects connected to a load.

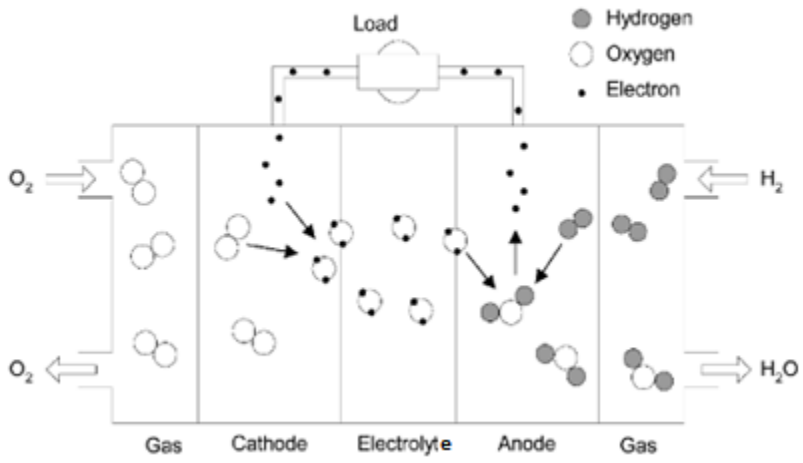

Figure 1.1-1: Schematic of Transport Processes in an SOFC [8]

Singhal (2005) provides a detailed description of the process. In the schematic above, oxygen at the cathode is reduced to $2O^{2-}$ by accepting 4 electrons from an external circuit. At the electrolyte layer, in the fluorite structure of the crystal, some of the Zr^{4+} ions are replaced by Y^{3+} ions. The lower valency of yttrium (3+) results in vacancies in the lattice structure which allows movement of O^{2-} ions, provided the operation is at sufficiency high temperatures. The anions are selectively transported through the electrolyte where the half-cell reaction with hydrogen at the anode side produces two H_2O molecules and four electrons that are transported back to the cathode via the external circuit. The half-cell reactions occur at the Triple Phase Boundary (TPB) between the gas phase, electrode and electrolyte layers at a microstructure level; hence, the fuel cell efficiency, and consequently the net system efficiency, is limited by

the reaction activation energies, mass transport resistance of reactants to the TPB and ohmic losses from the transport resistance of electrons and ions [9].

Some of the current SOFC development has revolved around reducing cost of cell components and improving mechanical stability. A second development effort has been in exploring sulphur and coke tolerant anode materials for utilizing untreated fossil fuels. Testing at a stack level is being done to ensure minimal voltage degradation for long duration operation and for multiple redox and thermal cycles [7].

Remote Power Applications for Diesel-Fuelled SOFC Systems

In many remote parts of Canada, there is a great environmental concern for use of conventional diesel generators for electricity generation. In addition to producing un-burnt HCs, NOX, SOX and carbon particle emissions, diesel engines cause noise and vibration and are also difficult to start up in cold weather conditions. There are currently about **600,000 off-grid sites for diesel** in Canada alone, in environmentally sensitive areas in the far North [10]. According to the Canadian Renewable Energy Guide (1999) [11], the Northwest Territories Power Corporation sells approximately 450 GWh of electricity annually, about half of which is provided by hydropower developments in the vicinity of the Great Slave Lake. The remaining is accounted for by diesel generators throughout the region. Private installations located at mines, telecommunication stations and remote hunting and fishing camps account for an additional 120 GWh of electricity on a yearly basis. Overall, this amounts to a total of

350 GWh, or 60% of the total electricity supply identified, as being generated from diesel fuel.

The availability of diesel, the peak price of $1.2 per kWh for electricity generation in remote areas and the extreme sensitivity of surrounding ecosystems provides motivation to replace the existing technology with SOFC systems [10]. Many of the existing generators in the northwest are built around communities and therefore residents have complained about the continuous hum. By comparison, a SOFC based system would be relatively noise-free and furthermore significantly reduce the environmental impact of using heavy hydrocarbon fuels.

1.2 Overview of Fuel Cell Systems

In addition to the fuel cell stack, practical fuel cell systems require Balance of Plant (BoP) components to ensure efficient and safe operation. The stack and BoP together form the fuel cell system [4]. Individual stack designs and fuel types might require slightly different unit operations for BoP components; however, most fuel cell systems in general consist of certain key operations. The set of operations required for any fuel cell system are highlighted by Figure 1.2-1.

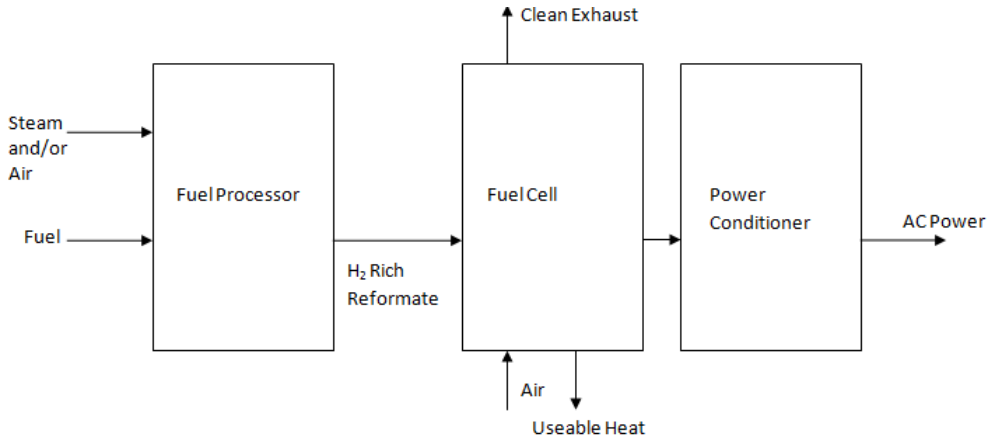

Figure 1.2-1: Key Constituents of a Fuel Cell System [4]

The fuel must first be processed prior to entering the fuel cell stack. Examples of processing steps include desulphurization, reforming using steam to produce the fuel mixture that will be directly consumed at the stack anode, and shift reactors where CO is reacted with steam to produce additional H_2. Shift reactors are especially important for low temperature fuel cells where CO species acts as a poison to the cell. In the fuel cell stack, the fuel consumed from the electrochemical reaction generates a power output based on the stack current and voltage. The fuel consumed directly in the stack is most commonly H_2. In the case of high-temperature fuel cells, however, direct oxidation of CH_4 and CO is also possible at the stack anode. This reduces fuel processing requirements upstream of the stack. The third major fuel cell subsystem is the power conditioning unit. The output from the stack represents a variable DC voltage that is not directly useable in conventional grid applications. It therefore must be converted to an AC output. In addition, the system also requires air, fuel and water management using compressors, blowers, pumps and air filters. The management of water is especially

important in low-temperature fuel cell systems, where water is present in the fuel cell in both liquid and vapor phase. For efficient systems considering both environmental and capital costs, careful design of the heat exchanger network is critical to ensure proper thermal management [4]. A proper process control scheme is also required in order to maintain the desired operating conditions. Important control variables in a fuel cell system are the flow of reactants (fuel, air and water) and also the stack temperature. Precise control of the process variables is critical to the viability and robustness of fuel cell systems [12].

1.2.1 Fuel Processing and Reformers

Fuel processing is a technique for converting hydrocarbon, alcohol or oxygenate fuels into a hydrogen-rich product stream that can be fed directly to the fuel cell anode. The key component of most fuel processors is the reformer operation. The three modes of reforming that are commonly employed in fuel cell systems are Steam Reforming (SR), Catalytic Partial Oxidation (CPOX) and Autothermal Reforming (ATR).

Steam Reforming (SR)

Approximately 50 million tons per year of hydrogen is produced worldwide from all sources. A large amount of the hydrogen generated comes from reacting steam with methane from natural gas. The hydrogen produced from SR is adjusted by controlling the Steam to Carbon (S to C) ratio of the fuel feed. For complex fuels with numerous hydrocarbons, the S to C is determined based on the average number of carbon atoms in the fuel.

The reforming reaction is strongly endothermic, and the heat to drive the reaction must be provided externally by combustion of additional fossil fuels. The reaction between steam and hydrocarbons (1.2.1) results in the formation of carbon oxides (CO, CO_2) and hydrogen.

$$Fuel\ (C_aH_b) + Steam \rightarrow Carbon\ Oxides + Hydrogen \quad (1.2.1)$$

Catalytic Partial Oxidation (CPOX)

CPOX is an alternative to SR, where a partial or substochiometric oxidation of the fuel produces primarily hydrogen and CO and small amounts of CO_2 (1.2.2). The amount of hydrogen produced is adjusted by controlling the air to fuel ratio. The process produces less hydrogen per unit of fuel than SR. A major benefit of using CPOX is the milliseconds residence time over which the reaction occurs compared to seconds for SR. The fast kinetics allows for the development of compact reactors for small-scale systems. CPOX in addition operates without the presence of steam. This eliminates the need for energy consuming water evaporation processes in the system.

$$Fuel\ (C_aH_b) + \ Air \rightarrow Carbon\ Oxides + Hydrogen + Nitrogen \quad (1.2.2)$$

Autothermal Reforming (ATR)

ATR combines the exothermic CPOX and endothermic SR reactions to effectively balance heat flows. The heat flows in an ATR are controlled by appropriately adjusting the flows of fuel, steam and air, or the S to C and Oxygen to Carbon ratio (O_2 to C). Carbon oxides, steam and hydrogen are the main reaction products (1.2.3). The hydrogen production per unit of fuel is lower than SR and greater than CPOX. The added benefit of steam is

that it reduces coke formation. The overall kinetics of the reaction is also sufficiently fast for the development of scalable, flexible reactors [13-14].

$$Fuel\ (C_aH_b) + \ Air + H_2O \rightarrow Carbon\ Oxides + \ Hydrogen + Nitrogen \quad (1.2.3)$$

1.3 Stationary SOFC CHP Generation Drivers and Barriers

Conventional small generators powered by internal combustion engines produce electricity at a cost greater than five times that from the grid and additionally result in the release of harmful pollutants and noise from vibration. A fuel cell based system must demonstrate longevity, reliability, low maintenance and an electrical energy cost below or equal to the cost of using the electricity grid in order to be successful as a commercial product [15]. The sections below present some of the technological and economic drivers and barriers that currently exist for SOFC based CHP systems.

1.3.1 Technological Drivers and Barriers

There are no moving parts in an SOFC and therefore less vibration and noise. The operating temperature of a SOFC provides high quality heat for reforming of the fuel for the anode. This results in improved thermal integration through regenerative heat recovery from the SOFC stack. The excess heat can be used in residential systems for providing hot water and space heating.

Fuel cells are generally more efficient than combustion engines [16]. SOFCs have a high fuel to electricity conversion between 45 and 65%. The total SOFC system efficiency

including recovery of high-quality waste heat can exceed 85% [17].

SOFCs have the longest continuous development period among all fuel cells, starting in the 1950's. New materials development for SOFCs to drive down costs, material durability and the lifetime of the stack has been an important technological driver. Some of the focal points have been in the development of new sulphur and coke tolerant anodes, metal-supported cells for improved fabrication costs and durability as well as robust interconnects and seals [4].

A SOFC powered generator, in comparison to conventional combustion-engine powered generators, produces only steam as a product (for a pure H_2 feed to the anode) with minimal CO_2 emissions in the exhaust. Hawkes *et al.* (2007) discuss that, based on a 1 kW SOFC micro-CHP in a UK dwelling, CO_2 emissions reduction on the order of 800 kg per dwelling per year could be expected in comparison to the case where electricity is supplied via the grid and heating is supplied via burning natural gas in a condensing boiler. Significant additional Greenhouse Gas (GHG) emission reductions can be achieved using an integrated SOFC CHP system compared to electricity produced at centralized power stations. The waste heat from the SOFC system can also displace the need for additional natural gas [18]. Furthermore, if a severe natural event were to occur resulting in a catastrophic failure of grid power, the level of social disruption would likely be far greater than if decentralized power systems were in common use. The use of decentralized SOFC CHP power generation

systems as alternative energy sources would also aid in the development of smart grid technology. In a smart grid system, SOFCs would provide a portion of the electricity in a residential or commercial setting and the remaining would be supplied from the grid. A portion of the electricity could alternatively be sold back to the grid. This would reduce costs for the consumer, improve the reliability of electricity supply and reduce peak demands from the centralized grid [19].

According to Sammes *et al.* (2000), applications which will drive SOFCs towards market entry include those which require a premium [15]. Such applications include those that require high power quality including servers, data processors or power generation applications for remote locations such as forestry, mining and agriculture, where power delivery is scarce such as in Northern Canada.

The technology for SOFCs has long been promising. One major problem yet to be overcome, however, is the limited lifetime of the SOFC stack. Mismatches between thermal expansion coefficients of materials at high SOFC operation temperatures result in thermal stresses. These can eventually lead to mechanical failure of components at their interfaces and limit the lifetime of the stack to approximately five years at full-load with reference to 2005 technology [20]. The future direction is aimed towards fabrication of low temperature SOFCs below 650 ^{o}C [21].

1.3.2 Political and Commercial Drivers and Barriers

The social and economic costs associated with pollution and energy inefficiency are providing political motivation for incentives and taxation to encourage the use of clean energy efficient technologies. The countries from the Organization of Economic Co-operation and Development currently tax fuels based on their carbon content to represent the social and environmental costs. A carbon tax could effectively account for the release of green-house gases to the atmosphere by any technology or industrial process and would create an environment in which fuel cells could thrive [15].

New employment opportunities would be generated with the commercialization of fuel cells. The effect of decentralization from the electricity grid would in addition help avoid fluctuations in electricity prices. The fuel flexibility of SOFCs provides a key advantage in that a separate infrastructure for the transport and storage of pure hydrogen as a fuel would not be required. This is not the case for low - temperature fuel cells such as Polymer Electrolyte Membrane (PEM) fuel cells.

Rare Earth Elements (REE) are commonly used in SOFC fabrication. In a recent report by J. Thijssen LLC (2011) on critical materials for SOFCs prepared for the National Energy Technology Laboratory (NETL), yttria is highlighted the primary critical material of interest. Yttria, however, represents less than 1% of SOFC weight. The demand for yttria, as outlined in Table 1.3-1, is less than 0.5% of its' current production. Markets have witnessed dramatic increases in yttria prices from $6/kg in 2006 to approximately

$160/kg in recent times; regardless, this amounts to less than $10/kW in materials cost for SOFCs, representing less than 10% of stack module cost and less than 1% of installed SOFC power-plant capital cost. Stack materials can also be recycled for their REE content, reducing REE demand for stack replacements by 80 to 90% [22]. The abundance of REE materials is, therefore, likely to have a minimal impact on the commercialization of SOFCs.

Table 1.3-1: Overview of SOFC Driven REE Demand, Production and Reserves [22]

	Content of SOFC	SOFC-Driven Net Demand	Production (2010)	Estimated Reserves	Projected Production (2015)
	g/kW	t/yr (2030)	t/yr	T	t/yr
Yttria	21	40	9,000	540,000	10,000

One of the key drawbacks to commercialization of SOFC technology is primarily its manufacturing cost. The thermal stresses between adjacent materials result in the need for high-strength materials with compatible thermal expansion coefficients, especially for cell interconnects and seals. Hawkes *et al.* (2005) state that operation and maintenance costs are high at $0.025 kWh^{-1}, though based on assertion can be driven down to $0.01 kWh^{-1} [20].

1.4 Overview of Current Developments in SOFC Systems

Status of SOFCs in Major World Economies

Cost reductions over the years in the development of industrial SOFC systems have been encouraging. The Department of Energy (DOE) has estimated that for a 5 kW planar SOFC and Gas-Turbine hybrid system, a cost of $400/kW can be achieved at

reasonable manufacturing volumes [23]. The DOE initiated the Solid State Energy Conversion Alliance (SECA) in 2001 and aimed to reduce the cost to less than $400/kW by 2010 [24]. According to Vora (2011), SECA established a target stack module cost of $700/kW (2007 basis), with coal being the major energy source [25]. Rolls Royce suggests that SOFC costs of $300/kW are already possible for large gas-turbine based hybrid systems. The majority of estimates are in the range $700/kW to $1300/kW [20]. The three industry teams selected for the SECA program involved in developing 25 kW stacks for testing were able to achieve the SECA target of $700/kW by the end of the 2010 fiscal year. The SOFC technology from the SECA program is also being deployed in two spin-off applications, those being; a diesel-fueled Auxiliary Power Unit (APU) for truck use and a small power source for an unmanned undersea vehicle [25].

The New Energy and Industrial Technology Development Organization (NEDO) of Japan has been performing basic research and fundamental technology development in order to achieve an early market introduction of an SOFC system also based on coal. Basic research at NEDO for improving durability and reliability involved performing a thermodynamic, mechanical and chemical analysis of the stack followed by evaluation of microstructure changes at the TPB, a 5,000-10,000 hours test for durability and research on the influence of minor impurities in coal gasification gas. Technological developments in stack stop-start cycles and high-pressure operation were also investigated. A total of 136 units ranging from 0.7 to 8 kW output have been installed

as of June 2010 to acquire operational data, with some units expected to demonstrate up to 40,000 hours of continuous operation. The units developed by NEDO have achieved an average electrical efficiency of 35% based on 0.5 kW output. The average electrical efficiency would be 40% based on the rated output of 0.7 kW. NEDO has set efficiency targets of 40% (electrical) and 80% (total energy efficiency) and a stack manufacturing cost target of $625/kW [26].

Steinberger-Wilckens (2011) reported on the status and trends of European SOFC technology. Several companies in Europe are already offering stack modules and complete units at a pre-competitive level for demonstration projects in niche markets. ElringKlinger, a German company, is focusing on diesel-fueled SOFC Auxiliary Power Units (APU) for passenger cars in addition to stationary power generation for the residential sector. Another European Austrian based firm, AVL, currently offers an SOFC APU with engine anti-idling technology for heavy duty trucks. The use of biogas is also a major option in Europe as a renewable energy sources. Biogas is receiving much attention as it is a source of GHG-neutral methane and is fully compatible with the natural gas distribution network [27].

There are a total of 80 companies situated in Canada as listed by Industry Canada, whose primary market focus is related to the development of fuel cells, according to the 2008 Canadian Fuel Cell Hydrogen and Fuel Sector Profile [28]. An SOFC Canada (SOFCC) NSERC Strategic Network has also been established and represents collaboration between 21 Canadian research groups from both university and government partnered

with industry. SOFCC is focusing primarily in Northern Canada, where an infrastructure for the transportation of diesel fuel exists and electricity costs on a per kWh basis are competitive with SOFC technology [29]. Current research is focused on developing sulphur and coke tolerant anodes for sulphur containing fuels, increasing robustness by improvement of manufacturing methods, in addition to evaluation of performance, reliability, durability and thermal management of BoP components. There is an active interest in the fabrication of planar metal-supported cells and tubular, porous electrolyte-supported cells. For the planar design, electrical efficiencies between 40% and 50% are targeted, with a CHP efficiency >80% and a stack manufacturing cost of $400/kW - $2000/kW. For the tubular design, an electrical efficiency of 30% is targeted for a 0.5 kW rating stack and a CHP efficiency >75%. A manufacturing and installation cost <$20,000/kW is targeted [10].

1.5 Problem Statement and Thesis Outline

The overall objective of this project was to develop a tool that would be used for the design and optimization of a small-scale SOFC system. The first objective was to develop a steady-state process simulation of a small scale diesel-fuelled SOFC system using commercial software (VMGSim^{TM}). The second objective was to develop unit operation models in a commercial computational software package (COMSOL Multiphysics^{TM}) to aid in providing insight into aspects of specific component options for the system design. This involved developing a unit operation model of a catalytic plate

reactor assisted by heat exchange. The third objective was to integrate the COMSOL™ model into the VMGSim™ process simulation to demonstrate the use of a multi-scale modeling approach. The output of this work is to be used by the SOFC Canada NSERC Strategic Network in order to develop a small-scale SOFC system design that will demonstrate the use of new sulphur-tolerant anode materials working with specialized fuel-processing technology.

The thesis is subdivided into six chapters. Chapter 1 gives a brief overview of the important aspects of fuel cell systems followed by a discussion of existing technological and economical barriers for commercialization of SOFCs and a review of recent industrial developments in the field. Chapter 2 reviews some of the developments in system Balance of Plant (BoP) components and a review of some of the existing literature on diesel-powered SOFC systems. Chapters 3 and 4 discuss the system simulation work along with a single and multi-variable sensitivity analysis, a CFD model of a coupled reaction and heat exchange unit operation and a proof of concept for integration of the CFD model into VMGSim™. Chapter 5 summarizes the principal findings and provides principal recommendations for the system simulation and unit operation model.

Chapter 2

Literature Review

A review of selected published information on SOFC systems fueled by diesel was conducted and is presented in Section 2.1. A selection of experimental and modeling studies are summarized. System design, performance characteristics and GHG-neutral operation are among the topics discussed. Specific unit operations modeled or used in the process simulation in this thesis are discussed in Section 2.2.

2.1 Diesel-Fuelled SOFC Systems

A *Diesel-Fuelled* SOFC System implies that diesel is the fuel that enters the system and is the input to the Fuel Processing unit (Figure 1.2-1). The H_2 rich stream that exits the fuel processor, or the diesel reformate, is the feed to the SOFC (Power Section). The Power Conditioning unit converts the variable DC voltage from the electrochemical reaction in the SOFC to a directly useable AC supply. The conditioning unit was not within the scope of this thesis and is not discussed in this review. Extensive information on SOFC systems or fuel cell systems in general can be found in textbooks by Larminie and Dicks, Blomen and Mugerwa, and Singhal [9, 16, 30].

Although for this thesis the application of interest was remote stationary generators, diesel-fuelled SOFC systems have been extensively studied for APU systems for long-haul trucks to reduce roadside idling. An SOFC APU run with low sulphur diesel was

tested and studied by the Webasto group in Germany (2006). The APU is rated at 1 kW and was developed in conjunction with H.C. Stark GmbH and Fraunhofer IKTS in Germany based on a planar cell design. The goal of the study was to demonstrate an SOFC system that could be started without electrical heating elements or purge gas. The second goal was to be able to run continuously without an external supply of water while being thermally self-sustainable. A Catalytic Partial Oxidation (CPOX) reactor was used for the reformer unit operation. The CPOX unit contains a total oxidation zone for vaporizing the injected diesel fuel. A flame in the total oxidation zone provides the required thermal energy to the catalytic reforming zone via heat transfer by conduction. The CPOX unit was used as a heater for initial system start-up to avoid use of electrical heating elements. Additional BoP components comprised of a tail-gas porous-media burner with a flame arrestor and a planar (plate) heat exchanger used to pre-heat the cathode air to stack temperature using the burner exhaust. Two gas mixing concepts were tested for the air and stack anode exhaust entering the porous-media burner. The gases were either premixed or non-premixed prior to entering the burner. The burner inlet temperature was limited to ~300 ^{o}C in the former case to prevent the flame from burning back into the mixing zone. The non-premixed concept was independent of the burner inlet temperature, allowing for flexibility in system operation and control. The premixed concept was presented in Webastos' study, however, to represent the worst case scenario. Overall, the SOFC APU was operated for 14 hours with no observed

degradation. The use of dry reformate in the stack was demonstrated and no soot was observed over the period of operation [31].

Kang *et al.* (2008) studied the operating characteristics of SOFCs fuelled by diesel autothermal reformate. Dodecane and methylnaphthalene were used as surrogates of diesel to simplify the quantification of the Steam to Carbon (S to C) ratio, Oxygen to Carbon (O_2 to C) ratio and the fuel conversion.

Kang *et al.* considered coke formation to be the most serious problem for diesel reformer-SOFC systems. Diesel fuel is often difficult to vaporize effectively due to the presence of heavier hydrocarbons. Fuel and oxidants being non-homogeneously mixed as a result, are prone to coke formation through pyrolysis in local fuel rich zones. Additionally, a lower fuel conversion in the reformer produces a reformate entering the SOFC with a greater composition of hydrocarbons. Parmar et *al.* [32] have reported a thermodynamic analysis of the carbon forming regions for steam, autothermal and catalytic partial oxidation reformation. A decrease in the quality of the reformate has a direct effect on stack performance, where additional quantities of hydrocarbons exposed to the anode exhibit a greater tendency for carbon formation.

Kang *et al.* observed that, for a constant current density, the SOFC operating voltage increased with a greater Gas Hourly Space Velocity (GHSV) in the ATR. The increase was attributed to a lower fuel utilization, or an increased total available amount of fuel at the stack anode. The effect was observed despite the decrease in partial pressures of H_2 and CO in the reformer arising from mass transfer limitations in the catalyst bed.

Increasing the S to C ratio at a fixed current density increased the fuel conversion and reduced coke formation. More energy was required, however, to vaporize the water. The additional steam also diluted the hydrogen to the stack and, therefore, a drop in stack operating voltage was observed.

Increasing the O_2 to C ratio, also for a constant current density, decreased the H_2 and CO concentrations in reformate product gas due to rapid H_2 and CO oxidation. Additionally, the fuel dilution by N_2 in the reformate resulted in a lower SOFC operating voltage compared to predictions from the Nernst equation based on pure H_2 entering the anode [33].

Yi *et al.* (2005) studied the fuel flexibility of an integrated 25 kW SOFC-reformer system at the National Fuel Cell Research Centre in the University of California. A total of four fuel types of different compositions were investigated, including pipeline natural gas, diesel reformate (after pre-reformer), biogas (landfill or digester gas) and coal-derived syngas. The Siemens Westinghouse single cell per tube, tubular design configuration was used for the stack (576 cells), where the cathode is located on the inside of the tube. In Figure 2.1-1, desulphurized fuel enters the bottom of the stack to an ejector. The ejector creates a partial vacuum to pull spent fuel from the Anode Off-Gas (AOG) recirculation zone at the top of the stack and captures water vapor for the steam reforming zone. The reformed fuel is then distributed to the outer surface of the tubes. Cathode air is pre-heated using the system exhaust and sent to the inner surface of the fuel cell tubes using air feed tubes from the top of the stack. The oxygen in the air

forms oxygen anions that flow back upwards inside the fuel cell tubes. The anions travel through the solid oxide electrolyte and electrochemically react with the oxidized fuel outside the tubes. A fraction of the AOG is recirculated back to the bottom of the stack and the remainder is burnt using depleted air in the combustion zone at the top of the SOFC Generator.

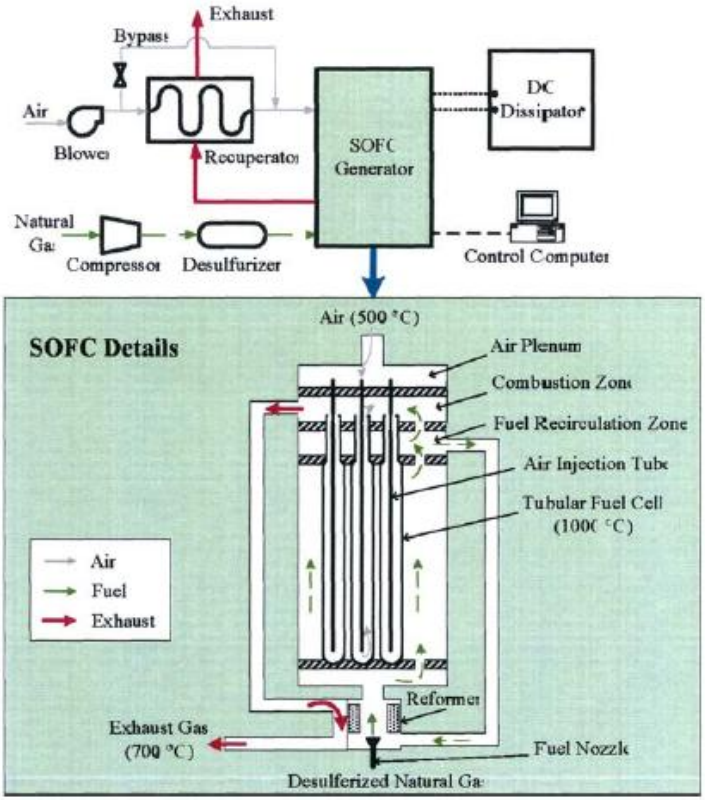

Figure 2.1-1: Schematic of Siemens Westinghouse 25 kW System [34]

The system was validated using the Advanced Power Systems Analysis Tools developed at the University of California. Residual errors between the experimental and model predictions for principal performance parameters including efficiencies and power consumption were less than 3%. Fuel compression was ignored in the model as pipeline

natural gas is at a sufficient pressure and the syngases are assumed to be compressed prior to being delivered to the system. The fuel utilization was set to a constant value of 82%, whereas the AOG recirculation ratio varied with different fuel compositions to avoid carbon formation while not significantly compromising system efficiency. The AOG contains steam from the reformate and steam generated from the SOFC. The effect of AOG recirculation on system efficiency is the same as the dilution effect associated with the S to C ratio as discussed earlier in this section.

Yi *et al.* observed that the exhaust temperatures from the SOFC system using biogas and diesel reformate as fuel sources were 7^{o}C and 21^{o}C higher than for natural gas. This was attributed to lower CH_4 content in these fuels; hence, the reduced endothermic effects associated with the CH_4 reforming reaction at the SOFC anode. This was more so the case with coal syngas, with no CH_4 content and high CO content promoting the exothermic Water-Gas Shift (WGS) reaction. A 153^{o}C increase in exhaust temperature was observed for coal syngas and also the lowest system efficiency (26.5%). Natural gas, diesel reformate and biogas yielded system efficiencies of 37.2%, 35.8% and 36.1%, respectively. Higher system efficiencies can be achieved using gas turbines by producing useful work from recoverable heat in the exhaust.

Carbon deposition was addressed by Yi *et al.* using AOG recirculation to increase the operating temperature and to maintain a high moisture content at the anode. The moisture serves to increase the H and O content of the fuel recirculation stream to shift chemical equilibrium to a region that does not favor carbon deposition. The coal syngas

studied by Yi *et al.* had the highest O content among the studied fuels. The SOFC system fuelled by coal syngas thus required the smallest recirculation ratio to ensure that no carbon deposition was observed, followed by biogas, diesel reformate and natural gas [34].

Vourliotakis *et al.* (2011) used a reactor network approach to model a SOFC system operated on liquid fuels. The reactor network uses a simplified flow and mixing representation and includes detailed reaction chemistry. All chemical reactors were modeled as ideal reactors. The approach is an alternative to full CFD modeling, in which complex flow and reaction chemistry are directly coupled and result in the use of additional resources and computation time.

CFD calculations and CHEMKIN were used to generate the reactor network and to couple detailed reforming kinetics. N-heptane was chosen as the diesel surrogate. The SOFC system (including reactor network and BoP components) modeled by Vourliotakis *et al.* can in principle operate with both gaseous fuels such as natural gas and liquid fuels such as diesel.

In the reactor network, the fuel is simultaneously vaporized and mixed using a Stabilized Cool Flame Vaporizer (SCFV), followed by a Thermal Partial Oxidation (TPOX) reactor. The SCFV operation serves to separate the mixing and vaporization zone from the combustion zone in the TPOX to avoid fuel auto-ignition. In an SCFV unit operation, about 5 to 10% of the fuel on a mass basis is converted to heat to provide the required vaporization enthalpy for achieving homogeneous mixing. Additionally, the SCFV unit

consists of recirculation zones to improve mixture homogeneity. The TPOX reactor design provides the advantage of non-catalytic oxidation. This is, however, at the expense of higher operating temperatures above 1000 K.

In the reactor network, the SCFV was modeled as a combination of five Perfectly Stirred Reactors (PSR) and a single Plug Flow Reactor (PFR). The first PSR represented the mixing zone near the reactor inlet and was connected in series to three looping PSR's that described the recirculation zone. The PFR in series modeled the flow for the inner flow cylinder for the SCFV. Upstream of the SCFV, the TPOX reactor was represented by two PSRs and one PFR in series. The recuperator (which pre-heats the inlet air to the SCFV using heat from the TPOX exhaust gases) was modeled using plug-flow conditions and the SOFC off-gas burner unit operation was considered as an individual PFR. In addition, the SOFC unit operation was modeled as an isothermal honeycomb monolith in plug flow conditions. Vourliotakis *et al.* were able to successfully predict the TPOX reactor exit and average recirculation temperatures in the SCFV mixing zone, in agreement with experimental studies in literature.

The integrated SOFC system developed by Vourliotakis *et al.* provides information on the evolution of major species as well as temperature predictions in the process. The model is demonstrated as an accurate design tool (at both a system and component level) to determine the optimum conditions required for clean and efficient operation [35].

By contrast, Lee *et al*. (2011) from the National United University in Taiwan presented an analytical and parametric study on the design and optimization of a SOFC system using a previously developed high-fidelity simulation tool. The model was able to predict system-level performance and characterize the heat transfer effects between system components. N-dodecane was used in the simulation as the diesel surrogate. In addition, a pure oxygen supply was used for the cathode. The main focus of the investigation was the effect of AOG recirculation. The entire system, including BoP components, consisted of a SOFC with Direct Internal Reforming (DIR), an external steam reformer, two heat exchangers, an afterburner, a condenser, a cooler, a CO_2 adsorber, a fuel injector, a fuel compressor and an AOG compressor. In the system simulation, the AOG recirculation stream was first cooled, compressed, reheated and finally sent to the reformer. Cooling the recirculation stream first avoided compression at a high temperature and, therefore, avoided additional work. The remaining AOG was sent to a tail-gas burner along with the cathode off-gas to provide heat for the external steam reformer. Additional fuel was added to the burner when necessary to meet heating requirements. The burner off-gas reheated the AOG stream and was condensed to a saturated steam mixture after pre-heating the pure oxygen stream. Lastly, an adsorbent bed removed CO_2 prior to the fuel reformate entering the stack anode.

Lee *et al.* determined exit compositions for the external reformer and SOFC stack, based on thermodynamic equilibrium calculations. An electrochemical, anode-supported SOFC model was used to determine the cell voltage by consideration of activation,

ohmic and concentration losses. Finally, the energy balances for the SOFC, external reformer and the burner operations were derived assuming non-adiabatic operation.

The system performance was evaluated as function of S to C ratio, fuel cell temperature, the AOG recirculation ratio and the CO_2 adsorption percentage. Lee *et al*. reported system efficiencies between 50 and 70% using a fuel utilization of 85% and an oxygen/n-dodecane molar stoichiometric ratio of 18.5. Increasing the S to C ratio diluted the H_2 in the reformate entering the stack anode, as also seen by Kang *et al*. [33]; consequently, a lower operating voltage was observed.

Increasing the SOFC temperature resulted in an increase in the operating voltage for a given current density. This is as would be expected due to an increase in the ionic conductivity of the electrolyte with temperature. Lowering the SOFC temperature resulted in an increase in the Nernst potential but the corresponding increase in the over-potential offset this gain. The over-potential here refers to the potential loss incurred at lower SOFC temperatures due to the decreased electrolyte ionic conductivity. The outcome was that the lowest SOFC temperature had the fastest decline in operating voltage with current density.

Increasing the AOG recirculation ratio had an effect similar to the S to C ratio, where the H_2 in the reformate entering the stack was diluted by additional steam. Increasing the CO_2 removal from the reformate stream had a positive effect. An increase in the H_2 partial pressure at the anode was observed as additional CO_2 was removed. This gave rise to an increase in the operating voltage [36].

In a recent study from the Colorado School of Mines, Kattke *et al.* (2011) developed a model for a highly integrated hexadecane-fuelled small-scale tubular SOFC system for APU applications. Their approach was to use a 1-D electrochemical SOFC model coupled with a 3-D CFD model of BoP components. The SOFC stack was a tubular configuration. The cell tubes were open at both ends, with the cathode gas flow being external (shell-side) and the anode gas flow being internal (tube-side). Each tube had an outside diameter of 1.1 cm. The hotbox was insulated from the surroundings and consisted of a 66 cell bundle SOFC unit, a CPOX reactor, Tail-Gas Combustor (TGC) and a recuperator for pre-heating the air. Air was fed from the top of the hotbox via four tubes in the external manifold and was pre-heated prior to entering into the cathode on the shell-side of the tubes. Again at the top of the hotbox, a mixture of fuel and air was fed into the central channel and was pre-heated prior to entering the CPOX reactor towards the bottom. The resulting reformate from the CPOX was then distributed to the anode inside the cell tubes. The unspent fuel and air were mixed near the top of the hotbox before entering the TGC. The final exhaust pre-heated the incoming cathode air and, finally, left the hotbox at the bottom.

Kattke *et al.* reported a baseline system efficiency, stack efficiency and stack power of 21.1%, 25.1% and 637W, respectively. The low efficiencies were attributed to a low fuel utilization of 56%. A variation in the cell bundle voltage of 81mV and the lowest cell voltages below 0.6V for the cells closest to the stack can wall were observed. The low voltage was flagged as a concern due to the increased probability of O^{2-} anions oxidizing

the Ni at the anode. Ni oxidation at the anode is undesirable and increases material stresses, eventually resulting in mechanical failure.

A sensitivity analysis was carried out by Kattke *et al.* by varying the fuel and oxidant flow rates as well as the cell current, one parameter at a time in order to better understand the behavior of the system. The effect of surface emissivity and insulation thickness was also studied. Both of these properties were determined to have a negligible effect on the stack power or system efficiency, with the exception of small insulation thickness values less than 25% of the baseline equivalent. Kattke *et al.* reported that radiative heat transfer was the dominant effect and accounted for 66-92% of the heat transfer in the stack.

Kattke *et al.* reported that, for a constant current density, a 10% decrease in the air flow rate from the baseline, was accompanied by an increase in the temperature throughout the entire hotbox. An 8.7% increase in stack power and system efficiency from the baseline was thus observed. Furthermore, the temperature difference between the SOFC stack and the surroundings in the hotbox was reduced as was the variation in cell voltage across the cells in the stack. The minimum cell voltage observed in the stack cells was also higher than the baseline case.

Kattke *et al.* reported that a 10% decrease in the fuel flow rate from the baseline case was accompanied by a 13.7% decrease in the stack power and a 4.1% decrease in the system efficiency, again for a constant current density. The decrease in the stack power was attributed to lower cell temperatures. This inverse relationship between the fuel

utilization and the system efficiency persisted throughout the majority of the studied fuel flow range.

Increasing the cell current, at a constant fuel flow rate, was accompanied by an increase in the fuel utilization. In their study, the stack power and system efficiency were directly proportional and the most sensitive to the cell current. The system efficiency was, therefore, instead observed to be directly proportional to the fuel utilization for current densities below peak power. Minimal variation in system temperatures was observed and was attributed to the temperature regulating effect on the integrated system design. For instance, at lower current density settings, smaller irreversibilities in the SOFC reduced the cell temperatures. Alternatively, additional unutilized fuel available to the TGC resulted in a rise in cell temperatures. The self-regulating feature of the system is important with regards to process control, with fewer manipulated variables being required for stable operation [37].

An earlier study by Baratto *et al.* looked at the impact assessment and trade-offs of diesel fuel based APUs. System level modeling and cost modeling were discussed in the context of reducing the common practice of idling in heavy duty trucks. The system was modeled in Aspen and consisted of an Autothermal Reformer (ATR) followed by desulphurization downstream (Figure 2.1-2).

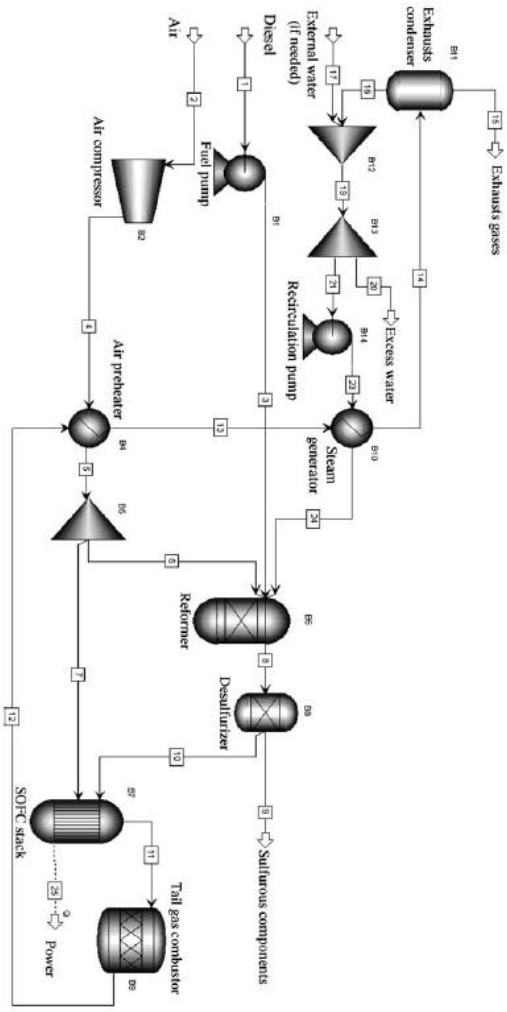

Figure 2.1-2: Flow Sheet of SOFC-based APU [38]

The TGC off-gas was used to pre-heat the compressed air and generate steam for the reformer. The steam required for the ATR was supplied by condensation of the TGC off-gas. In the desulphurization unit, a sulphur removal efficiency of 100% was assumed. Overall, a net system efficiency of 37.4% was obtained at a cell voltage of 0.69 V for a 5 kW system at a fuel utilization of 90% [38]. The simulation of Baratto *et al.* is similar to the simulation of this thesis that will be described in the next chapter.

2.2 Unit Operations for SOFC Systems

The SOFC system modeled in this thesis uses a liquid-phase desulphurization bed for the removal of sulphur-containing compounds. Additionally, a Catalytic Plate Reactor (CPR) is modeled as a component option for the system design. This section presents a brief overview of liquid-phase desulphurization technologies and of CPR technologies used for process intensification.

2.2.1 Desulphurization Technologies

SOFCs are severely poisoned by 1 ppm sulphur concentrations in the anode feed gas. Poisoning by sulphur concentrations as low as 50 ppb has been demonstrated to be severe at lower operating temperatures of 750 ^{o}C [39]. According to a 2009 review of the specifications for contaminant levels in the anode feed, SOFC vendor requirements for sulphur content vary from 0.1 ppm for Versa Power Systems to as low as 5 ppb for Ceramic Fuel Cells Limited in Australia [40].

It is therefore important to desulphurize the majority of the fuel feed to the system, upstream of the stack. Fuel reforming assists in reducing the concentration of sulphur in the reformate entering the stack by dilution. The dilution effect is caused by an increase in the number of moles during reforming and, therefore, the volume of the reformate exiting the reformer.

Rheinberg *et al.* (2008) reported that sulphur tolerance in reforming processes typically increases from SR to ATR to CPOX; from <0.1 ppm tolerance for SR up to 50 ppm for CPOX for short periods of time. With a sulphur content in the feed to the reformer of 10

ppm, a sulphur concentration in the reformate of 1 ppm can be achieved through dilution, and a unit operation for desulphurization is not required. An additional desulphurization process must be available on site, however, if a sulphur concentration in the reformate stream of <1 ppm is required. Hydrodesulphurization, or deep-desulphurization, is a commonly employed technique for sulphur removal in large-scale industrial refineries. The high process operating temperatures (300-400 ^{o}C) and pressures (40-50 bar), however, make this process impractical for small-scale systems. Rheinberg *et al.* investigated the adsorptive liquid desulphurization of low-sulphur diesel fuel using a commercial Ni/Ni-O sorbent. The Ni/Ni-O sorbent was identified as being able to successfully remove refractory species such as 4,6-dimethyldibenzothiophene, with sulphur concentrations reduced to <0.2 ppm.

Rheinberg *et al.* (2008) conducted a parametric analysis to study the influence of temperature and residence time on the sulphur concentration at the exit of the desulphurization unit. The best results yielded a final sulphur content of <0.2 ppm at 200 ^{o}C for low-sulphur diesel fuel containing 6 ppm sulphur. At this operating point, there was a negligible influence on kinetics of desulphurization. The exit sulphur concentration was found to be strongly dependent on the residence time at temperatures <180 ^{o}C. Larger residence times at temperatures <180 ^{o}C (in comparison to temperatures of 200 ^{o}C and above), however, did not yield low sulphur concentrations on the order of 0.2 ppm at the exit of the desulphurization unit [41].

Hernández *et al.* (2008) studied liquid adsorptive desulphurization for removing sulphur from natural gas, and from a simulated liquid diesel fuel containing three sulphur species. The model diesel fuel was a mixture of decane and dodecane in a 2:1 ratio and consisted of the following sulphur-containing compounds; benzothiophene (1), dibenzothiophene (2) and 4,6-dimethylbenzothiophene (3). Good sulphur removal efficiencies were observed for two Ni/SiO_2-Al_2O_3 sorbents. From a mechanistic standpoint, this result was attributed to the direct interaction between the heteroatom in the fuel and the nickel surface. Adsorption capacities decreased in the order of (1) > (2) > (3). The results, therefore, indicated that the interaction between the sulphur atom and the sorbent active sites was attributed to the methyl groups [42].

The TDA Research group, based in Colorado, has focused on desulphurization processes in bio-fuelled SOFCs. The group has developed low cost, high-capacity and ambient temperature sorbents that currently can outperform commercial adsorbents for H_2S removal. In their study, the TDA sorbent was compared with a commercial activated carbon sorbent under saturated moisture conditions. The best TDA sorbent was found to have high sulphur capacities of 35 wt% sulphur for a biogas feed. TDA claims that the sulphur adsorbing capacity is among the highest ever reported for a sulphur adsorption bed [43].

2.2.2 Catalytic Plate Reactors

The concept of process intensification has long been around in the chemical engineering industry. It relies on the development of novel technologies that are inherently safer, can substantially reduce the equipment-size/production-capacity ratio, and improve energy efficiencies. [44]. Catalytic Plate Reactors (CPRs) are an example of a heat-exchanger reactor used for process intensification. Compared to conventional chemical reactors, CPRs have the potential to provide higher product throughputs, greater heat transfer rates and lower manufacturing costs.

CPRs use thin, stacked metal plates coated with a catalyst layer. Process intensification in CPRs can be achieved via two methods. In one method, exothermic and endothermic reactions take place in alternative channels [45]. In the second method, a hot flue gas exchanges heat with an endothermic reaction taking place in an alternate channel, as was studied in this thesis. Some of the existing literature on CPRs [45-50] is discussed here and a detailed two-dimensional model of a CPR is also presented in Chapter 4.

In a recent study by Grote *et al*. (2010), experimental and computational investigations were performed on a compact steam reformer for fuel oil and diesel fuel. The structure of the reactor along with flow configuration can be seen in Figure 2.2-1.

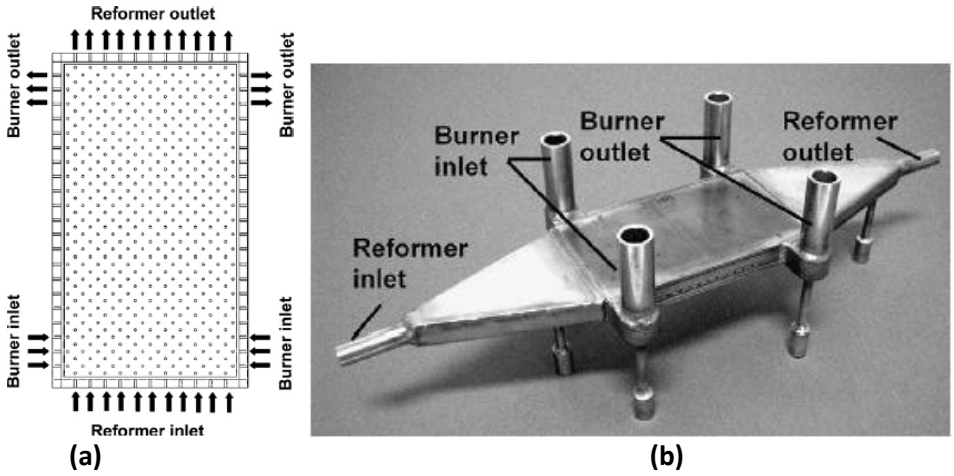

Figure 2.2-1: (a) Top View Outline of Reactor; (b) Reactor Experimental Setup [46]

The reactor was designed as a catalytically coated plate heat exchanger to couple the reforming and combustion reactions. The reformate exiting the reactor was used to superheat the steam prior to reforming. The aim of the study was to optimize the performance and durability of the reactor: quick overheating of reactants to prevent carbon formation, high fuel conversion rates, a homogeneous temperature distribution, low pressure drop, and a maximum operating temperature of 1173 K.

Reforming kinetics were modeled using a power law expression originally derived from the kinetics of hexadecane on an Rh based catalyst. Tetradecane was used as the surrogate for representing fuel oil. The average chemical formula for diesel fuel used was also similar to that of tetradecane. Heterogeneous-based combustion kinetics were

modeled using an empirical formulation for butane, on a Pt catalyst. Grote *et al.* observed from pre-calculations that there was little or no limitation of heat transfer in the catalyst layer. The CFD model, therefore, did not consider the thin catalyst layer phase. Spatial variations influenced by reaction kinetics were instead modeled through an analytical expression of the effectiveness factor. Grote *et al.'s* calculations yielded good agreement with experimental studies for reactor temperature distribution and reformer fuel conversion. Several parameters were varied in order to optimize the reactor, including flow configuration and reactor geometry. The parameters were ranked on a scale of 0-10, zero being the case where demands were not met. CFD results indicated that the cross-flow and counter-flow configurations exhibited the the highest standard deviations in temperature of 100 K and 117 K, respectively. Pressure loss was most reduced by increasing the channel height. The burner width was also increased in the simulation and resulted in an increase in the length for reactants overheating by 40%. The original co-current flow reactor, with a reduced burner width and an increased channel height, was concluded to best meet demands [46].

Zanfir *et al.* (2002) studied the influence of a number of parameters on thermal behavior and performance for CPRs using methane steam-reforming and combustion in alternative channel arrangements. A two-dimensional model was used, and the parameters of interest included channel height, wall thickness, inlet temperature, composition, velocities and kinetic parameters. Zanfir *et al.* characterized the importance of catalyst choice, so that small changes in design and operating parameters

do not significantly affect reactor operation. Two different catalysts for the combustion reaction were studied. The catalyst choice (characterized by activation energy), and the inlet temperature exhibited the greatest sensitivities among the parameters studied [45].

In a later study (2003), Zanfir *et al*. further investigated catalytic combustion-assisted methane steam reforming in a CPR. A two-dimensional half-channel mathematical model was formulated to determine temperature and concentration distributions inside the reactor (Figure 2.2-2). The Froment and Xu [51] rate expressions based on the $Ni/MgAl_2O_3$ catalyst were used to model steam reforming kinetics.

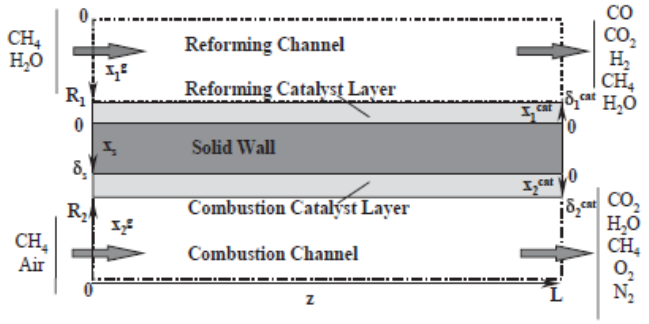

Figure 2.2-2: Single plate geometry depicting model domains [48]

Zanfir *et al.* (2003) concluded that, compared to conventional tubular reformers with a 250 K temperature difference between the tube wall and mean gas-phase temperature, the CPR reactor temperature difference did not exceed 0.5 K across the wall and 40 K across the gas-phase, allowing for a more homogeneous temperature distribution. Effectiveness factors were determined to be on an order of magnitude higher than conventional reformers. The effectiveness factor for the catalyst was defined as the ratio of the average rate of reaction inside the catalyst layer and the rate of reaction if

the catalyst layer was exposed rate of reaction at the catalyst surface (x_1^{cat} or x_2^{cat} in Figure 2.2-2). A low concentration of hydrogen near the entrance of the reactor resulted in a high rate of reforming and methanation at the catalyst surface and thus a low reforming effectiveness factor. Conversely, the effectiveness factor of WGS had a larger value at the entrance as no CO was present in the fuel feed. CO was present in higher concentrations within the catalyst layer, in comparison to the catalyst surface. The effectiveness factors predicted by Zanfir *et al.'s* (2003) mathematical model are depicted in Figure 2.2-3.

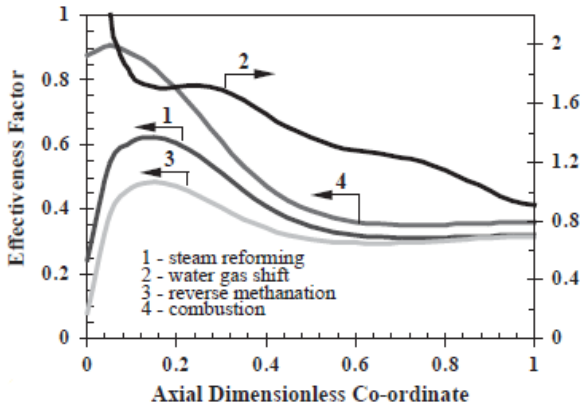

Figure 2.2-3: Effectiveness factors along axial length of reactor [48]

The half-channel height was varied by keeping a constant flow rate at the reactor inlet per total amount of catalyst. The product of half-channel height and inlet velocity was, therefore, kept at a constant value. Marginally higher outlet methane conversion was seen for smaller channel heights and was attributed to lower mass transfer resistances in the catalyst layer. The sensitivity to the outlet conversion was much higher as the channel height was changed while keeping a constant inlet velocity. In this case,

decreasing channel height reduced the channel inlet flow rate per catalyst volume and an increase in the conversion of methane was therefore observed.

Zanfir *et al*. (2003) also investigated the influence of catalyst thickness by maintaining a constant catalyst thickness to inlet velocity ratio, again to ensure a constant inlet flow rate per unit catalyst volume. Lower conversions were observed for larger catalyst thickness values and attributed to greater intra-phase mass transfer resistances and also a lower reactor residence time (for a constant catalyst thickness to inlet velocity ratio). The reforming and combustion effectiveness factors were also reduced [48].

Chapter 3

System Studies

3.1 Process Overview of Diesel-Fuelled SOFC System

One of the end goals of the SOFCC NSERC Strategic Network is to develop a small scale SOFC system run on diesel to demonstrate new sulphur and coke tolerant anode materials working with specialized fuel processing technology. In this chapter, a simulation of a 1 kW diesel-fuelled SOFC system at steady-state is presented. The SOFC unit operation is custom built using the associated mass and energy balances and a cell model adopted from an experimentally validated study [52]. Further details can be found in sub-chapters 3.2 and 3.3. An important feature of the system is the use of an ATR, whereby heat generated from the oxidation reaction and the heat required by the endothermic steam reforming reaction can be finely controlled via adjusting the relative amounts of fuel, steam and air to the reactor. In the current literature on diesel-fed SOFC systems, most use either steam reforming [36, 53], CPOX [31, 37] or TPOX [35] as part of their fuel processing methods, with ATR fuel processing directed primarily towards APUs [33, 38, 54]. Following these sub-chapters is a sensitivity analysis of the influence of key process operating and design variables on three performance metrics, those being the net system efficiency, stack efficiency and the final exhaust temperature from the system. The analysis provides an insight into operating variables that would need to be tightly controlled to ensure optimal operation. The simulation represents a

base model that will be used in the design and optimization of a demonstrational small-scale SOFC system as part of the deliverables for the SOFC Canada NSERC Strategic Network.

3.1.1 Process Description

A schematic of the process modeled in VMGSim^{TM} is depicted in Figure 3.1-1, with an accompanying color key for description of fluid streams. The Afterburner exhaust serves as the primary heating utility for the system. The availability of excess heat in the system for heat recovery such as from the Afterburner exhaust avoids the need for energy from external sources. The highest temperature stream (a mixture of steam, vaporized fuel and air) to the Autothermal Reformer (ATR) is pre-heated first by the afterburner exhaust stream to minimize losses due to entropy in the heat exchanger, followed by complete vaporization of the diesel fuel from 200 ^{o}C to 320 ^{o}C and production of superheated steam from 20 ^{o}C to 300 ^{o}C. Additional waste heat available from the SOFC anode and cathode exhaust streams is used to pre-heat the air to the cathode to 800 ^{o}C and the incoming fuel to the liquid desulphurization temperature of 200 ^{o}C. The SOFC unit operation in the simulation consists of a set of mass and energy balances. The zero-dimensional cell model used for the unit operation is obtained from an experimentally validated study conducted by Costamagna *et al.* [52] on an integrated-planar and cathode-supported cell design. The cell model provides an estimate of the operating voltage of the stack. Additionally, all the heat exchanger configurations are set to counter-current flow to allow for lower and relatively constant

approach temperatures throughout the exchanger, with a hot stream inlet temperature being matched with the cold stream exit temperature. A low approach temperature of 30 ^{o}C is used for pre-heating the mixture stream to the ATR. The sizing of the heat-exchangers was not considered in the simulation.

Lower approach temperatures are desirable from a system efficiency standpoint in order to reduce irreversible losses from entropy production and maximizing work recovered. In other words, there is a smaller penalty that has to be paid (smaller change in entropy) with a smaller the temperature difference between the hot and cold streams [55]. In addition to the stream mixers and splitters, the remaining BoP components includes the air blower, the liquid adsorption Desulphurization unit and the fuel and water pumps, all of which are represented as parasitic losses in the system. The blower was represented by the compressor unit operation in VMGSim^{TM}, where the required pressure was only 1.07 bar. The blower had the largest associated parasitic loss in the simulation. The parasitic losses were, however, small compared to the electrical energy produced by the stack.

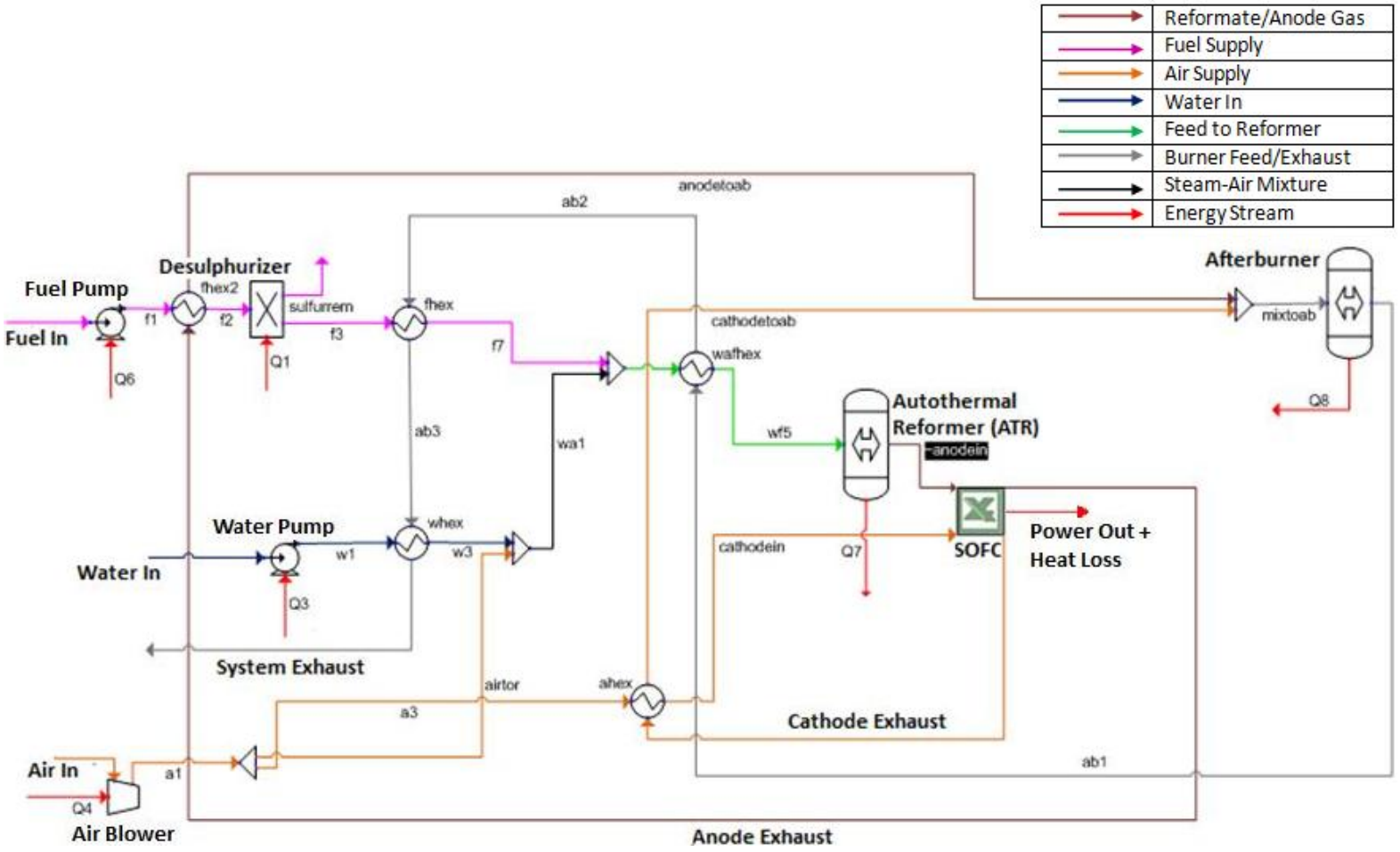

Figure 3.1-1: Process Flow Diagram of 1 kW Diesel-Fed SOFC System

3.1.2 Assumptions and Approximations

The fuel composition chosen to represent the characteristics of diesel fuel is shown in Table 3.1-1. This composition was obtained from communication with Dr. Brant A. Peppley based on his work around air independent propulsion systems. The mixture of hydrocarbons was developed such that the carbon to hydrogen ratio and the boiling point curve was a reasonable approximation to that of standard diesel fuel (personal communication, 2011).

Table 3.1-1: Diesel Feed Mixture Molar Composition

n-NONANE	0.015998	**n-HEXYLBENZENE**	6.03E-02
n-DECANE	8.90E-03	**n-HEPTYLBENZENE**	4.88E-02
n-UNDECANE	4.60E-03	**n-OCTYLBENZENE**	0.049995
n-DODECANE	2.80E-03	**n-NONYLBENZENE**	5.28E-02
n-TRIDECANE	1.40E-03	**n-DECYLBENZENE**	5.12E-02
n-TETRADECANE	1.50E-03	**n-UNDECYLBENZENE**	0.118088
n-PENTADECANE	3.30E-03	**n-DODECYLBENZENE**	0.187781
n-HEXADECANE	0.006999	**NAPHTHALENE**	6.50E-03
n-HEPTADECANE	0.014999	**1-METHYLNAPHTHALENE**	3.30E-03
n-OCTADECANE	3.18E-02	**1-ETHYLNAPHTHALENE**	5.30E-03
n-NONADECANE	6.71E-02	**1-PROPYLNAPHTHALENE**	8.10E-03
n-EICOSANE	0.138886	**1-n-BUTYLNAPHTHALENE**	1.31E-02
n-PENTYLBENZENE	8.37E-02	**PHENYL MERCAPTAN**	1.28E-02

- Negligible pressure drop throughout the system. The heat exchangers were, however, assigned minimal pressure drops on the order of 0.5-2 kPa.
- The ATR and Afterburner in Figure 3.1-1 operate in adiabatic mode. The values of the associated energy streams, Q7 and Q8 are, therefore, zero. Both are modeled as Gibbs reactors, where reactor the exit composition is determined from Gibbs free energy minimization.

- Homogeneous mixing of fuel, steam and air is achieved prior to the ATR stage.
- The Desulphurization Unit is a liquid adsorption separator and the efficiency of sulphur removal is assumed to be 100%. Phenyl Mercaptan is the only sulphur species present in the model diesel fuel in Table 3.3-1.
- CO does not oxidize in the fuel cell stack and the WGS reaction is assumed to be at equilibrium. In the simulation, CO is the limiting reactant in the WGS reaction for the anode stream entering the stack. To account for this in the simulation, CO is first reacted with steam to produce H_2 and CO_2 on a stoichiometric basis. In the last step, WGS equilibrium is re-established using the equilibrium constant for the reaction and the extent of reaction. Further details are provided in Section 3.2.
- The quantity of CH_4 entering the stack is negligible. There is no Direct Internal Reforming (DIR) of CH_4.
- No carbon formation modeled.

It should be noted, however, that for DIR based SOFC systems the endothermic steam reforming of CH_4 at the anode is influential with regards to reducing SOFC heat losses and/or the amount of heat available in the SOFC exhaust.

The assumption about no direct oxidation of CO in the stack was based on the following: (i) the kinetics of H_2 oxidation is more predominant than CO. (ii) the mass transfer of CO into the TPB region is about 10 times slower than H_2 (iii) there is significantly more

surface area at the catalyst surface available for reforming and shift reactions than there is at the TPB for oxidation reactions [4].

3.1.3 Definitions

The net system efficiency is defined as the net power output from the stack over the lower heating value of the fuel entering the system (3.1.1). The parasitic losses are incurred from additional power requirements in the system such as the air blower that would need to be supplied by the stack.

$$Net\ System\ Efficiency = \frac{W_{elec} - W_{parasitic}}{m_{fuelin}\, LHV_{fuelin}} \tag{3.1.1}$$

The stack efficiency is based on the ratio of the stack power output and the LHV of the anode feed gas to the stack. The LHV is based on the CH_4, CO and H_2 content of the anode feed gas (3.1.2). CH_4, CO and H_2 are the only combustible species in the anode feed. Similarly, the reformer efficiency (3.1.3) is defined as the ratio of the LHV of the anode feed gas to the stack over the LHV of the fuel feed to the ATR. An approximate LHV of 42.5 MJ/kg was used for (3.1.1) and (3.1.3) for the diesel composition in Table 3.1-1. The general form of the expressions listed in (3.1.1) through (3.1.3) can also be found in the textbook, *Fuel Cell Systems* [30].

$$Stack\ Efficiency = \frac{W_{elec}}{m_{CO}\, LHV_{CO} + m_{CH_4}\, LHV_{CH_4} + m_{H_2}\, LHV_{H_2}} \tag{3.1.2}$$

$$ATR\ Efficiency = \frac{m_{CO}\, LHV_{CO} + m_{CH_4}\, LHV_{CH_4} + m_{H_2}\, LHV_{H_2}}{m_{fueltoref}\, LHV_{fueltoref}} \tag{3.1.3}$$

Fuel conversion in the ATR is more challenging to quantify for higher hydrocarbon fuels such as diesel. There are variations in literature and the quantity is sometimes defined as the conversion to gaseous carbon species such as CO, CO_2 and C_1-C_6 hydrocarbons as these compounds can be analyzed using a gas chromatograph or mass spectrometer [56]. Equation (3.1.4) for fuel conversion is, however, written in terms of molar flow rates of CO, CO_2, and CH_4 in the product as no C_2-C_6 hydrocarbons are produced in the simulation of the ATR. n_c in (3.1.4) is the weighted average number of carbon atoms per hydrocarbon molecule in the ATR feed.

$$Fuel\ Conversion = \frac{n_{CH_4} + n_{CO} + n_{CO_2}}{n_c \times Molar\ flow rate\ of\ hydrocarbons\ to\ ATR} \tag{3.1.4}$$

The hydrogen yield in the ATR is defined as the molar flow rate of H_2 and CO in the product over the H_2 equivalent of the total molar flow rate of hydrocarbons fed to the reactor (3.1.5). The yield is defined as a function of H_2 and CO to include both H_2 production from reforming and any additional H_2 that could be generated from CO downstream by WGS. n_h represents the theoretical number of moles of hydrogen produced per mol of hydrocarbon [56].

$$Hydrogen\ Yield = \frac{n_{H_2} + n_{CO}}{n_h \times Molar\ flow rate\ of\ hydrocarbons\ to\ ATR} \tag{3.1.5}$$

Lastly, the fuel utilization, U_f, in the stack is based on the total hydrogen molar flow rate in the anode feed; the flow rate of H_2 as well as the flow rate of CO to account for H_2

from WGS [4]. (3.1.7) is expressed in terms of the total available molar flow rate of H_2 entering the stack. ε_{COMB} represents the moles of H_2 consumed in the stack (3.1.6).

$$\varepsilon_{COMB} = \frac{i \times n_{cells}}{2F} \tag{3.1.6}$$

$$U_f = \frac{\varepsilon_{COMB}}{\left(n_{H_2} + n_{CO}\right)} \tag{3.1.7}$$

3.2 Electrochemistry and SOFC Model

An electrochemical model of an integrated-planar and cathode-supported SOFC developed by Costamagna *et al.* [52] was used in the system simulation. This section describes the basic set of equations required for model implementation as was also used by Costamagna.

For a given current density, cell temperature and species composition, the output voltage for a cell can be calculated. This, however, requires an understanding of the basic governing thermodynamic concepts around fuel cells and the associated polarization losses incurred due to activation, ohmic and concentration or mass transport barriers. As derived from the first and second law of thermodynamics, the Gibbs free energy is defined as the maximum non-expansion work attainable in a reversible process of a closed system. For a fuel cell, this is represented by the net electrical work performed from the transport of ions and electrons. For a fuel cell operating on hydrogen and oxygen, the net reaction is depicted in (3.2.1).

$$H_2 + \tfrac{1}{2}O_2 \rightarrow H_2O \tag{3.2.1}$$

The effect of pressure and reactant concentration is expressed by the Nernst equation. The Nernst equation represents the equilibrium potential difference between the anode and cathode electrodes [16].

Irreversibilities are encountered as current is drawn from the cell and therefore results in polarization or losses in voltage. Polarization in a fuel cell can arise from half-cell reaction activation barriers, ohmic losses from electrical resistance in the electrodes and resistance to flow of ions in the electrolyte, and mass-transport barriers for reactants reaching the TPB region. The operating voltage is defined as the Nernst potential minus the sum of the loss in voltage from the polarization effects. Losses incurred due to half-cell reaction activation energies can be expressed by the Butler-Volmer equation. The expression can be simplified and represented in terms of η_{act} (3.2.2), for cases where the charge transfer coefficient is assumed to be 0.5 for both electrodes (as was the case for this thesis). The charge transfer coefficient accounts for the proportion of electrical energy used to incur a change in the rate of the electrochemical reaction. The exchange current density, i_o is a measure of the equilibrium forward and backwards flow of electrons from and to the electrolyte at open-circuit conditions [16].

$$V_{act} = \frac{2RT}{n_e F} sinh^{-1}\left(\frac{i}{2i_o}\right) \tag{3.2.2}$$

$$i_{o,c} = \gamma_c \left(\frac{P_{O_2}}{P_{ref}}\right) exp\left(-E_{act,c}/RT\right) \tag{3.2.3}$$

$$i_{o,a} = \gamma_a \left(\frac{P_{H_2}}{P_{ref}}\right)\left(\frac{P_{H_2O}}{P_{ref}}\right) exp\left(-E_{act,a}/RT\right) \tag{3.2.4}$$

The resistance to movement of electrical charge is represented by ohmic losses. This refers to the transfer of oxygen ions at the electrolyte and the transfer of electrons at the anode and cathode electrodes. An additional contact resistance term is sometimes included to account for imperfect adhesion between different layers. The ohmic resistance term accounts for the observed losses in a fuel cell as a function of current density and is a represented by a linear relationship in the form of $V = i\Omega$.

High current densities are often associated with the presence of concentration over-potentials. Mass transport resistances to the reaction sites at the microstructure level, amid the electrode, electrolyte and gaseous reactants are prominent and therefore the concentration of reactants at the TPB must be considered. Taking the difference in the Nernst potential at bulk conditions and at the TPB, the expressions (3.2.5) and (3.2.6) can be obtained [9].

$$V_{conc,a} = -\frac{RT}{n_e F} ln\left(\frac{1-\left(iRTt_a / n_e F D_{eff,a} P X_{H_2}\right)}{1+\left(iRTt_a / n_e F D_{eff,a} P X_{H_2O}\right)}\right) \tag{3.2.5}$$

$$V_{conc,c} = -\frac{RT}{2n_e F} ln\left(\frac{1}{X_{O_2}} - \left(\frac{1}{X_{O_2}} - 1\right) exp\left(\frac{iRTt_c}{2n_e F D_{eff,c} P}\right)\right) \tag{3.2.6}$$

The bulk mole fractions or partial pressures in the cell model used in (3.2.3) through (3.2.6) were calculated based on the log mean of the values of each species at the inlet and outlet of the stack. (3.2.2) through (3.2.6) were used for setting up the cell model for the system simulation. The cell model parameters adopted from Costamagna *et al*.

[52] were used without modification unless otherwise specified. Most of the required parameters reported by Costamagna *et al.* were obtained from literature.

3.3 Mass and Energy Balances

The SOFC mole balances are presented in Table 3.3-1. In the first column (*CO Shift*), the total amount of CO entering the stack anode is converted to H_2 and CO_2 on a stoichiometric basis. This is based on the assumption listed in the Section 3.1.2 (no direct oxidation of CO in the stack). The sum of the *Initial* and *CO Shift* columns for the anode represents the anode feed to the stack. In the column denoted *Electrochemical Change*, H_2 is consumed as current is drawn. Finally, WGS equilibrium is re-established by calculating the extent of the RWGS reaction, ε_{WGS}.

ε_{WGS} is determined by substituting the WGS equilibrium constant as a function of product and reactant flows (3.3.2) into a temperature dependent equilibrium constant expression (3.3.1) [57]. ε_{WGS} carries a negative value.

Table 3.3-1: SOFC Mol Balance Table

Anode	**Initial**	**CO Shift**	**Electrochemical Change**	**Re-establish WGS Equilibrium**	**Final (Anode Exhaust)**
CO	n_{CO}	$-n_{CO}$	-	$-\varepsilon_{WGS}$	$-\varepsilon_{WGS}$
H_2	n_{H_2}	n_{CO}	$-\frac{i \times n_{cells}}{2F}$	ε_{WGS}	$n_{H_2} + n_{CO} - \frac{i \times n_{cells}}{2F} + \varepsilon_{WGS}$
H_2O	n_{H_2O}	$-n_{CO}$	$\frac{i \times n_{cells}}{2F}$	$-\varepsilon_{WGS}$	$n_{H_2O} - n_{CO} + \frac{i \times n_{cells}}{2F} - \varepsilon_{WGS}$
CO_2	n_{CO_2}	n_{CO}	-	ε_{WGS}	$n_{CO_2} + n_{CO} + \varepsilon_{WGS}$
CH_4	n_{CH_4}	-	-	-	n_{CH_4}
N_2	n_{N_2}	-	-	-	n_{N_2}
Cathode	**Initial**	**Electrochemical Change**	**Final (Cathode Exhaust)**		
O_2	n_{O_2}	$-\frac{i \times n_{cells}}{4F}$	$n_{O_2} - \frac{i \times n_{cells}}{4F}$		
N_2	n_{N_2}	-	n_{N_2}		

$$ln\left(K_{WGS}\right) = 4306/T_{SOFC} - 3.93 \tag{3.3.1}$$

$$K_{WGS} = \frac{\left(\left(n_{CO_2} + n_{CO}\right) + \varepsilon_{WGS}\right)\left(\left(n_{H_2} + n_{CO} - \frac{i \times n_{cells}}{2F}\right) + \varepsilon_{WGS}\right)}{\left(-\varepsilon_{WGS}\right)\left(\left(n_{H_2O} - n_{CO} + \frac{i \times n_{cells}}{2F}\right) - \varepsilon_{WGS}\right)} \tag{3.3.2}$$

The SOFC energy balance consists of enthalpy terms in and out of the stack, the heat of reaction for the electrochemical combustion of the fuel and WGS (Q_{rxn}), an electrical power output and a heat loss term (3.3.3). The input and output enthalpies are calculated from (3.3.4).

$$\sum_{i=1}^{k} H_{i,in} - \sum_{i=1}^{k} H_{i,out} - Q_{rxn} = W_{elec} + Q_{loss} \tag{3.3.3}$$

$$H_i = m_i C_{pi}\left(T_i - T_{ref}\right) \tag{3.3.4}$$

$$Q_{rxn} = \varepsilon_{COMB}\Delta H_{COMB} + \left(n_{CO} + \varepsilon_{WGS}\right)\Delta H_{WGS} \quad (3.3.5)$$

The total heat loss in the stack Q_{loss} was set to an arbitrary value of 400 W in the simulation. It should be noted that in reality, the heat loss would be dependent on the SOFC temperature and an overall heat transfer coefficient.

VMGSim™ Simulation System Controllers

In the setup of the mass and energy balances, an energy balance controller is used. The output temperature of the stack, T_{SOFC} is adjusted as a manipulated variable until the energy balance is satisfied. The target value is the RHS of (3.3.3), or the sum of the electrical power output from the stack and the heat loss. The stack power is, however, a variable, with a direct dependency on the current and voltage; therefore, the controller set point is also a variable quantity in the controller as seen in Table 3.3-2. A total of two controllers are applied in the simulation in addition to a recycle required for the anode stream to the stack. An initial guess is required for the recycle stream for convergence to be achieved. The controller parameters are summarized in Table 3.3-2. MV, SP, and TV are acronyms for the manipulated variable, set point and target variable, respectively.

It should be noted that T_{SOFC} is not physically adjusted in reality and manipulated in the simulation solely in order to satisfy the energy balance. In reality, controlling the air flow rate entering the stack would be a means of maintaining the stack temperature.

Table 3.3-2: Controller Inputs and Outputs

Controller	MV	SP	TV
Fuel Utilization	m_{fuelin}	Constant Fuel Utilization	U_f
Energy Balance	T_{SOFC}	$W_{elec} + Q_{loss}$	$\sum_{i=1}^{k} H_{i,in} - \sum_{i=1}^{k} H_{i,out} - \varepsilon_{COMB}\Delta H_{COMB} - (n_{CO} + \varepsilon_{WGS})\Delta H_{WGS}$

3.4 Sensitivity Analysis

The significance of various process operating and design variables was assessed as a function of the performance metrics described earlier in the chapter. The base-case cell settings and the list of applied constraints for the simulation (sensitivity analysis and multi-variable study presented in the next section) are presented in Table 3.4-1 and Table 3.4-2, respectively. The operating and design variables of interest, assessed in the study, are depicted below.

- Air Utilization (U_a) in the Stack
- Fuel Utilization (U_f) in the Stack
- Oxygen to Carbon (O_2 to C) Ratio in Feed to ATR
- Steam to Carbon (S to C) Ratio in Feed to ATR
- Inlet Cathode Temperature to Stack
- Pre-heater Approach Temperature to ATR

Table 3.4-1: Base-Case System Settings

System Settings			
Thermodynamic Model	Lee-Kesler	**SOFC Pressure**	1.04 atm
S to C to ATR	3	**Stack Outlet Temperature**	870 °C
O_2 to C to ATR	0.25	**SOFC Cell Voltage**	0.696 V
U_f in SOFC	80%	**Cathode Inlet Temperature**	800 °C
U_a in SOFC	25%	**ATR Pre-heater Approach Temperature**	30 °C
Stack Power	1023 W	**ATR Fuel Conversion**	100%
Cell Settings			
Cell Current	15 Amps	**Anode Thickness**	20 µm
Cell Area	100 cm^2	**Cathode Thickness**	500 µm
Number of Cells	98	**Electrolyte Thickness**	20 µm
Cell Pitch Length	1 cm	**Interconnect Thickness**	500 µm[1]

[1][58]

Table 3.4-2: Model Constraints

Parameter	Min	Max
Stack Power Output	0.8 kW	1.2 kW
Average Stack Temperature	-	≤ 1000 °C
Average ATR Temperature	500 °C	1000 °C
ATR Fuel Conversion	≥ 99%	-
ATR Efficiency	≥ 80%	-
ATR Hydrogen Yield (based on H_2 and CO product)	≥ 100%	-
Cathode Exhaust Post-Recuperator Temperature to Burner	≥ 30 °C	-
Minimum Heat-Exchanger Approach Temperature	10 °C	
Cathode Temperature to Stack	500 °C	840 °C
O_2 to C Ratio	0.15	0.5
S to C Ratio	2	4.5
ATR Pre-heater Heat-exchanger Approach Temperature	10 °C	200 °C
Fuel Utilization	50%	90%
Air Utilization	15%	50%

The effect of independent variables on system performance was studied *for a constant current density* and within the constraints defined in Table 3.4-2. All other conditions were kept at the baseline conditions in Table 3.4-1 while an independent variable was varied. The baseline efficiencies were 37% (net system) and 40% (stack). The baseline system exhaust temperature was 217^{o}C. The baseline conditions and model constraints were chosen based on the cell model [52] and from the range of values reported in various textbooks [4, 16, 30].

3.4.1 Effects of Individual Variables

Effect of Air Utilization (U_a)

The effect of an increase in U_a in the SOFC (or a decrease in the feed air flow rate) for a fixed current density, was an increase in the net system efficiency and stack efficiency (Figure 3.4-1). This was in part attributed to the lower power requirements of the air blower as a lower air flow rate to the system was supplied. Secondly, a smaller air flow rate to the stack resulted in less air available for stack cooling and gave rise to an increase in the stack temperature. Operation at higher stack temperatures in the simulation reduced both ohmic and activation losses and contributed to an increase in the stack voltage. Thirdly, an increase in the stack temperature also resulted in an increase in the burner exhaust temperature throughout the studied U_a range. For a constant ATR pre-heater approach temperature, the temperature of the feed to the ATR was increased, giving rise to a greater hydrogen yield (the production of methane was also reduced with the rise in the temperature of the ATR). A smaller system fuel feed

rate was, therefore, required for a constant current density and fuel utilization. The reduced air flow to the stack also reduced the partial pressure of O_2 in the stack and would eventually result in a decrease in the net and stack efficiencies. The combined effects of lower air blower power requirements, a higher stack temperature and a greater hydrogen yield in the ATR were, however, more dominant over the range of $U_a's$ tested. The variation in the stack temperature and the log mean O_2 partial pressure in the SOFC cathode with air utilization are shown in Figure 3.4-2.

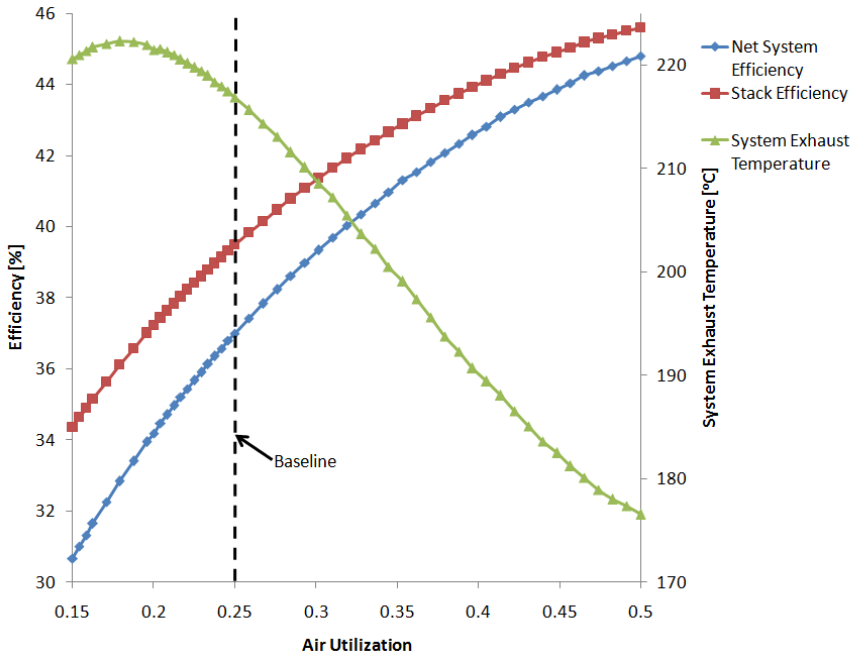

Figure 3.4-1: Effect of Air Utilization on Performance Metrics

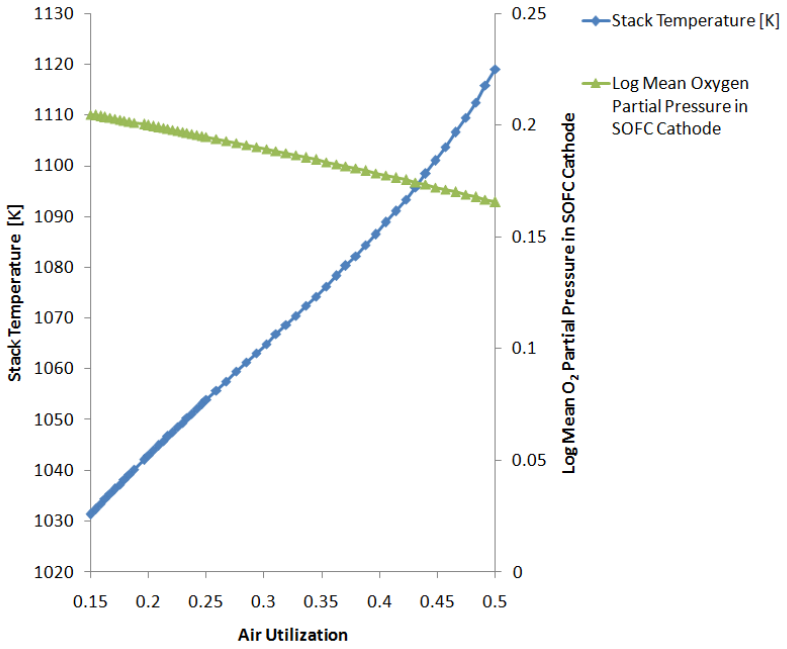

Figure 3.4-2: Effect of Air Utilization on Stack Temperature and Average O_2 Partial Pressure in SOFC Cathode

An increase in the burner exhaust temperature initially resulted in a higher system exhaust temperature as seen in Figure 3.4-1 above. Beyond a utilization factor of approximately 20%, however, a decrease in the system exhaust temperature was observed. This observed effect was attributed to a reduction in the total mass flow rate of the burner exhaust stream with increasing U_a, and to unused air comprising of a large mass fraction of the exhaust. The energy content of the burner exhaust stream was, therefore, reduced and resulted in a lower system exhaust temperature.

Effect of Fuel Utilization (U_f)

The effect of U_f was studied over the range from 50 to 90%. A reduction in the fuel feed rate resulted in a decrease in the average partial pressure of hydrogen in the stack

as a consequence of the increased U_f. A decrease in stack power output was, therefore, observed. Both net system and stack efficiency gains were, however, observed over the simulation range (as seen in Figure 3.4-3) as the total heating value of the fuel feed $\left(m_{fuelin}\ LHV_{fuelin}\ \right)$ decreased with increasing utilization.

Less pre-heated steam was required with increasing U_f for a constant S to C ratio; however, a smaller fuel feed rate to the system resulted in less fuel to the burner. A lower system exhaust temperature was consequently observed.

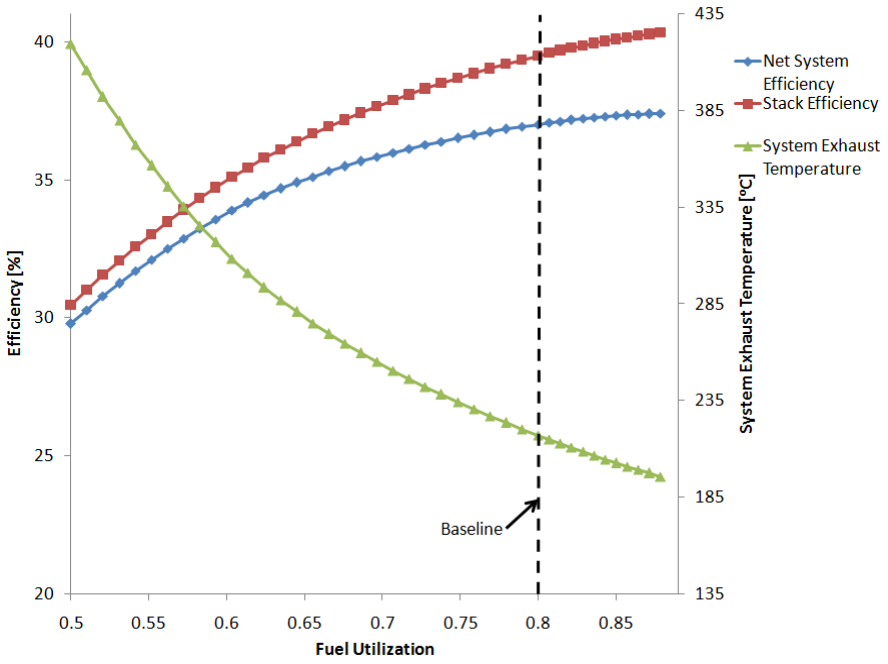

Figure 3.4-3: Effect of Fuel Utilization on Performance Metrics

Effect of O_2 to C Ratio

In the process diagram in Figure 3.1-1, air at 20 ^{o}C is mixed with superheated steam followed by mixing with vaporized diesel fuel. The resulting mixture was pre-heated to

a temperature based on the heat exchanger approach temperature prior to entering the ATR.

The net system and stack efficiencies were initially observed to rise with increasing O_2 to C ratio (Figure 3.4-4). Additional air entering the ATR increased the hydrogen yield and therefore lowered the fuel feed requirements for the system. The increase in hydrogen yield was attributed to the exothermic heat of combustion serving as a heat source for the endothermic steam reforming of diesel to hydrogen.

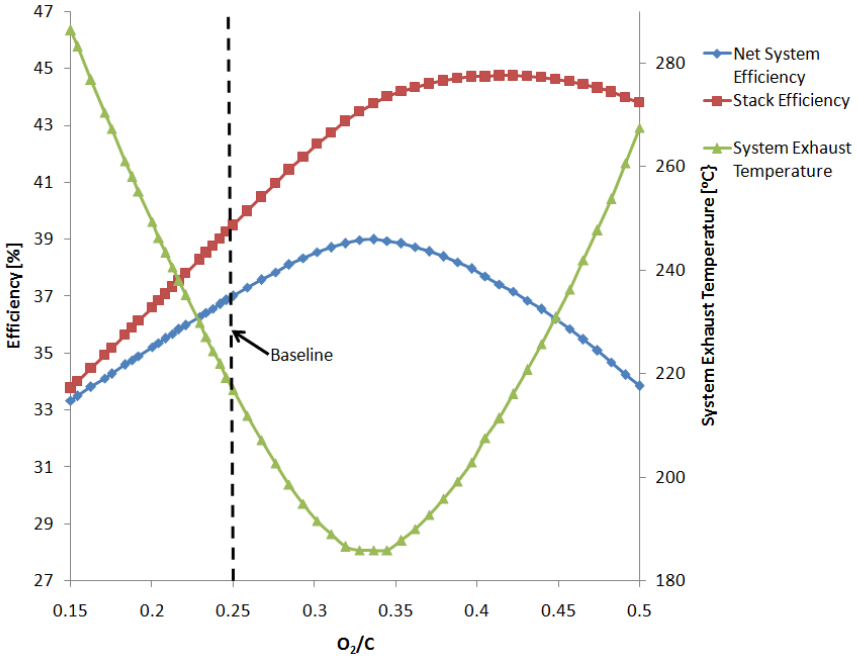

Figure 3.4-4: Effect of O_2 to C Ratio on Performance Metrics

An O_2 to C ratio greater than approximately 0.35, however, had a negative effect on efficiency. A lower hydrogen yield in the ATR was observed due to excess fuel oxidation, in addition to the unfavorable change in the WGS equilibrium (formation of H_2O and CO

from CO_2 and H_2) at higher temperatures (in the ATR as well as in the stack). The fuel feed requirements for the system were thus raised, resulting in a lower efficiency.

In comparison to the net system and stack efficiencies, an increase in the O_2 to C ratio resulted initially in a decrease followed by an increase in the system exhaust temperature as shown in Figure 3.4-4. The initial decrease in the system exhaust temperature was due to the additional pre-heating of the mixed air, steam and fuel stream entering the ATR. Furthermore, there was a heat capacity effect as the mass flow rates of H_2O and CO_2 in the burner exhaust were initially lowered as the O_2 to C ratio to the ATR was increased (Figure 3.4-5) (H_2O in the burner exhaust has the highest specific heat capacity on a mass basis). The reduction in these mass flow rates was attributed to an increase in hydrogen production from steam reforming in the ATR as well as the change in the WGS equilibrium in the stack at higher stack temperatures (reducing the flow of CO_2 out of the stack). The reduction in the fuel feed rate to the system in this initial region with increasing O_2 to C ratio also reduced the amount of H_2O required in the ATR for a constant S to C ratio. The overall effect was a decrease in the heat capacity, energy content and the temperature of the burner exhaust stream and also a decrease in the system exhaust temperature.

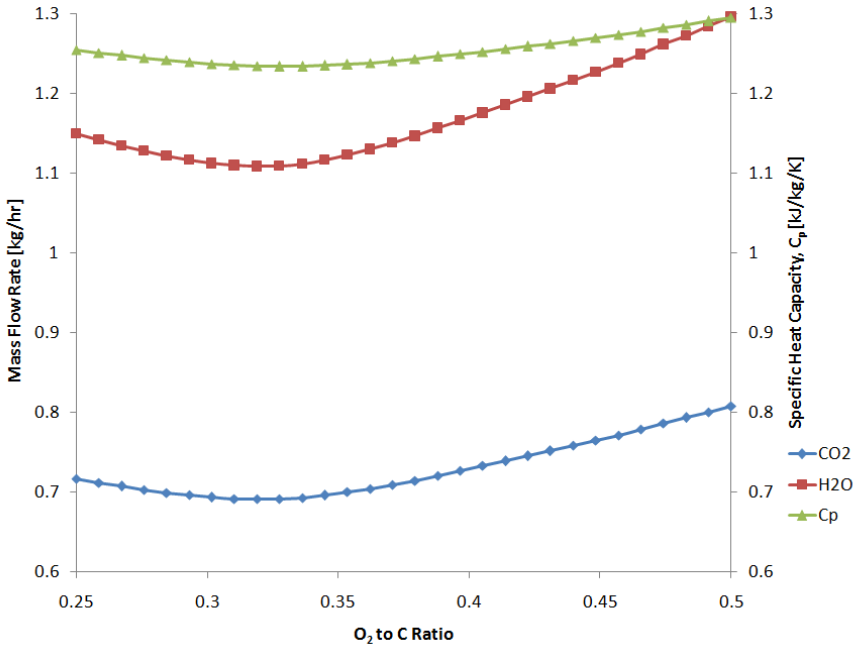

Figure 3.4-5: Effect of O_2 to C Ratio on CO_2 and H_2O Mass Flow Rates and Heat Capacity in the Burner Exhaust

The system exhaust temperature began to rise as the O_2 to C ratio was raised past approximately 0.35. The rise in the system exhaust temperature was in part attributed to the flow rates of CO_2 and H_2O in the burner exhaust increasing with increased fuel oxidation. In addition, the increase in the total mass flow rate of the burner exhaust and an increase in the stream heat capacity increased the total energy content of the stream, resulting in a rise in the system exhaust temperature.

Effect of Steam to Carbon Ratio

The molar flow rate of water entering the system was determined by the specified S to C ratio based on the weighted average number of carbon atoms per molecule in the diesel fuel feed. An increase in the S to C ratio was initially accompanied by a slow rise in the

net system and stack efficiency as the hydrogen yield in the ATR was increased (Figure 3.4-6).

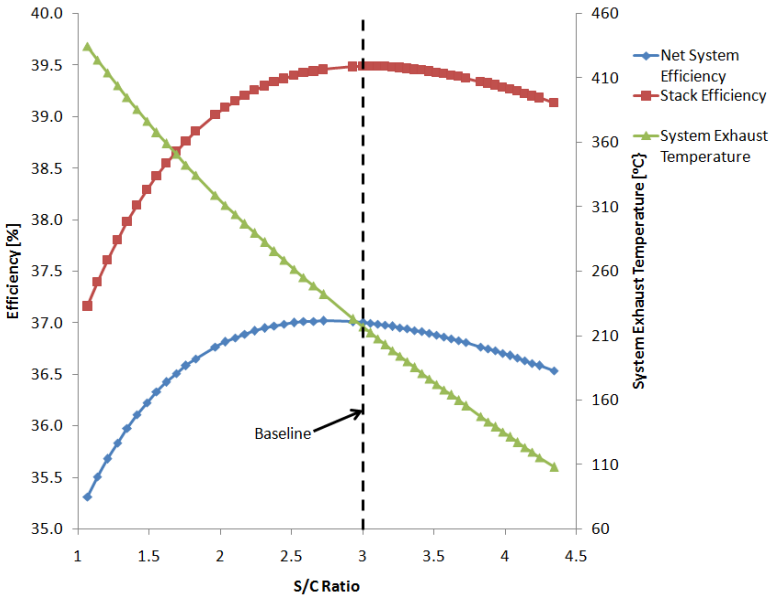

Figure 3.4-6: Effect of S to C Ratio on Performance Metrics

An increase in the hydrogen yield reduced the fuel flow requirements to the system and, therefore, the total heating value of the feed stream. As more steam was added, however (an S to C > ~ 2.5), the H_2 downstream in the stack became increasingly diluted, resulting in a lower H_2 partial pressure [33]. A lowering of the stack power output was, therefore, observed. Secondly, the increase in the hydrogen yield was less pronounced with an increasing amount of steam and the overall effect was a loss in net and stack efficiency.

Lastly, the system exhaust temperature as can be seen in Figure 3.4-6, decreased with an increasing S to C ratio. This was attributed to the following. Firstly, being a lower stack temperature and the temperature of the anode and cathode exhaust streams

exiting the stack and entering the burner were lower. Secondly, additional pre-heating of the ATR feed was required with more steam entering the system at higher S to C ratios. Additional pre-heating was also required to provide the latent heat of vaporization for generating steam.

Operation at S to C ratios <2 is not desirable due to possibility of carbon formation and is, therefore, an undesirable operating condition. The effect was shown in Figure 3.4-6, as this helps to highlight the point of maximum net system efficiency. Operation at high S to C ratios is also not desirable as it has a negative effect on net system and stack efficiencies.

Effect of Inlet Cathode Temperature to Stack

The simulation predicted an increase in efficiency as the temperature of the cathode stream to the stack increased, as seen in Figure 3.4-7. The higher temperature cathode feed stream increased the temperature of the stack and this resulted in an increase in the stack voltage and power output. The increase in stack power contributed to the rise in the net and stack efficiencies. A higher inlet temperature to the SOFC cathode also resulted in a lower cathode exhaust post-recuperator temperature to the burner and a lower system exhaust temperature as seen in Figure 3.4-7.

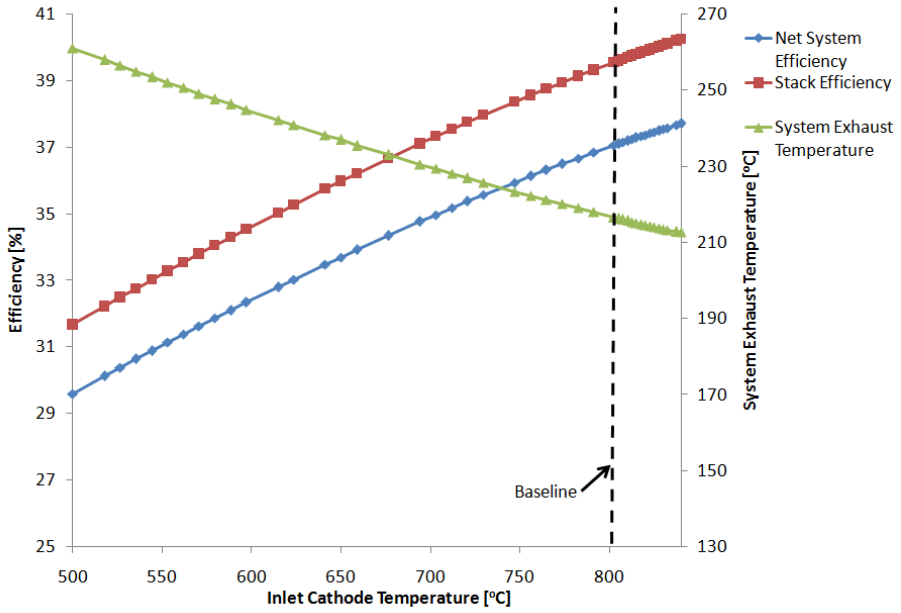

Figure 3.4-7: Effect of Inlet Cathode Temperature on Performance Metrics

Effect of ATR Pre-heater Approach Temperature

The lower the approach temperature (or the larger the heat-transfer surface area in the heat-exchanger) in the ATR pre-heater, the more effective is the heat-exchange. A lower approach temperature in the heat-exchanger resulted in an increase in the temperature of the ATR feed (Figure 3.4-8). This means a smaller feed fuel flow rate was required to maintain the set fuel utilization with a greater hydrogen concentration at the ATR exit. An increase in stack power was also observed with a rise in the stack temperature. The overall effect was once again an increase in the net system efficiency and stack efficiency. The system exhaust temperature decreased in a linear fashion with a lower approach temperature as pre-heating requirements were raised, which would be expected as more heat is recovered from the burner exhaust.

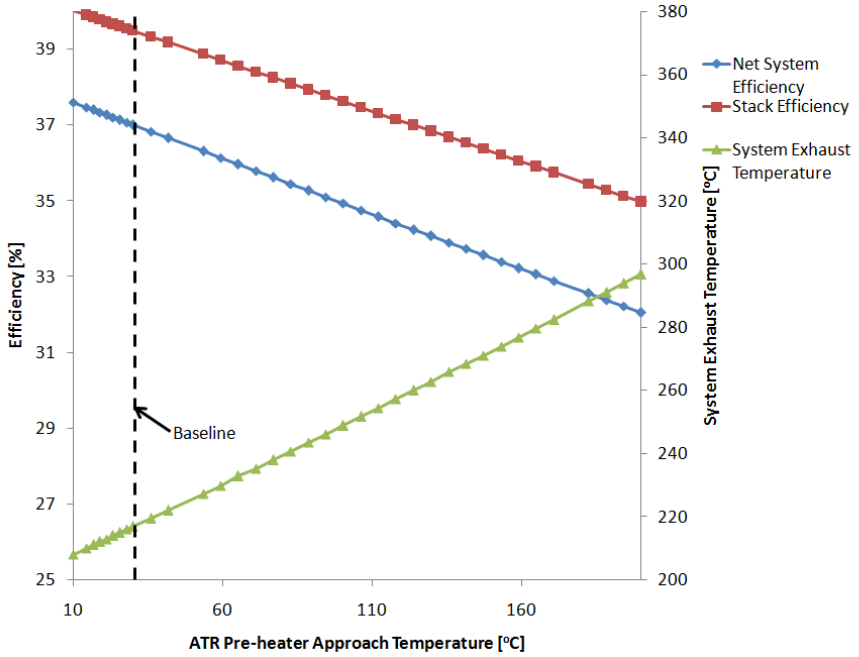

Figure 3.4-8: Effect of ATR Pre-heater Approach Temperature on Performance Metrics

Higher approach temperatures also significantly influenced the hydrogen yield and; therefore, a maximum approach temperature of approximately 200 ^{o}C was used in the simulation case-study, based on the constraints listed in Table 3.4-2. Thus, a highly integrated heat-exchanger setup is important from a design standpoint in order to achieve high net system and stack efficiencies. Furthermore, the steam reforming reaction is favorable at lower approach temperatures and a lower O_2 to C ratio can be used to produce the same amount of hydrogen.

3.5 Multi-Variable Study

The sensitivity of the predicted system performance on each of the independent variables that were studied was quantitatively assessed to produce a sensitivity ranking. The sensitivity rankings were determined using two different methods and are

presented in Table 3.5-1. In the first case, a Sensitivity Index (SI) was calculated based on finding the difference in the maximum and minimum output value when evaluating one input variable over its entire range [59-60] and is expressed by (3.5.1), where *D* represents the output value of the performance metric (*Method 1*). In *Method 2*, localized sensitivities were determined by varying input variables one at a time by 5% above and below their base case values and determining the corresponding ratio of the difference in input and output. According to Hamby (1994) [59-60], for a moderate number of independent variables, the SI is the easiest and most reliable sensitivity measure as it can be calculated without detailed knowledge about the variable and without the use of random sampling techniques. For each method in Table 3.5-1, the top three ranked independent variables are presented in order of decreasing sensitivity.

$$\frac{D_{max} - D_{min}}{D_{max}} \tag{3.5.1}$$

Table 3.5-1: Assessment of Sensitivities

Performance Measure	Method 1	Method 2
System Exhaust Temperature	S to C Ratio, U_f, O_2 to C Ratio	O_2 to C Ratio, U_f, U_a
Net System Efficiency	U_a, Cathode Inlet Temperature, U_f	U_a, O_2 to C Ratio, U_f
Stack Efficiency	U_a, U_f, O_2 to C Ratio	O_2 to C Ratio, U_a, U_f

A repeated occurrence of top ranked independent variables was observed in the rankings obtained from both methods. The system exhaust temperature was found to be the most sensitive to changes in the S to C ratio, O_2 to C ratio and U_f. On the other hand, the net system and stack efficiencies were most sensitive to the O_2 to C ratio, U_a and U_f. In order to better understand the behaviour of the system around the base-

case settings, two pairs of independent variables were chosen from Table 3.5-1. A multi-variable study was then carried out based on the constraints from Table 3.4-2 and for a constant current density. In one case, U_f and U_a were varied simultaneously to determine the highest net and stack efficiencies among the data collected. Similarly, U_f and S to C ratio were varied to obtain the lowest system exhaust temperature among the data collected. The two cases were plotted in the three-dimensional surface plots in Figures 3.5-1 and 3.5-2, based on a total of 258 and 232 data points collected, respectively. Table 3.5-2 lists the ranges over which the independent variables (U_f, U_a and S to C ratio) were simulated.

Table 3.5-2: Independent Variable Simulation Ranges

Independent Variable	Minimum	Maximum
$\boldsymbol{U_f}$	0.5 (50%)	0.9 (90%)
$\boldsymbol{U_a}$	0.25 (25%)	0.5 (50%)
S to C ratio	3	4.5

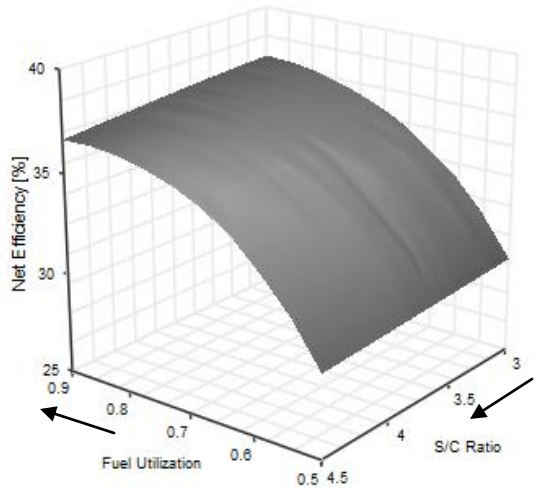

(a) Net System Efficiency

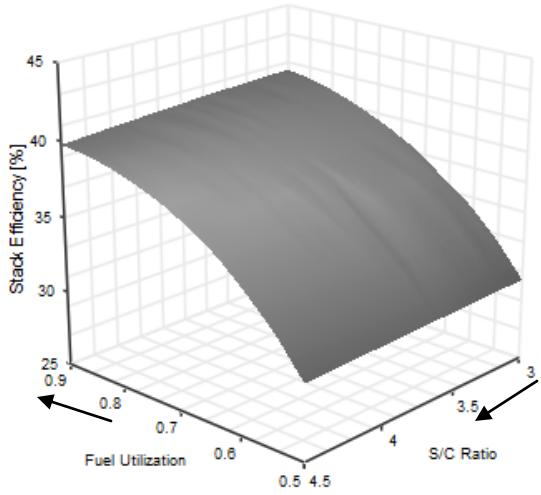

(b) Stack Efficiency

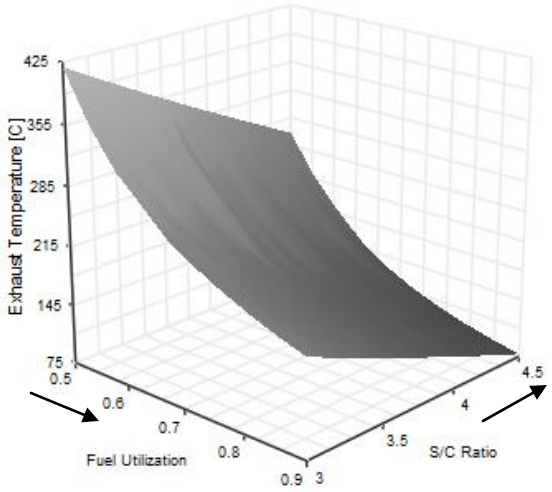

(c) System Exhaust Temperature

Figure 3.5-1: Fuel Utilization-S to C Ratio Interaction Effects; (a) Net System Efficiency (b) Stack Efficiency (c) System Exhaust Temperature

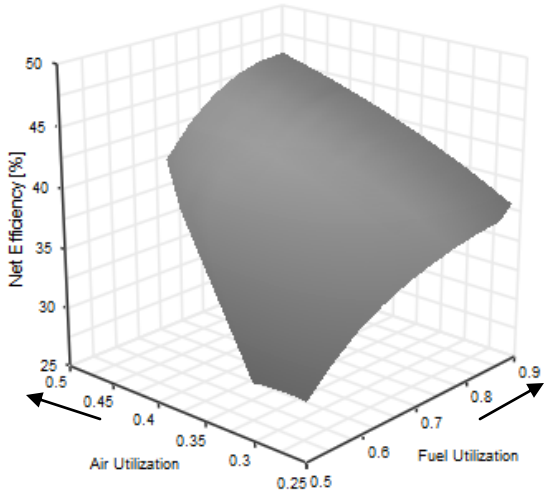

(a) Net System Efficiency

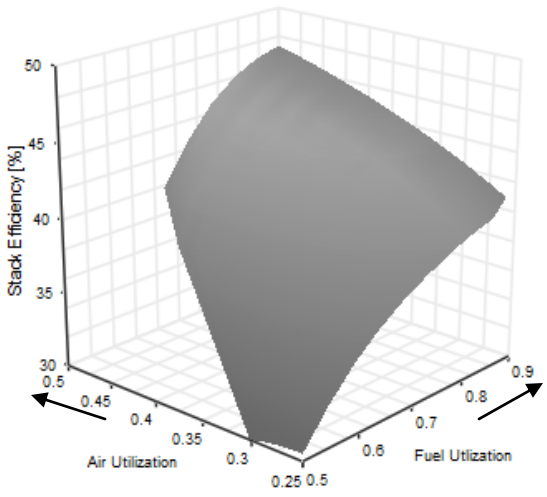

(b) Stack Efficiency

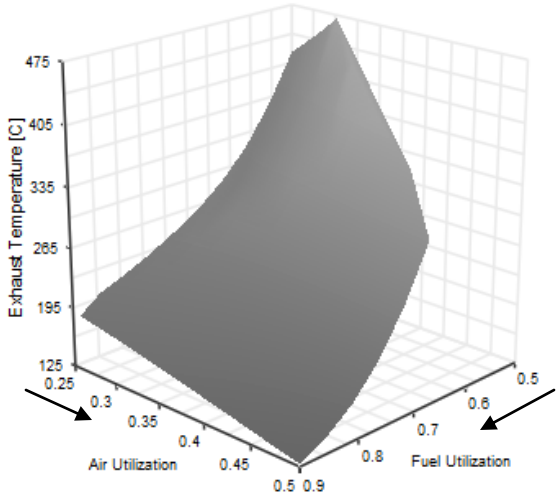

(c) System Exhaust Temperature

Figure 3.5-2: Fuel Utilization-Air Utilization Interaction Effects; (a) Net System Efficiency (b) Stack Efficiency (c) System Exhaust Temperature

The relationships observed in the surface plots above were generally similar to the original sensitivity analysis where the independent variables were varied one at a time. The exception to this was the observed relationship between U_f, U_a and the system exhaust temperature. In Figure 3.5-2, at lower values of U_f and for a fixed current density, additional fuel entered the burner and resulted in an increased burner exhaust

temperature. Secondly, at lower U_f values, the result of a large increase in the stack temperature with an increasing U_a was an increase in the system exhaust temperature. The result was different from what was observed over the majority of the base-case sensitivity analysis (at a fixed U_f; 80%), where the system exhaust temperature decreased with an increasing U_a. The trend is shown again in Figure 3.5-3 for clarity. The stack temperature was constrained to <1000 ^{o}C in the analysis and, therefore, not all points over the U_a range (25-50%) were included in the figures. Knowledge about the range beyond which stack overheating occurs would be important when designing process control strategies.

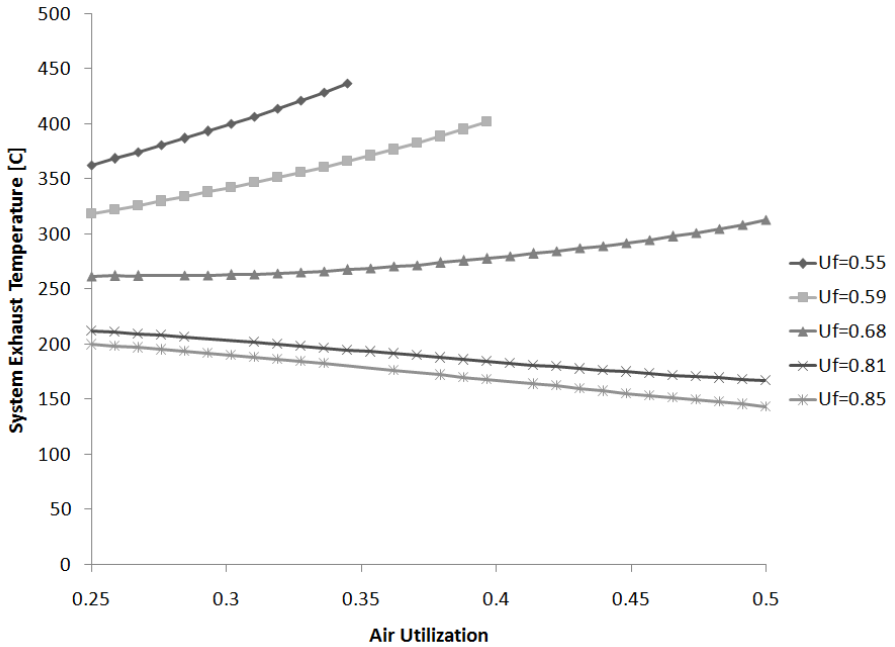

Figure 3.5-3: Fuel Utilization-Air Utilization: Influence on System Exhaust Temperature

The constrained optimum values of the performance metrics over the simulation range as determined from the surface plots and based on the constraints in Table 3.4-2 are

listed in Table 3.5-3. The lowest exhaust temperature was observed at a high U_f and S to C. The highest net and stack efficiencies were observed at a high U_f and also a high U_a. The net efficiencies observed lie within the range of efficiencies reported by Delphi for their small-scale APU systems using CPOX reformers [61]. Baratto *et al.* [38], as mentioned in Chapter 2, also have reported net efficiencies close to 40% in their simulation of a 5 kW diesel-fueled SOFC APU with an ATR fuel processor.

Table 3.5-3: Constrained Optimum Values of Performance Metrics over the Simulation Range

	Net System Efficiency [%]	Stack Efficiency [%]	System Exhaust Temperature [^{o}C]
Net and Stack Efficiency Maximum[2]	45	47	128
System Exhaust Temperature Minimum[3]	37	40	78

[2] U_f = 0.9, U_a = 0.5, S to C = 3, [3] U_a = 0.25, U_f = 0.9, S to C = 4.5

It should be noted that this analysis has focused on the three highest ranked operating variables in terms of system performance sensitivity. To obtain the global optimum of the system performance, more than two design variable interactions would need to be analyzed.

Chapter 4

Component Modeling Studies

The sensitivity analysis in the previous chapter provides some insight into independent variables that have the greatest impact on system performance. The simulation, however, did not consider spatial variations in momentum, mass and heat flows in the unit-operations. This included burner and reformer unit-operations in the process simulation that were modeled as Gibbs reactors.

One of the goals of the SOFC Canada (SOFCC) NSERC Strategic Network is to develop a cost-effective fuel processor design for diesel fuel [29]. There has been a active interest in developing effective coke and sulphur tolerant catalysts for fuel processing of diesel fuel [56, 62]. The case study presented in this chapter compares two kinetic models for diesel SR in a Catalytic Plate Reactor (CPR) at steady-state, using COMSOL Multiphysics^{TM} CFD software. The temperature, concentration and effectiveness factor profiles along the length of the reactor were obtained for co-current operation using a coupling of momentum, mass and heat transport equations.

4.1 Model Development

4.1.1 Model Geometry, Assumptions, Initial Conditions, Transport Equations and Boundary Conditions

Most reactors for steam reforming of hydrocarbons operate in the 700 ^{o}C to 900 ^{o}C degree range and require the use of expensive high-temperature alloy materials (on

the order of $100 per-lb) for durability and stability. Catacel™ technology, which manufactures CPRs, uses Fecralloy™ for its plate construction and the cost is significantly less. In comparison to ceramic and modified ceramic heat transfer media, Fecralloy can provide the same heat transfer performance and a much higher surface area with only a modest pressure drop [63].

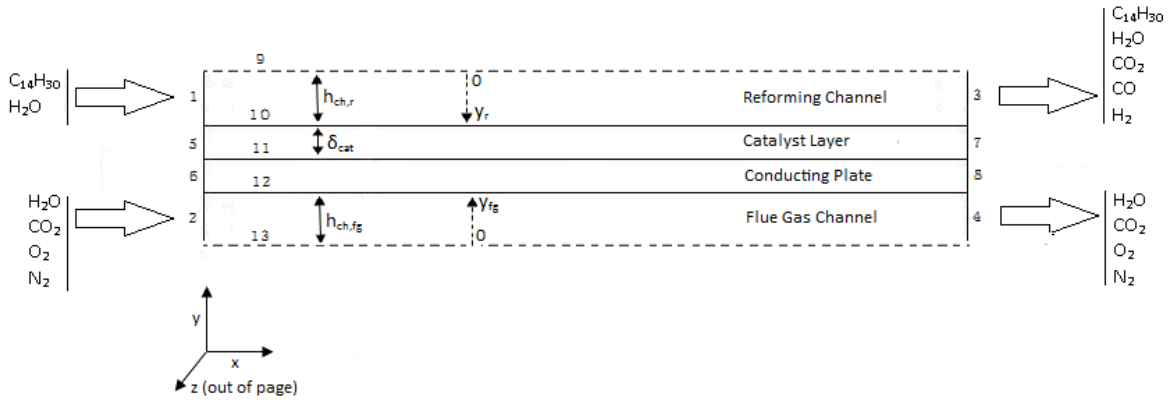

Figure 4.1-1: Catalytic Plate Reactor Geometry (Not to Scale)

In the two-dimensional geometry of the CPR that was modeled in this study (Figure 4.1-1), the properties of a Fecralloy variant were used for the conducting plate. The geometry consisted of four domains; the reforming channel, reforming channel catalyst layer, a conducting plate and a flue gas channel. In the model, a surrogate of diesel (tetradecane) and steam was fed to the reforming channel at a specified S to C ratio. The flue gas stream served as a heat source for the reforming reaction. The flue gas stream consists primarily of H_2O, CO_2 and excess or un-reacted air from the burner of the SOFC system as seen in the system simulation in the previous chapter. The dimensions provided in Table 4.1-1 were similar to the dimensions of the Catacel CPR [64] for a single plate. A catalyst thickness of 0.09 mm was used [48].

The mass, momentum and heat transfer gradients along the width of the channel (z-direction) were assumed to be negligible. In addition, the plate width in the z-direction is considered long enough such that flow between two infinite parallel plates was considered [65-66]. The overall modeling domain was, therefore, reduced to a two-dimensional reactor.

Table 4.1-1: Catalytic Plate Reactor Dimensions

Half-Channel Height	1 mm
Half-Channel Length	25 cm
Plate Thickness	0.127 mm

The following assumptions were applied for the modeling study. The initial conditions for the base-case settings are described in Table 4.1-2.

- Ideal gas law.
- A single plate used to represent the entire reactor (consisting of multiple stacked plates), due to the symmetry conditions at the centreline of the channels.
- Fully developed laminar flow in both half- channels.
- No thermal cracking and carbon formation reactions.
- All reactions take place in the catalyst layer.
- No intra-phase diffusion limitations in the catalyst.
- Negligible pressure drop along the channels
- Body forces neglected

Table 4.1-2: Catalytic Plate Reactor Initial Conditions

$T_{in,r}$	1073.15 [K]
$T_{in,fg}$	1273.15 [K]
$P_{out,fg}$, $P_{out,r}$	101325 [Pa]
$u_{in,r}$	0.3 [m/s]
$u_{in,fg}$	1 [m/s]
S to C	3
$X_{in,r}$	$X_{C_{14}H_{30}}$ = 0.0233, X_{CO} = 0 X_{CO_2} = 0, X_{H_2O} = 0.967, X_{H_2} = 0
$X_{in,fg}$	X_{H_2O} = 0.201, X_{CO_2} = 0.068 X_{O_2} = 0.094, X_{N_2} = 0.637

Species thermal conductivities, heat capacities and viscosities were calculated as a function of temperature, as shown in the following expressions [67]. The letters $A-E$ in (4.1.1) through (4.1.3) are regression coefficients for species i. Details are shown in Appendix B.

$$C_{pi} = A + BT + CT^2 + DT^3 + ET^4 \tag{4.1.1}$$

$$k_i = A + BT + CT^2 \tag{4.1.2}$$

$$\mu_i = A + BT + CT^2 \tag{4.1.3}$$

The mixture heat capacity was evaluated using the weighted average heat capacity of the gaseous mixture. The thermal conductivity of low pressure gas mixtures is based on the Wassiljewa expression [68]. The effective thermal conductivity of the catalyst layer was calculated using (4.1.4) [69]. The gas mixture viscosity was evaluated using the Herning and Zipperer (1936) correlation at low pressures [68].

$$k_{eff} = \phi k_g + k_s(1-\phi) \tag{4.1.4}$$

The plate properties in Table 4.1-3 were obtained from the Material Property Database [70] and were based on a Fecralloy^{TM} variant (Fe 73/Cr 22/Al 4.8). The catalyst properties are also presented in Table 4.1-3. The same catalyst properties (permeability, porosity, pore radius, tortuosity and thermal conductivity) were applied to both kinetic models. The solid catalyst thermal conductivity was approximated based on the Pt on Alumina catalyst. This resulted in an effective conductivity (of gas-phase and catalyst-phase) on the order of 4.5 W/m.K. The effective conductivity value lies within the range of thermal conductivities studied by Shi *et al.* for the Pt on CeO_2 and Gd_2O_3 catalyst.

Table 4.1-3: Catalyst and Plate Properties

Catalyst Properties		**Plate Properties**[5]	**Fecralloy^{TM} (Fe 73/Cr 22/Al 4.8)**
Porosity	0.5[4]	**Heat Capacity**	460 [J kg^{-1} K^{-1}]
Tortuosity	4[4]	**Thermal Conductivity**	16 W [m^{-1} K^{-1}]
Permeability	1E-9 [m^2][3]	**Density**	7169 [kg m^{-3}]
Pore Radius	15E-9 [m][4]		
Density	2053 [kg m^{-3}][1], 3867 [kg m^{-3}][2]		
Thermal Conductivity	8.9 [W m^{-1} K^{-1}][1]		

[1][57], [2][69], [3][71], [4][48], [5][70]

Both bulk and Knudsen diffusion were considered (4.1.7) in the catalyst layer to account for diffusion in the catalyst pore structure whereas only bulk diffusion (4.1.5) was considered in the reforming channel. Knudsen diffusion is dominant in the catalyst layer, where collisions between the gas molecules and the walls of the catalyst pores are significant. Bulk diffusion, on the other hand, considers transport in large pores such that molecule-molecule collisions are dominant in comparison to molecule-wall collisions [72]. The Fuller equation was used to obtain bulk diffusion coefficients for

each species. The species binary diffusion coefficients were calculated with respect to H_2O and are described as follows. The Knudsen diffusion coefficient is expressed by (4.1.6) [73]:

$$D_{ij} = \frac{0.01013T^{1.75}\left(\left(1/M_i\right)+\left(1/M_j\right)\right)^{0.5}}{P\left(v_i^{1/3}+v_j^{1/3}\right)^2} \tag{4.1.5}$$

$$D_{kn,i} = 97R_p\left(T/M_i\right)^{0.5} \tag{4.1.6}$$

$$D_{eff} = \phi/\tau\left(1/D_{ij} + 1/D_{kn,i}\right) \tag{4.1.7}$$

The CPR was modeled using COMSOL Multiphysics™. The partial differential equations for the CPR model used by COMSOL for the transport of momentum, mass and heat are presented in Table 4.1-4, by considering spatial variations at steady state. These are commonly used equations in CFD modeling and can be found in a number of textbooks [65-66]. The Navier-Stokes/Brinkman equations were used to solve for momentum transport in the porous catalyst layer. The no slip condition in Table 4.1-4 represents a zero fluid velocity relative to the associated boundary.

Table 4.1-4: Transport Equations and Boundary Conditions

refer to Figure 4.1-1 and Table 4.1-2 for boundary conditions

a. *Reforming Channel*

i. Momentum Transport

$$\rho_{mix}\left(u_x\frac{\partial u_x}{\partial x}+u_y\frac{\partial u_x}{\partial y}\right)=-\frac{\partial P}{\partial x}+\mu_{mix}\frac{\partial}{\partial x}\left(2\frac{\partial u_x}{\partial x}-\frac{2}{3}\left(\frac{\partial u_x}{\partial x}+\frac{\partial u_y}{\partial y}\right)\right)+\mu_{mix}\frac{\partial}{\partial y}\left(\frac{\partial u_x}{\partial y}+\frac{\partial u_y}{\partial x}\right)$$

$$\rho_{mix}\left(u_x\frac{\partial u_y}{\partial x}+u_y\frac{\partial u_y}{\partial y}\right)=-\frac{\partial P}{\partial y}+\mu_{mix}\frac{\partial}{\partial x}\left(\frac{\partial u_x}{\partial y}+\frac{\partial u_y}{\partial x}\right)+\mu_{mix}\frac{\partial}{\partial y}\left(2\frac{\partial u_y}{\partial y}-\frac{2}{3}\left(\frac{\partial u_x}{\partial x}+\frac{\partial u_y}{\partial y}\right)\right)$$

ii. Continuity Equation

$$\frac{\partial\left(\rho_{mix}u_x\right)}{\partial x}+\frac{\partial\left(\rho_{mix}u_y\right)}{\partial y}=0$$

iii. Ideal Gas Equation of State

$$\rho_{mix}=\frac{P\sum X_iM_i}{RT}$$

iv. Mass Transport

$$c_i\left(\frac{\partial u_x}{\partial x}+\frac{\partial u_y}{\partial y}\right)+u_x\frac{\partial c_i}{\partial x}+u_y\frac{\partial c_i}{\partial y}-D_{i,j}\frac{\partial}{\partial x}\left(\frac{\partial c_i}{\partial x}\right)-D_{i,j}\frac{\partial}{\partial y}\left(\frac{\partial c_i}{\partial y}\right)=0$$

v. Heat Transport

$$-k_{mix}\frac{\partial}{\partial x}\left(\frac{\partial T}{\partial x}\right)-k_{mix}\frac{\partial}{\partial y}\left(\frac{\partial T}{\partial y}\right)+\rho_{mix}C_{p,mix}\left(u_x\frac{\partial T}{\partial x}+u_y\frac{\partial T}{\partial y}\right)=0$$

Boundary Conditions

1. Inlet Conditions
   - inlet velocity profile: $u_x=1.5u_{x,in,r}\left[1-\left(\frac{y_r}{h_{ch,r}}\right)^2\right]$
   - inlet concentration: $c_{i,b1}=c_{i,in,r}$
   - inlet temperature: $T_{b1}=T_{in,r}$
2. Outlet Conditions
   - outlet pressure: $P_{b3}=P_{out,r}$
   - no viscous stress
   - zero flux: $\frac{\partial c_{i,b3}}{\partial x}=\frac{\partial T_{b3}}{\partial x}=0$
3. Channel Centre
   - symmetry: $\frac{\partial u_{x,b9}}{\partial y}=\frac{\partial c_{i,b9}}{\partial y}=\frac{\partial T_{b9}}{\partial y}=0$
4. Channel Wall

- no slip: $u_{x,b11} = 0$
- zero flux: $\frac{\partial c_{i,b11}}{\partial y} = 0$

b. *Catalyst Layer*

i. Momentum Transport

$$\frac{\mu_{mix}}{\kappa} u_x = -\frac{\partial P}{\partial x} + \frac{\mu_{mix}}{\phi}\frac{\partial}{\partial x}\left(2\frac{\partial u_x}{\partial x} - \frac{2}{3}\left(\frac{\partial u_x}{\partial x} + \frac{\partial u_y}{\partial y}\right)\right) + \frac{\mu_{mix}}{\phi}\frac{\partial}{\partial y}\left(\frac{\partial u_x}{\partial y} + \frac{\partial u_y}{\partial x}\right)$$

$$\frac{\mu_{mix}}{\kappa} u_y = -\frac{\partial P}{\partial y} + \frac{\mu_{mix}}{\phi}\frac{\partial}{\partial x}\left(\frac{\partial u_x}{\partial y} + \frac{\partial u_y}{\partial x}\right) + \frac{\mu_{mix}}{\phi}\frac{\partial}{\partial y}\left(2\frac{\partial u_y}{\partial y} - \frac{2}{3}\left(\frac{\partial u_x}{\partial x} + \frac{\partial u_y}{\partial y}\right)\right)$$

ii. Continuity Equation (same as ***a.***)

$$\frac{\partial(\rho_{mix} u_x)}{\partial x} + \frac{\partial(\rho_{mix} u_y)}{\partial y} = 0$$

iii. Ideal Gas Equation of State (same as ***a.***)

$$\rho_{mix} = \frac{P\sum X_i M_i}{RT}$$

iv. Mass Transport

$$c_i\left(\frac{\partial u_x}{\partial x} + \frac{\partial u_y}{\partial y}\right) + u_x\frac{\partial c_i}{\partial x} + u_y\frac{\partial c_i}{\partial y} - D_{i,j}\frac{\partial}{\partial x}\left(\frac{\partial c_i}{\partial x}\right) - D_{i,j}\frac{\partial}{\partial y}\left(\frac{\partial c_i}{\partial y}\right) = r_i$$

v. Heat Transport

$$-k_{eff}\frac{\partial}{\partial x}\left(\frac{\partial T}{\partial x}\right) - k_{eff}\frac{\partial}{\partial y}\left(\frac{\partial T}{\partial y}\right) + \rho_{mix} C_{p,mix}\left(u_x\frac{\partial T}{\partial x} + u_y\frac{\partial T}{\partial y}\right) = \sum\left(-\Delta H_k r_k\right)$$

Boundary Conditions

1. Inlet Conditions
   - no slip: $u_{x,b5} = 0$
   - zero flux: $\frac{\partial c_{i,b5}}{\partial x} = \frac{\partial T_{b5}}{\partial x} = 0$
2. Outlet Conditions
   - no slip: $u_{x,b7} = 0$
   - zero flux: $\frac{\partial c_{i,b7}}{\partial x} = \frac{\partial T_{b7}}{\partial x} = 0$
3. Catalyst Surface ($y = y_r$)
   - continuity: momentum, mass and heat flux components normal to the boundary are continuous across the boundary; $N_1 - N_2 = 0$

c. *Plate*

i. Heat Transport

$$\frac{\partial^2 T}{\partial x^2} + \frac{\partial^2 T}{\partial y^2} = 0$$

Boundary Conditions

1. Inlet Condition, $\frac{\partial T_{b6}}{\partial x} = 0$
2. Outlet Condition, $\frac{\partial T_{b8}}{\partial x} = 0$
3. Reforming Channel Wall
   - continuity: heat flux components normal to the boundary are continuous across the boundary; $N_1 - N_2 = 0$
4. Flue Gas Channel Wall,
   - continuity: heat flux components normal to the boundary are continuous across the boundary; $N_1 - N_2 = 0$

d. *Flue Gas Channel*

i. Momentum Transport (same as ***a.***)

$$\rho_{mix}\left(u_x\frac{\partial u_x}{\partial x} + u_y\frac{\partial u_x}{\partial y}\right) = -\frac{\partial P}{\partial x} + \mu_{mix}\frac{\partial}{\partial x}\left(2\frac{\partial u_x}{\partial x} - \frac{2}{3}\left(\frac{\partial u_x}{\partial x} + \frac{\partial u_y}{\partial y}\right)\right) + \mu_{mix}\frac{\partial}{\partial y}\left(\frac{\partial u_x}{\partial y} + \frac{\partial u_y}{\partial x}\right)$$

$$\rho_{mix}\left(u_x\frac{\partial u_y}{\partial x} + u_y\frac{\partial u_y}{\partial y}\right) = -\frac{\partial P}{\partial y} + \mu_{mix}\frac{\partial}{\partial x}\left(\frac{\partial u_x}{\partial y} + \frac{\partial u_y}{\partial x}\right) + \mu_{mix}\frac{\partial}{\partial y}\left(2\frac{\partial u_y}{\partial y} - \frac{2}{3}\left(\frac{\partial u_x}{\partial x} + \frac{\partial u_y}{\partial y}\right)\right)$$

ii. Continuity Equation (same as **a.**)

$$\frac{\partial(\rho_{mix}u_x)}{\partial x} + \frac{\partial(\rho_{mix}u_y)}{\partial y} = 0$$

iii. Ideal Gas Equation of State (same as **a.**)

$$\rho_{mix} = \frac{P\sum X_i M_i}{RT}$$

iv. Heat Transport (same as ***a.***)

$$-k_{mix}\frac{\partial}{\partial x}\left(\frac{\partial T}{\partial x}\right) - k_{mix}\frac{\partial}{\partial y}\left(\frac{\partial T}{\partial y}\right) + \rho_{mix}C_{p,mix}\left(u_x\frac{\partial T}{\partial x} + u_y\frac{\partial T}{\partial y}\right) = 0$$

Boundary Conditions

1. Inlet Conditions
   - inlet temperature: $T_{b2} = T_{in,fg}$
   - inlet velocity profile: $u_x = 1.5u_{x,in,fg}\left[1 - \left(\frac{y_{fg}}{h_{ch,fg}}\right)^2\right]$
2. Outlet Conditions
   - outlet pressure: $P_{b4} = P_{out,fg}$
   - no viscous stress

- zero flux: $\frac{\partial T_{b4}}{\partial x} = 0$

3. Channel Centre
   - symmetry: $\frac{\partial u_{x,b13}}{\partial y} = \frac{\partial T_{b13}}{\partial y} = 0$
4. Channel Wall
   - no slip: $u_{x,b12} = 0$

4.1.2 Reaction Kinetics

The reaction rate term, r_i in Table 4.1-4 requires knowledge about steam reforming kinetics for diesel fuel. Only a small number of kinetic models for steam reforming of diesel fuel are available in the current literature [57, 69, 74-76], two of which were studied in the current work [57, 69]. From these, an experimentally validated mechanistic kinetic model by Parmar *et al*. [57] was applied to the CPR geometry and compared with a second model by Shi *et al.* [69] on the basis of reactor performance. The main differences are highlighted in Table 4.1-5. Both use a Platinum based catalyst with different catalyst supports. The rate expressions were based on the global reactions (4.1.8) to (4.1.10). Parmar *et al.*, however, considered the steam reforming of diesel to CO_2 as a dependant reaction (4.1.10). Lastly, hexadecane was used as a diesel surrogate by Shi *et al.* whereas tetradecane was used by Parmar *et al.* In this work, tetradecane was chosen as the surrogate in the simulation for both kinetic models. Details about the rate expressions can be found in the quoted references [57, 69]. The rate expressions for the kinetic models were used without any parameter modifications. It should be noted that both models were originally based on auto-

thermal reforming. The combustion kinetics, however, were dropped from the model and only steam reforming kinetics was considered.

Table 4.1-5: Underlying Differences in Kinetic Models

	Shi *et al.* [69]	Parmar *et al.* [57]
Catalyst Support	Cerium Oxide, Gadolinium Oxide	Alumina
Number of Independent Reactions	Three	Two
Diesel Surrogate	Hexadecane	Tetradecane

$$C_aH_b + aH_2O \rightarrow aCO + \left(\frac{2a+b}{2}\right)H_2 \qquad \Delta H > 0 \tag{4.1.8}$$

$$CO + H_2O \rightarrow CO_2 + H_2 \qquad \Delta H < 0 \tag{4.1.9}$$

$$C_aH_b + 2aH_2O \rightarrow aCO_2 + \left(\frac{4a+b}{2}\right)H_2 \qquad \Delta H > 0 \tag{4.1.10}$$

4.2 Modeling Results and Discussion

In this section, CFD results for the CPR simulation are presented and compared for both kinetic models using a co-current flow arrangement. The reforming species concentration profiles, comparisons with equilibrium data, the influence of reactor residence time and the inlet reforming temperature on fuel conversion, and the evolution of reforming effectiveness factors along the axial coordinate are described. The difference in co-current and counter-current modes of operation is also studied in the context of achieving a near-isothermal temperature distribution.

The standard mesh size for the CPR models consisted of 40,051 triangular elements. More mesh elements were used near the entrance of the reforming channel and the

catalyst layer due to larger variations in the reaction rates and thermal gradients. The CPR simulation was rerun, using on the order of 120,000 triangular mesh elements. The increase in the number of elements corresponds to an increase in the degrees of freedom by a factor greater of approximately three. A maximum percentage difference in the exit hydrogen mole fractions of less than 1% was observed for both kinetic models using the two different mesh sizes. Thus the original mesh of 40,051 elements was retained for the study.

In the model solution, it was ensured that the conservation of mass in both the reforming and flue gas channels was satisfied (4.2.1). The fuel conversion was calculated as a function of the inlet and exit tetradecane mole fractions (4.2.2).

$$\int_0^{h_c} \rho_{mix} u_x dy\big|_{x=0} = \int_0^{h_c} \rho_{mix} u_x dy\big|_{x=L} \tag{4.2.1}$$

$$1 - \frac{\int_0^{h_c} X_{C_{14}H_{30}} dy\big|_{x=L}}{\int_0^{h_c} X_{C_{14}H_{30}} dy\big|_{x=0}} \tag{4.2.2}$$

Co-current versus Countercurrent Flow

The effect of flow arrangement on the heat transfer effects arising in the CPR from the endothermic reforming reaction was studied. Co-current and countercurrent flow operation modes were modeled by considering the same initial conditions and kinetic model (Parmar *et al.*). Figure 4.2-1 (a) and (b) present the transverse temperature difference profile along the length for the flow arrangements for both the reforming channel and the flue gas channel. The axial dimensionless coordinate references the

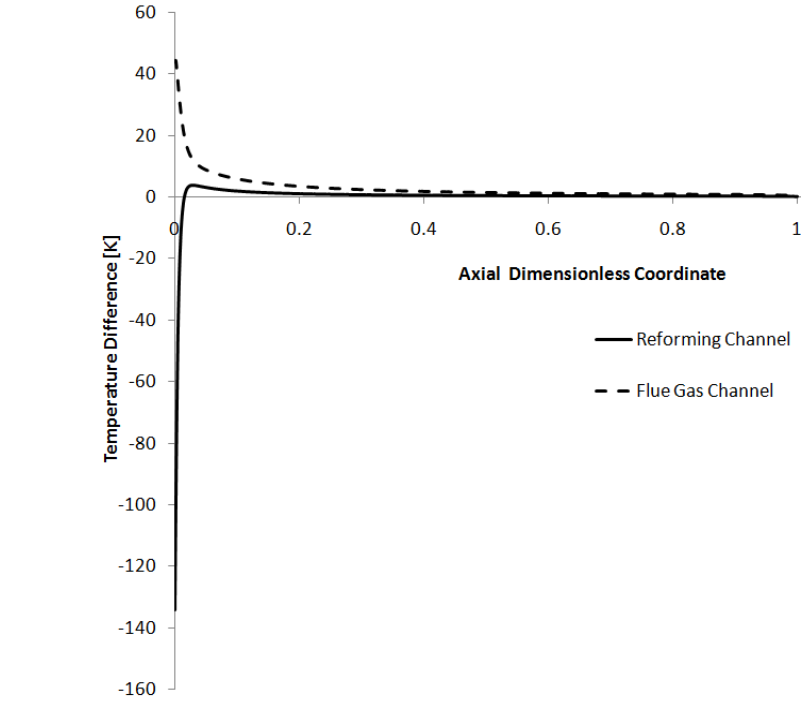

(a)

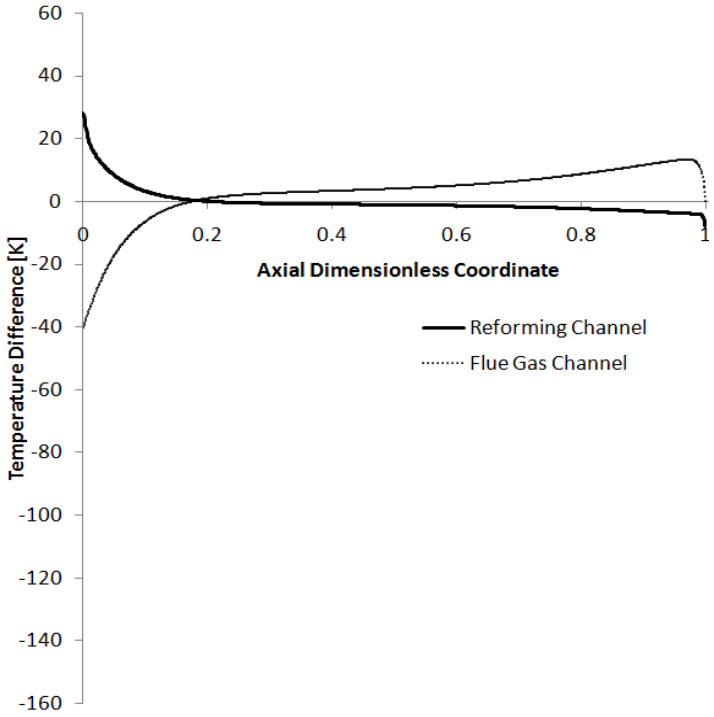

(b)

Figure 4.2-1: Transverse Temperature Difference (T_{centre} - T_{wall}) along Reforming Channel and Flue Gas Channel for (a) Co-Current and (b) Counter-Current Flow Arrangement

reforming channel side for both the co-current and countercurrent cases. In other words, the zero axial dimensionless coordinate represents the reforming channel inlet and the flue gas channel outlet for the countercurrent configuration. The transverse temperature difference in the CPR is defined as the difference between the temperature at the centerline/symmetry boundary of the channel and the adjacent plate wall.

In the co-current arrangement, the wall temperature is significantly greater than the adjacent reforming channel centre at the entrance and a maximum absolute difference of 135 K is observed. Within the first 1-2% of the reactor length, the difference becomes positive and the wall temperature becomes marginally smaller than the centre of the channel. A maximum positive transverse temperature difference of about 4 K is attained, after which the value tends to zero towards the reactor exit. The flue gas channel experiences a maximum transverse temperature difference of approximately 40 K at the channel entrance and also tends to zero towards the reactor exit. The temperature at the centerline of the flue gas channel is greater than the adjacent wall along the entire length. There is a region in the reactor, as is implied, where the temperature values in both the flue gas and reforming channel are greater than the adjacent plate walls. This is attributed to the temperature gradient across the catalyst thickness being approximately zero. Therefore, the conduction in the plate in this region takes place in the through-plane direction (along the length of the plate).

In the counter-current case in Figure 4.2-1 (b), the transverse temperature difference is less pronounced. A maximum absolute difference of approximately 30K is seen for the reforming channel and 40K for the flue gas channel. The temperature profiles for each channel along the reactor length are plotted in Figure 4.2-2, for co-current and countercurrent flow.

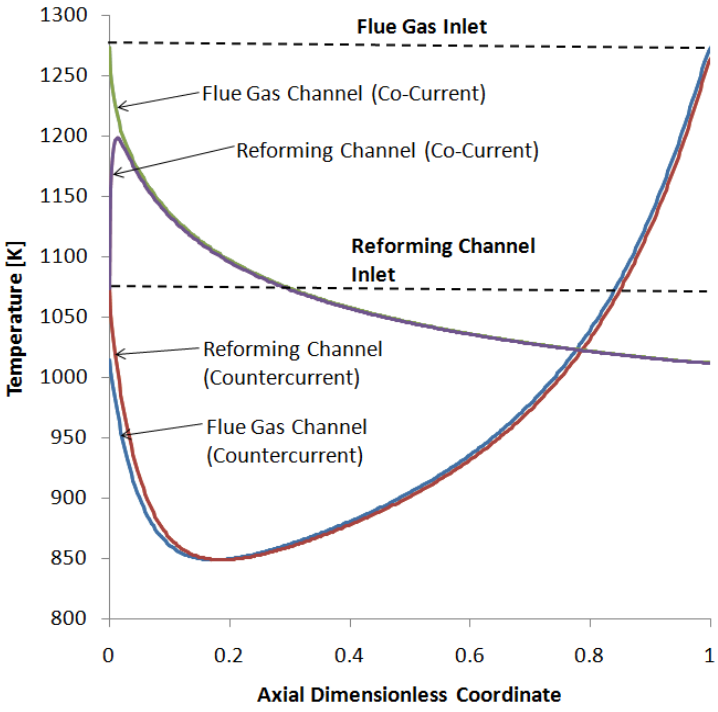

Figure 4.2-2: Co-Current and Counter-Current Temperature Profiles along Reactor Length for Reforming Channel and Flue Gas Channel

The dashed lines indicate the inlet temperature conditions for the reforming channel and flue gas channel. Operation within this region would be desirable for achieving closer-to-isothermal conditions. The counter-current arrangement results in a parabolic temperature profile along the reactor, and temperatures reaching as low as 850 K at approximately 20% of the axial dimensionless coordinate. Thus a low-temperature zone

is generated by the endothermic reforming reaction. The co-current arrangement, on the other hand, results in a lowest temperature of approximately 1000 K near the reactor exit. The reforming temperature along the reactor length is closer to the inlet reforming temperature of 1073 K and closer-to-isothermal conditions are thus achieved. The remainder of this chapter focuses on modeling results for a co-current flow arrangement.

Reforming Species Concentration Profiles

The reaction network in the reforming channel consisted of five species; $C_{14}H_{30}$, H_2, H_2O, CO and CO_2. The species concentration profiles in the reforming channel along the length of the reactor are illustrated in Figure 4.2-3, based on the initial conditions in Table 4.1-2. In the co-current arrangement, the bulk of the reaction occurs in the first 5-10% of the reactor length for Shi *et al.'s* case and approximately 20% in Parmar *et al.'s* case. The fast kinetics at the entrance can be advantageous from a design standpoint, for reducing the reactor length and consequently the material cost. Average fuel conversions of approximately 82% and 100%, respectively, were obtained at the reactor exit, using the Parmar *et al.* and Shi *et al.* kinetics models, for an average residence time of 700 ms. Larger residence times or an increase in reactor length would, however, be required to achieve the equilibrium hydrogen yield.

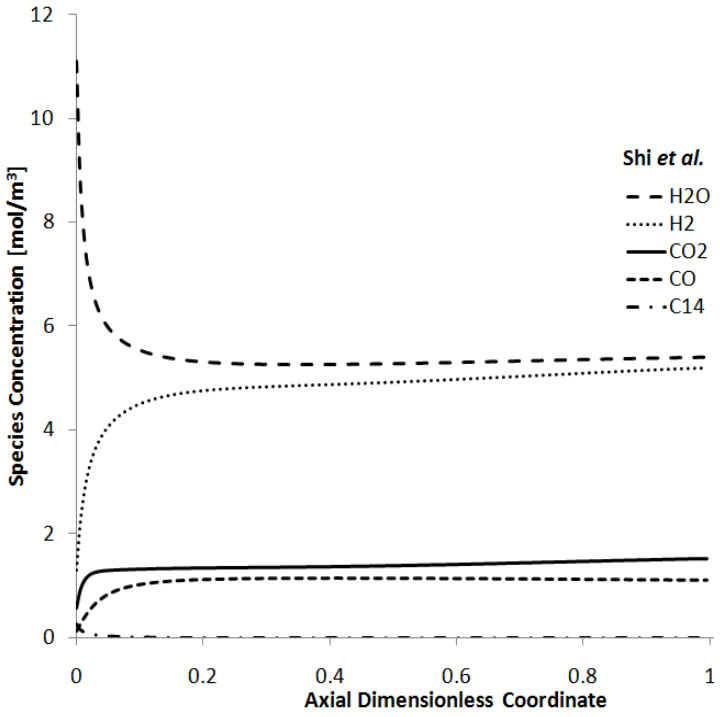

(a)

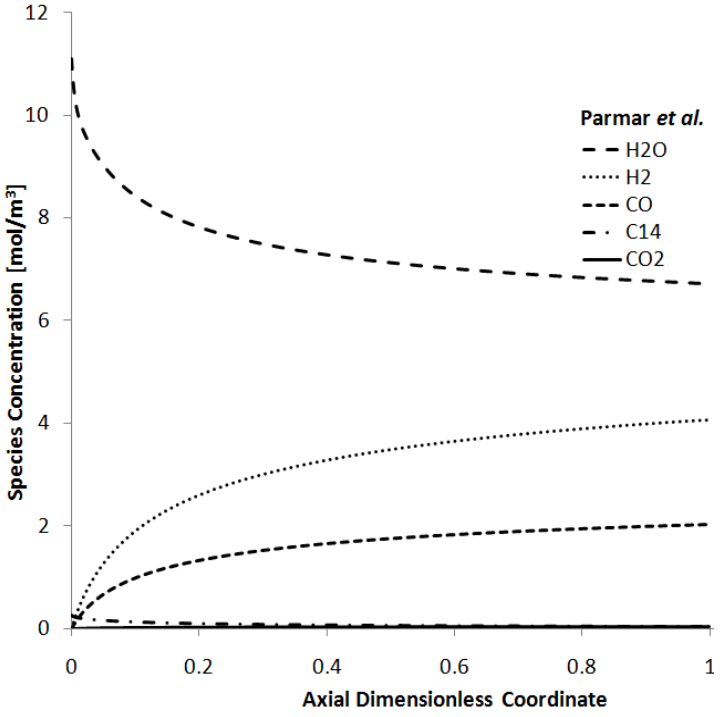

(b)

Figure 4.2-3: Reforming Channel Species Concentration Profiles for Co-Current Flow Arrangement; (a) Shi *et al.* (b) Parmar *et al.*

The primary difference in the concentration profiles for the reforming reaction was the concentration of CO_2. Parmar *et al.* did not consider the reforming of tetradecane to CO_2 and H_2 as an independent global reaction and therefore, a minimal concentration of CO_2 was observed at the reactor exit. Compared to Shi *et al.*, less hydrogen was produced and less steam was consumed.

Comparison with Equilibrium Data

The averaged mole fractions of H_2 and CO at the exit of the reforming channel from the CPR simulations were compared with equilibrium data obtained from VMGSim™, at various temperatures (Figure 4.2-4). The equilibrium analysis used the Gibbs free energy minimization approach to calculate the final species mole fractions. The analysis was based on the following species; H_2O, H_2, CO, CO_2, $C_{14}H_{30}$, CH_4, C_2H_4 and C_2H_6. The equilibrium comparison was based on the average temperature at the exit boundary of the reforming channel in the CPR simulation. In Figure 4.2-4, the equilibrium H_2 mole fraction decreased a small amount at higher reforming temperatures for the range of temperatures studied. This was attributed to the effect of the reverse WGS reaction, where some of the CO_2 and H_2 is converted back to H_2O and CO. Exit H_2 mole fractions using Shi *et al.'s* kinetic model were consistently higher than Parmar *et al.* and between 80 and 84% of the equilibrium values for the temperature range studied.

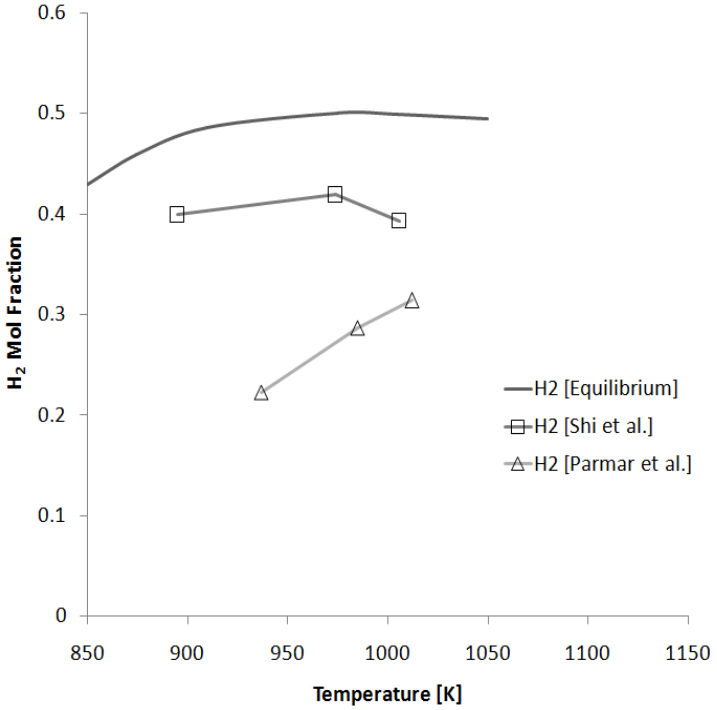

(a)

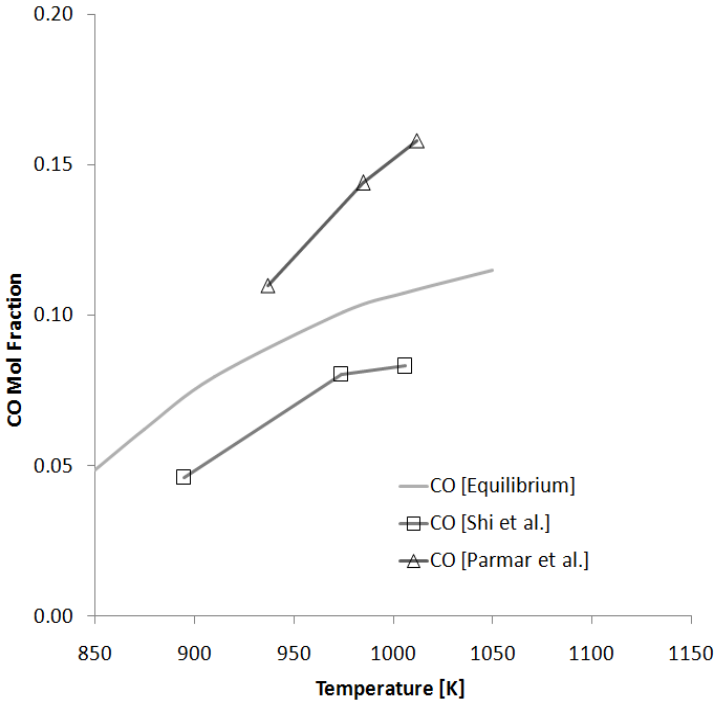

(b)

Figure 4.2-4: Comparison of Reforming Species Mole Fractions at the Reactor Exit with Equilibrium Data; (a) H_2 (b) CO

The H_2 mole fractions for both kinetic models also under-predicted the equilibrium data for the temperature range studied. The H_2 prediction was consistent with the prediction for the H_2O mole fraction. The H_2O mole fraction over-predicted the equilibrium data for both kinetic models.

Parmar *et al.* kinetics over-predicted the equilibrium CO mole fraction. The increase in the CO mole fraction with reforming temperature was again attributed to the effects of reverse WGS. Shi *et al.'s* kinetic model in contrast, under-predicted the equilibrium CO mole fraction. The difference in the equilibrium prediction between the two models is attributed to the CO_2 mole fraction. Shi *et al.'s* kinetic model over-predicted the CO_2 mole fraction whereas Parmar *et al.'s* model largely under-predicted the CO_2 mole fraction.

Influence of Residence Time and Inlet Reforming Temperature

The average residence time in the reforming channel was based on the average of the velocities at the reactor entrance and exit. Inlet velocities were varied from 0.1 to 4 m/s at inlet reforming temperatures of 773 and 1073 K as seen in Figure 4.2-5.

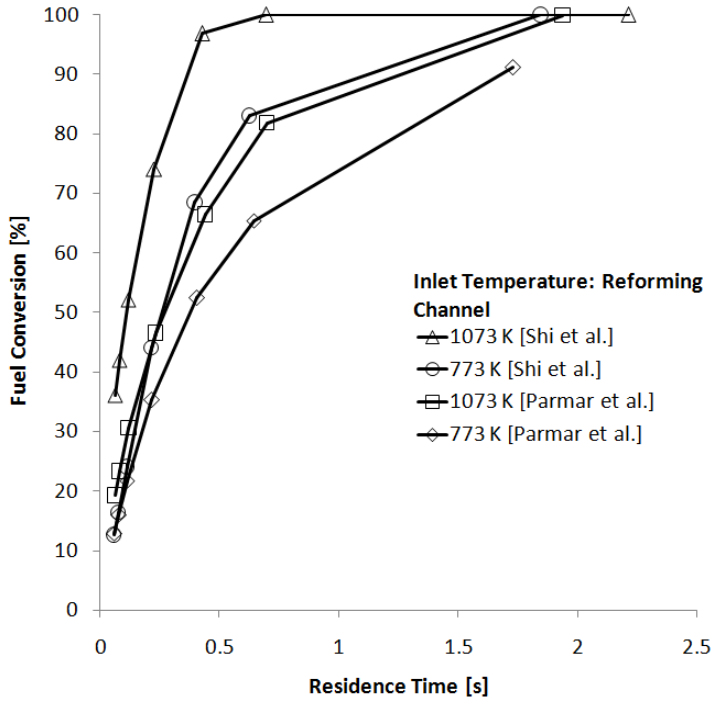

Figure 4.2-5: Influence of Residence Time on Fuel Conversion

Fuel (tetradecane) conversion increased with residence time in the reactor as expected. At 1073 K, 100% fuel conversion was achieved at a residence time of approximately 700 ms using Shi *et al.'s* model and 2 seconds using Parmar *et al.'s* model. Additionally, the fuel conversion as a function of inlet reforming temperature is shown in Figure 4.2-6. An increase in the fuel conversion was achieved at higher inlet reforming temperatures as would be expected because steam reforming is highly endothermic. Shi *et al.'s* model

predicted a higher fuel conversion in comparison to Parmar *et al.'s* model throughout the studied temperature range. The maximum difference between the predicted fuel conversion for the kinetic models of Parmar *et al.* and Shi *et al.* of approximately 25% was observed over the temperature range.

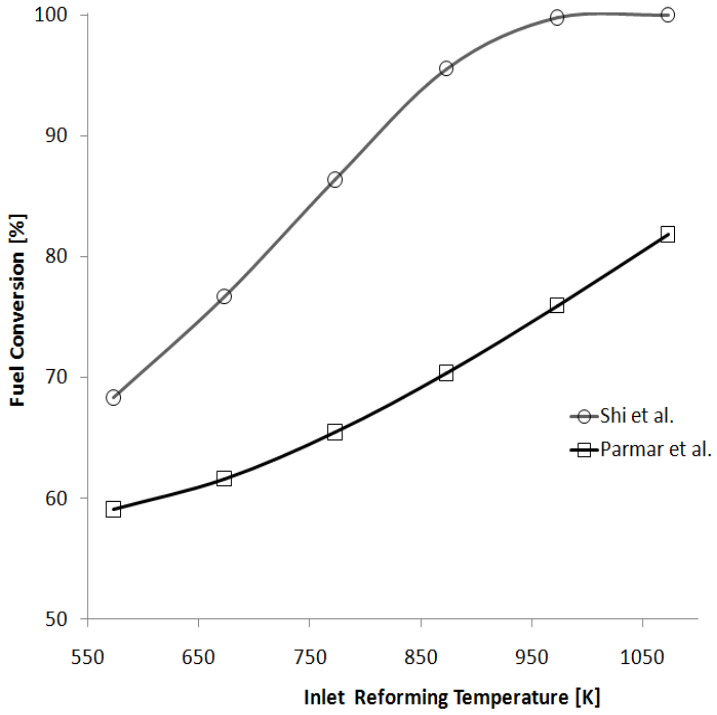

Figure 4.2-6: Influence of Inlet Reforming Temperature on Fuel Conversion

The differences in predicted fuel conversion between the kinetic models can be attributed to the differences in the support (Al_2O_3 vs CeO_2/Gd_2O_3) and the mechanisms used to derive the rate expressions. Both the Parmar *et al.* and Shi *et al.* kinetics were based on different rate determining steps for the reforming reaction. Parmar *et al.* considered C-C bond breakage to be rate-determining. Alternatively, Shi *et al.* based their simplified kinetic model on a model initially developed by Numaguchi and Kikuchi

[77] for the steam reforming of methane. The model developed by Numaguchi and Kikuchi assumed that the surface adsorption of methane was rate-determining.

Comparison of Effectiveness Factor Profiles

The design of catalysts with high effectiveness factors or low intra-phase mass transport resistances is critical in industry for reducing reactor volume and also the amount of catalyst used. Larger pellet sizes can be afforded for catalysts with low intra-phase mass transport resistances, thereby reducing pressure drop [78]. In this study, however, very fine catalyst particles are used and, therefore, only inter-phase resistance was taken into account. The effectiveness factors (4.2.3) were calculated for both kinetic models along the length of the CPR. The behavior of both the WGS reaction and the SR reactions were studied. The denominator in expression (4.2.3) represents the reaction rate at the surface of the catalyst layer. The subscript k refers to reactions (4.1.8) through (4.1.10).

$$\eta = \frac{\frac{1}{\delta_{cat}} \int_0^{\delta_{cat}} r_k \, dy}{r_k \,|_{y=\delta_{cat}}} \tag{4.2.3}$$

Parmar *et al.* considered two global reactions, including WGS and SR to CO and H_2, as is plotted in Figure 4.2-7 (a). The effectiveness factor for WGS was >1 at the entrance of the reforming channel. This was due to the fact that CO was not present at the inlet and, therefore, the reaction rate at the catalyst surface was lower than the average reaction rate over the catalyst layer thickness.

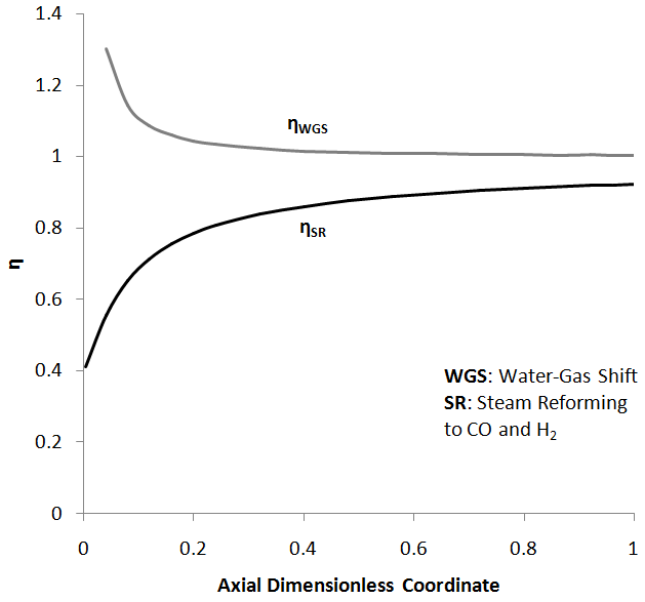

(a)

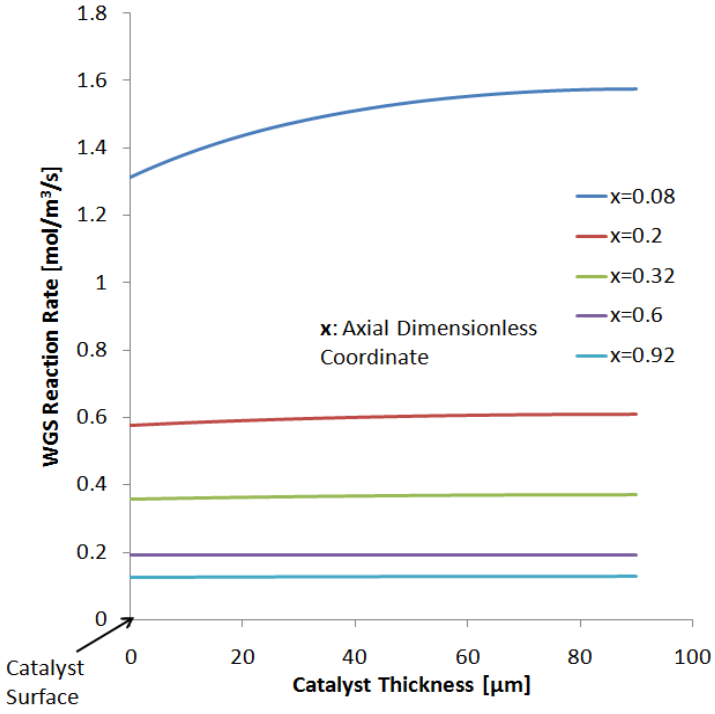

(b)

Figure 4.2-7: Effectiveness Factors and WGS Reaction Rate Profiles for Co-Current Flow Arrangement using Parmar *et al.'s* Kinetic Model: (a) η_{WGS} and η_{SR} (b) WGS Reaction Rate Across Catalyst Thickness

The effectiveness factor value approached one towards the end of the reactor as the reaction rate profiles across the catalyst thickness became more homogenized. These reaction rate profiles are seen in Figure 4.2-7 (b). The effectiveness factor of SR was lower near the entrance due to a lower hydrogen concentration. The reforming reaction rate was, therefore, faster at the catalyst surface. A maximum value of the effectiveness factor for SR of 0.92 was reached at the reactor exit.

The reverse WGS reaction was predicted to occur throughout the reactor for Shi *et al.'s* kinetic model (Figure 4.2-8 (a)). The WGS effectiveness factor remained positive until approximately 35% of the reactor length. In this initial region, the average reaction rate and the reaction rate at the surface of the catalyst layer were both negative. The reverse WGS was, in other words, predominant. The reaction rate at the surface of the catalyst layer began to increase as the effectiveness factor increased. The asymptotic effect at approximately 35% of the axial dimensionless coordinate was attributed to a shift in the direction of the WGS reaction at the catalyst surface from the reverse direction to the forward direction. Consequently, the effectiveness factor became negative as H_2 and CO_2 were produced from CO and H_2O at the surface. The change in the sign of the WGS reaction rate can also be seen in Figure 4.2-8 (b). The asymptotic effect is similar to the evolution of effectiveness factors for WGS as observed by Xu and Froment [79]. The global SR reactions producing either CO and H_2 or CO_2 and H_2 had almost identical effectiveness factors.

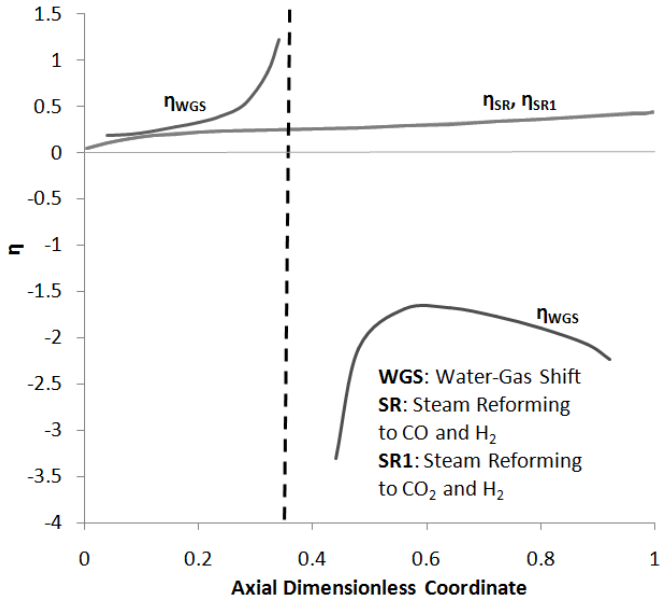

(a)

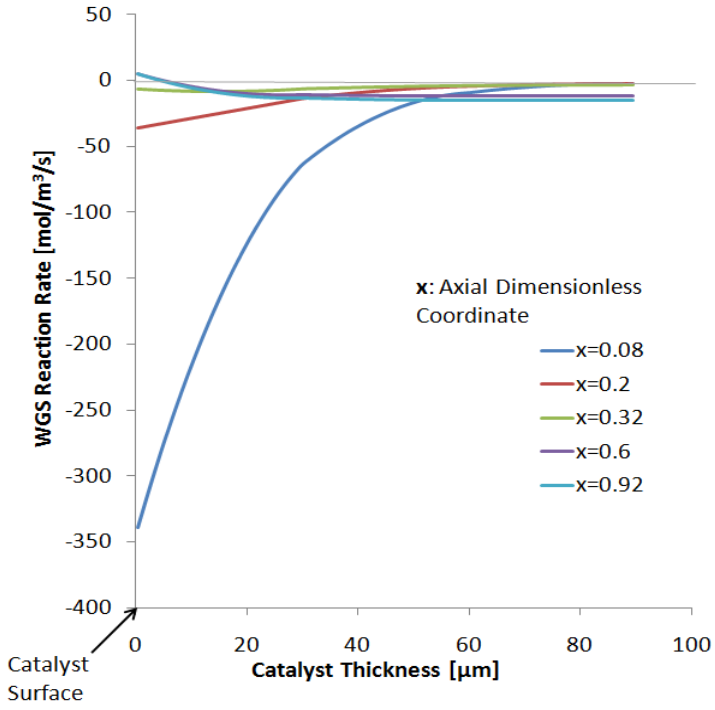

(b)

Figure 4.2-8: Effectiveness Factors and WGS Reaction Rate Profiles for Co-Current Flow Arrangement using Shi *et al's.* Kinetic Model: (a) η_{WGS}, η_{SR} and η_{SR1} (b) WGS Reaction Rate Across Catalyst Thickness

The reaction rate, however, was more pronounced for the reforming reaction producing CO_2 and H_2. For the Shi *et al.* model, a maximum effectiveness factor value of approximately 0.45 was observed at the reactor exit for both SR reactions.

4.3 Multi-Scale Modeling Integration; COMSOL-MATLAB-VMGSIM-EXCEL Interface

The design and optimization of the SOFC system requires a thorough understanding of the associated unit operations at various dimensional scales. The unit-operations for the SOFC system developed in this thesis, including the reformer and afterburner, were modeled based on an equilibrium approach for Gibbs free energy minimization and adiabatic conditions. The heat exchangers were based on the default shell and tube design in VMGSim™ and did not have the option of coupling reaction and heat exchange. This lack of an accurate representation and design flexibility of certain unit operations provided motivation for developing a multi-scale modeling approach.

A proof of concept, multi-scale modeling tool was developed that integrated the CFD software (COMSOL™) with the process modeling tool (VMGSim™), as is represented by the block diagram in Figure 4.3-1. The integration was achieved by using a Matlab™ Automation Server (AS) as the central communication interface of the set-up. The AS acts as a data storage box, from where information can be sent or retrieved. The arrows 1-8 in Figure 4.3-1 describe the flow of information. VMGSim™ contains an Excel™ Unit Operation (EUO) for performing external calculations. The EUO facilitates the import

and export of information by creating a live-link between a cell in the Excel™ worksheet and the property value in the VMGSim™ material stream.

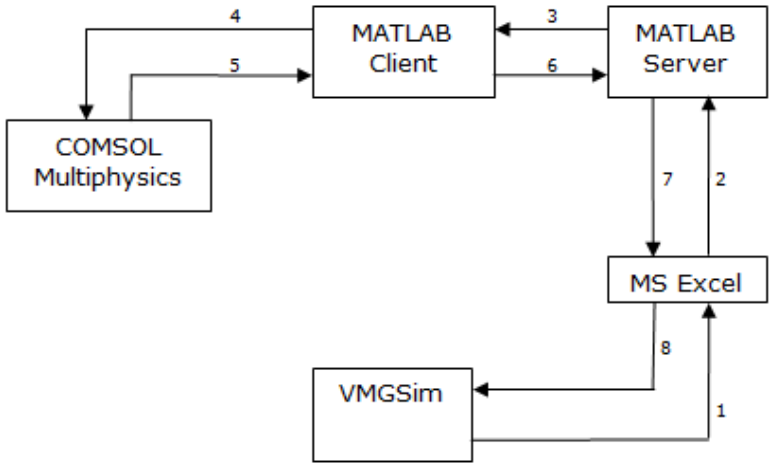

Figure 4.3-1: Block Diagram of Software Interactions

The proof of concept was developed in VMGSim™ for a stand-alone unit operation (the steam reforming heat-exchange reactor modeled in this chapter) involving four material streams (two inlet and two outlet).

- Firstly, any material stream property value changed by the user in VMGSim™ gets updated in the Excel™ worksheet via the live-link and is sent to the Matlab™ AS.
- The Matlab™ Client window runs a program that periodically searches for changes in property values of the input material streams to the heat-exchanger reactor, by retrieving the values from the Matlab™ AS.
- Once a change in an input material stream property value is detected, there is a small pause, after which the initialization of the CFD program for the heat-

exchanger reactor is triggered using the new input values. The property values at the output boundary of the reactor are averaged after the CFD simulation is complete and sent to the Matlab™ AS.

- The new output property values are finally exported back to the VMGSim™ environment, to the respective output material stream(s) of the heat-exchanger reactor.

Further documentation about setting up the multi-scale modeling tool proof of concept can be found in Appendix C.

Table 4.3-1 depicts the results for a sample run using the multi-scale modeling tool. The table portrays the inlet and outlet conditions in VMGSim™ before and after changing the inlet temperature in the reforming channel from 1073.15 K to 1000 K. The new solution in COMSOL™ using the updated initial conditions is computed and the average properties at the exit boundary of the reforming and flue gas channels (outlet conditions) are sent back to the VMGSim™ output material stream.

Table 4.3-1: Multi-Scale Tool Sample Run; Changing Inlet Conditions in VMGSim™

Inlet Conditions	***Before in VMGSim™***		***After in VMGSim™***	
	Reforming channel	**Flue Gas Channel**	**Reforming channel**	**Flue Gas Channel**
u	1 [m/s]	1 [m/s]	1 [m/s]	1 [m/s]
T	1073 [K]	1273 [K]	**1010 [K]**	1273 [K]
P	1 atm	1 atm	1 atm	1 atm
Outlet Conditions				
u	1.15 [m/s]	0.79 [m/s]	1.18 [m/s]	0.78 [m/s]
T	980 [K]	980 [K]	966 [K]	966 [K]
P	1 atm	1 atm	1 atm	1 atm

The integration of the heat-exchanger reactor into the process model has demonstrated the potential of this method for multi-scale modeling and optimization studies. Further integration of this tool will require modification to implement the CFD program into a process model with multiple unit operations and input-output streams, as well as for convergence during multiple solution iterations.

Chapter 5

Conclusion and Recommendations

5.1 Conclusion

A steady-state simulation of a small-scale diesel-fuelled SOFC system using a fuel processor with an ATR was developed for application in remote areas. A sensitivity analysis of key operating and design variables was carried out in order to investigate their influence on the net system efficiency, stack efficiency and the system exhaust temperature.

- The net and stack efficiencies were observed to be most sensitive to fuel and air utilization.
- The system exhaust temperature was most sensitive to the S to C ratio, because a greater heat of vaporization was required at higher ratios to generate steam; thus significantly reducing the exhaust temperature.
- A multi-variable study was carried out based on the sensitivity results, varying two independent variables at a time, in order to understand the behavior of the system. It was found that, at lower fuel utilizations, higher air utilization factors were not desirable. The limitation in the air utilization factor at low fuel utilizations was attributed to the significant increase in the stack temperature from additional fuel entering the burner as well as less excess air available for stack cooling.

- Maximum net system and stack efficiencies of 45% and 47%, respectively, were observed, at a high fuel utilization of 0.9. A minimum system exhaust temperature of 78 ^{o}C was achieved.

In the second part of this thesis, a steam-reforming heat-exchange reactor was modeled using COMSOL^{TM}. The model was for a catalytic plate reactor, with a diesel-steam mixture feed and a hot flue gas stream from the exhaust of the afterburner flowing in alternate channels. The hot flue gas served as a heat-source for the endothermic steam reforming reaction.

- Two experimentally validated kinetic models for diesel steam reforming, using tetradecane as a diesel surrogate were implemented and reactor performance was assessed on the basis of selectivity and residence time for a given conversion. Both kinetic models were based on a Pt catalyst, albeit with different supports. Shi *et al.*'s model [69] used a CeO_2/Gd_2O_3 support whereas Parmar *et al.*'s model [57] used an alumina support.
    - The exit fuel conversion using Shi *et al.'s* kinetic model, in comparison to Parmar *et al.*, was consistently greater for various inlet reforming temperatures and residence times.
    - The exit hydrogen yield for Shi *et al.* was also closer to the equilibrium values obtained from VMGSim^{TM}. The superior performance was attributed to the difference in the reaction mechanisms and the catalyst support.

- Parmar *et al.* did not consider the reforming of tetradecane to CO_2 as an independent global reaction and, therefore, a smaller concentration of CO_2 was observed at the reactor exit, than for Shi *et al.'s* kinetic model.
- The effectiveness factor profiles were calculated over the length of the reactor. The major difference in the profiles of the two kinetic models was the evolution of the WGS reaction.
    - The WGS effectiveness factor was greater than one near the channel entrance for Parmar *et al.'s* case, indicating that the bulk of the forward reaction was taking place within the catalyst layer. Near the exit of the channel, the value was close to one, such that the rate of reaction at the catalyst surface and inside the catalyst layer was approximately the same.
    - In the case of Shi *et al.*, the reverse WGS reaction producing CO and H_2O persisted throughout most of the reforming channel. The direction of the WGS reaction shifted from reverse to forward along the length of the reactor, as was reflected by the change in the sign of the effectiveness factor. The change in the sign of the effectiveness factor was attributed to the reaction rate at the catalyst surface changing from negative to positive. The behavior is similar to what has been reported by Xu and Froment [79].

Finally, a proof of concept multi-scale model integrating the CFD component model and the process simulation tool was developed. The multi-scale model involved a two-way interaction between four different software components: COMSOL™, VMGSim™, Matlab™ and Microsoft Excel™. This proof of concept approach was successfully demonstrated.

5.2 Recommendations and Future Work

The simulation of the diesel-fuelled SOFC system was carried out using hypothetical quantities for operating variables. The final simulation, therefore, needs to be validated against real system data. Similarly, the CFD models of the steam reforming heat-exchange reactor using tetradecane as the diesel surrogate would also need to be experimentally validated. Secondly, the system simulation was carried out at steady-state. A transient model would be required to evaluate system start-up and shut-down. The assessment of the steam reforming heat exchange reactor as an option to ATR for the system design was not possible and was due to work remaining for the completion of the multi-scale modeling tool. The proof of concept multi-scale model demonstrates the integration process for a stand-alone unit operation in VMGSim™. The concept, will, however, require some more adjustment (via discussion with VMGSim™ consultants) to allow for multiple input-output and unit operation interactions during convergence in the process simulation.

References

[1] B. Haughton, Hidden History: Lost Civilizations, Secret Knowledge, and Ancient Mysteries, The Career Press, New Jersey, 2006, ISBN: 1564148971.

[2] T.M. Letcher, Future energy: improved, sustainable and clean options for our planet, Elsevier, 2008, ISBN: 0080548083.

[3] V.S. Bagotsky Fuel cells: problems and solutions, John Wiley & Sons, New Jersey, 2009, ISBN: 0470232897.

[4] I. EG&G Technical Services, Fuel cell handbook, 7th ed., DOE, Morgantown, 2004, ISBN: 0899344283.

[5] N. Rajalakshmi, K. Dhathathreyan, Present Trends in Fuel Cell Technology Development, Nova Science Publishers Inc., 2008, ISBN: 1604562110.

[6] IEA, Prospects for hydrogen and fuel cells, OECD/IEA, 2005, ISBN: 9264109579.

[7] J.H. Clark, D.J. Macquarrie, Handbook of green chemistry and technology, Blackwell Science Ltd., 2002, ISBN: 0632057157.

[8] R. Bove, S. Ubertini, Modeling solid oxide fuel cells: methods, procedures and techniques, Springer 2008, ISBN: 1402069944.

[9] S.C. Singhal, K. Kendall, High temperature solid oxide fuel cells: fundamentals, design, and applications, Elsevier 2003, ISBN: 1856173879.

[10] V. Birss, (2007), NSERC Form 101 - Application for Grant, Retrieved September 2011 from http://www.sofccanada.com/membersonlysection/proposals.html.

[11] A.R. McKirdy, The Canadian Renewable Energy Guide, General Store Publishing House, Burnstown, 1999, ISBN: 1894263073.

[12] J.T. Pukrushpan, A.G. Stefanopoulou, H. Peng, Control of fuel cell power systems: principles, modeling, analysis, and feedback design, Springer London, 2004, ISBN: 1852338164.

[13] G. Kolb, Fuel processing: for fuel cells, Wiley-VCH, Weinheim, 2008, ISBN: 3527315810.

[14] D.P. Kothari, R. Ranjan, Renewable Energy Sources And Emerging Technologies, PHI Learning Private Limited, New Delhi, 2009, ISBN: 978-81-203-3357-4.

[15] N. Sammes, R. Boersma, Journal of Power Sources, 86 (2000) 98-110.

[16] J. Larminie, A. Dicks, Fuel cell systems explained, 2nd ed., John Wiley & Sons West Sussex, 2003, ISBN: 978-0-470-84857-9.

[17] E.D. Wachsman, C.A. Marlowe, K.T. Lee, Energy Environ. Sci., 5 (2012) 5498-5509.

[18] A. Hawkes, P. Aguiar, B. Croxford, M. Leach, C. Adjiman, N. Brandon, Journal of Power Sources, 164 (2007) 260-271.

[19] F.P. Sioshansi, Smart Grid: Integrating Renewable, Distributed & Efficient Energy, Academic Press, Waltham, 2011, ISBN: 0123864526.

[20] A. Hawkes, M. Leach, Journal of Power Sources, 149 (2005) 72-83.

[21] S. Basu, Recent trends in fuel cell science and technology, Springer New York, 2007, ISBN: 0387355375.

[22] L. J. Thijssen, (2011), Solid Oxide Fuel Cells and Critical Materials: A Review of Implications, Retrieved September 2011 from http://www.netl.doe.gov.

[23] M.C. Williams, J.P. Strakey, W.A. Surdoval, L.C. Wilson, Solid State Ionics, 177 (2006) 2039-2044.

[24] N.R. Council, C.o.A.a.S.f.F.H.P. Use, N.A.o. Engineering, The hydrogen economy: opportunities, costs, barriers, and R&D needs, National Academy Press, 2004, ISBN: 0309091632.

[25] S.D. Vora, ECS Trans., 35 (1), 3 (2011).

[26] K. Hosoi, M. Ito, M. Fukae, ECS Trans., 35 (1), 11 (2011).

[27] R. Steinberger-Wilckens, ECS Trans., 35 (1), 19 (2011).

[28] I. Canada, (2011), Hydrogen and Fuel Cells; Industry Canada, Retrieved September 2011 from http://www.ic.gc.ca/eic/site/hfc-hpc.nsf/eng/home.

[29] V. Birss, T. Petric, S. Thomas, (2011), SOFC Canada NSERC Strategic Research Network, Presented at ECS 219th Meeting, Montreal, ON, Retrieved from http://www.sofccanada.com/Documents/SOFC%20XII%20Network%20Talk.pdf.

[30] L.J.M.J. Blomen, M.N. Mugerwa, Fuel cell systems, Springer, New York, 1993, ISBN: 0306441586.

[31] J. Lawrence, M. Boltze, Journal of Power Sources, 154 (2006) 479-488.

[32] R.D. Parmar, A. Kundu, K. Karan, Journal of Power Sources, 194 (2009) 1007-1020.

[33] I. Kang, Y. Kang, S. Yoon, G. Bae, J. Bae, International Journal of Hydrogen Energy, 33 (2008) 6298-6307.

[34] Y. Yi, A.D. Rao, J. Brouwer, G.S. Samuelsen, Journal of Power Sources, 144 (2005) 67-76.

[35] G. Vourliotakis, G. Skevis, M. Founti, International Journal of Hydrogen Energy, 36 (2011) 6112-6122

[36] T.S. Lee, J. Chung, Y.C. Chen, Energy Conversion and Management, 52 (2011) 3214-3226.

[37] K. Kattke, R. Braun, Journal of Power Sources, 196 (2011) 6347-6355

[38] F. Baratto, U.M. Diwekar, D. Manca, Journal of Power Sources, 139 (2005) 205-213.

[39] L. J. Thijssen, (2004), The Impact of Future Diesel Fuel Specifications and Engine Emissions Standards on SOFC, Retrieved November 2011 from http://www.netl.doe.gov.

[40] J. Winterburn, (2009), Current specifications for anode feed in terms of contaminant levels, fuel quality and composition, Retrieved November 2011 from http://sofccanada.com.

[41] O. van Rheinberg, K. Lucka, H. Kohne, T. Schade, J.T. Andersson, Fuel, 87 (2008) 2988-2996.

[42] S. Hernández, L. Solarino, G. Orsello, N. Russo, D. Fino, G. Saracco, V. Specchia, International Journal of Hydrogen Energy, 33 (2008) 3209-3214.

[43] G. Alptekin, A. Jayaraman, M. Schaefer, ECS Trans., 35 (1), 2693 (2011).

[44] Z. Anxionnaz, M. Cabassud, C. Gourdon, P. Tochon, Chemical Engineering and Processing: Process Intensification, 47 (2008) 2029-2050.

[45] M. Zanfir, A. Gavriilidis, Chemical Engineering Science, 57 (2002) 1653-1659.

[46] M. Grote, M. Maximini, Z. Yang, P. Engelhardt, H. Kohne, K. Lucka, M. Brenner, Journal of Power Sources, (2010) 9027-9035.

[47] G. Kolb, J. Schürer, D. Tiemann, M. Wichert, R. Zapf, V. Hessel, H. Löwe, Journal of Power Sources, 171 (2007) 198-204.

[48] M. Zanfir, A. Gavriilidis, Chemical Engineering Science, 58 (2003) 3947-3960.

[49] M. Zanfir, A. Gavriilidis, Chemical Engineering Research and Design, 82 (2004) 252-258.

[50] K. Venkataraman, E. Wanat, L. Schmidt, AIChE Journal, 49 (2003) 1277-1284.

[51] J. Xu, G.F. Froment, AIChE Journal, 35 (1989) 88-96.

[52] P. Costamagna, A. Selimovic, M. Del Borghi, G. Agnew, Chemical Engineering Journal, 102 (2004) 61-69.

[53] J. Amphlett, R. Mann, B. Peppley, P. Roberge, A. Rodrigues, J. Salvador, Journal of Power Sources, 71 (1998) 179-184.

[54] M.T. Çoban, C. Ezgi, Journal of Naval Science and Engineering, 6 (2010) 59-78.

[55] R.K. Shah, D.P. Sekulić, K. . Fundamentals of heat exchanger design, John Wiley & Sons, New Jersey, 2003, ISBN: 0471321710.

[56] J.J. Spivey, Fuel Cells: Technologies for Fuel Processing, Elsevier 2011, ISBN: 0444535632.

[57] R.D. Parmar, A. Kundu, C. Thurgood, B.A. Peppley, K. Karan, Fuel, 89 (2010) 1212-1220.

[58] G. Wang, Y. Yang, H. Zhang, W. Xia, Journal of Power Sources, 167 (2007) 398-405.

[59] D. Hamby, Health Physics, 68 (1995) 195-204.

[60] D. Hamby, Environmental Monitoring and Assessment, 32 (1994) 135-154.

[61] S. Shaffer, (2007), Development Update on Delphi's Solid Oxide Fuel Cell Systems, Presented at 2007 SECA Annual Review Meeting, Retrieved from http://www.netl.doe.gov/publications/proceedings/07/SECA_Workshop/.

[62] C. Fauteux-Lefebvre, N. Abatzoglou, N. Braidy, I.E. Achouri, Journal of Power Sources, 196 (2011) 7673-7680

[63] W.A. Whittenberger, (2010), Permanent, High Performance, Drop-In Replacement Catalyst for Steam Reforming Hydrogen Plants, Retrieved October 2011 from http://www.catacel.com/resources.php.

[64] W.A. Whittenberger, (2007), Patent No. WO/2007/032891, Garretsville, OH: World Intellectual Property Organization.

[65] R.B. Bird, W.E. Stewart, E.N. Lightfoot, Transport Phenomena, JohnWiley & Sons, New York, 2002, ISBN.

[66] L.A. Belfiore, J.J. Way, L. Zhang, Transport phenomena for chemical reactor design, John Wiley & Sons, 2003, ISBN: 0-471-20275-4.

[67] C.L. Yaws, C. Gabbula, Yaws" Handbook of Thermodynamic and Physical Properties of Chemical Compounds, Knovel, 2003, ISBN: 1591244447.

[68] B.E. Poling, J.M. Prausnitz, P.O.C. John, The properties of gases and liquids, 5th ed., McGraw-Hill New York, 2001, ISBN: 0-07-149999-7.

[69] L. Shi, D.J. Bayless, M.E. Prudich, International Journal of Hydrogen Energy, 34 (2009) 7666-7675.

[70] Matweb, Resistalloy International Fecralloy™ 135 Electrical Resistance Steel, Retrieved October 2011 from http://www.matweb.com/search/datasheet.aspx?matguid=936326174f534ec78ba8eb373a2d9953&ckck=1.

[71] A.K. AvcI, D.L. Trimm, M. Karakaya, Catalysis Today, 155 (2010) 66-74.

[72] M.E. Davis, R.J. Davis, Fundamentals of chemical reaction engineering, McGraw-Hill Higher Education, 2003, ISBN: 007245007X.

[73] R.H. Perry, D. Green, Perry's Chemical Engineers' Handbook, 7th ed., McGraw-hill, 1997, ISBN: 0-07-049841-5.

[74] P.V. Gawade, D. Patel, G.G. Lipscomb, M.A. Abraham, Industrial & Engineering Chemistry Research, 49 (2010) 6931–6940.

[75] J. Thormann, L. Maier, P. Pfeifer, U. Kunz, O. Deutschmann, K. Schubert, International Journal of Hydrogen Energy, 34 (2009) 5108-5120.

[76] D. Creaser, X. Karatzas, B. Lundberg, L.J. Pettersson, J. Dawody, Applied Catalysis A: General, (2011).

[77] T. Numaguchi, K. Kikuchi, Chemical engineering science, 43 (1988) 2295-2301.

[78] A. Kronberg, K. Westerterp, Industrial catalysis: optimizing catalysts and processes, Vch Verlagsgesellschaft Mbh, 1998, ISBN: 3527285814.

[79] J. Xu, G.F. Froment, AIChE Journal, 35 (1989) 97-103.

[80] C.L. Yaws, Chemical properties handbook, Knovel Corporation, 1999, ISBN: 159124028X.

Appendix A

Baseline Process Simulation Stream Tables

Please refer to Figure 3.1-1 for stream names.

Table A-1: Stream Tables for Baseline Conditions in SOFC Model

Stream Name	/a1	/a3	/ab1	/ab2	/ab3	Air In	/airtor	/anodein	Anode Exhaust
VapFrac	1	1	1	1	1	1	1	1	1
T [C]	36	36	557	483	472	20	36	590	863
P [kPa]	107	107	105	104	104	101	107	105	105
Mole Flow [kgmole/h]	0.28	0.26	0.34	0.34	0.34	0.28	0.02	0.09	0.09
Fraction [Fraction]									
HYDROGEN	0	0	0	0	0	0	0	0.32	0.06
CARBON MONOXIDE	0	0	0	0	0	0	0	0.04	0.02
CARBON DIOXIDE	0	0	0.05	0.05	0.05	0	0	0.12	0.15
WATER	0	0	0.19	0.19	0.19	0	0	0.34	0.6
OXYGEN	0.21	0.21	0.11	0.11	0.11	0.21	0.21	0	0
NITROGEN	0.79	0.79	0.66	0.66	0.66	0.79	0.79	0.17	0.17
METHANE	0	0	0	0	0	0	0	0.01	0.01
HYDROGEN SULFIDE	0	0	0	0	0	0	0	0	0
n-NONANE	0	0	0	0	0	0	0	0	0
n-DECANE	0	0	0	0	0	0	0	0	0
n-UNDECANE	0	0	0	0	0	0	0	0	0
n-DODECANE	0	0	0	0	0	0	0	0	0
n-TRIDECANE	0	0	0	0	0	0	0	0	0
n-TETRADECANE	0	0	0	0	0	0	0	0	0
n-PENTADECANE	0	0	0	0	0	0	0	0	0

n-HEXADECANE	0	0	0	0	0	0	0	0	0
n-HEPTADECANE	0	0	0	0	0	0	0	0	0
n-OCTADECANE	0	0	0	0	0	0	0	0	0
n-NONADECANE	0	0	0	0	0	0	0	0	0
n-EICOSANE	0	0	0	0	0	0	0	0	0
n-PENTYLBENZENE	0	0	0	0	0	0	0	0	0
n-HEXYLBENZENE	0	0	0	0	0	0	0	0	0
n-HEPTYLBENZENE	0	0	0	0	0	0	0	0	0
n-OCTYLBENZENE	0	0	0	0	0	0	0	0	0
n-NONYLBENZENE	0	0	0	0	0	0	0	0	0
n-DECYLBENZENE	0	0	0	0	0	0	0	0	0
n-UNDECYLBENZENE	0	0	0	0	0	0	0	0	0
n-DODECYLBENZENE	0	0	0	0	0	0	0	0	0
NAPHTHALENE	0	0	0	0	0	0	0	0	0
1-METHYLNAPHTHALENE	0	0	0	0	0	0	0	0	0
1-ETHYLNAPHTHALENE	0	0	0	0	0	0	0	0	0
1-PROPYLNAPHTHALENE	0	0	0	0	0	0	0	0	0
1-n-BUTYLNAPHTHALENE	0	0	0	0	0	0	0	0	0
PHENYL MERCAPTAN	0	0	0	0	0	0	0	0	0
ETHANE	0	0	0	0	0	0	0	0	0
PROPANE	0	0	0	0	0	0	0	0	0
n-BUTANE	0	0	0	0	0	0	0	0	0
n-PENTANE	0	0	0	0	0	0	0	0	0
n-HEXANE	0	0	0	0	0	0	0	0	0
n-HEPTANE	0	0	0	0	0	0	0	0	0
n-OCTANE	0	0	0	0	0	0	0	0	0
Mass Flow [kg/h]	8.1	7.54	9.22	9.22	9.22	8.1	0.57	1.69	2.13
Std Gas Volume Flow [SCMD]	1.60E+02	1.49E+02	1.92E+02	1.92E+02	1.92E+02	1.60E+02	1.12E+01	5.32E+01	5.32E+01
Std Liq Volume Flow [m3/hr]	0.024	0.022	0.024	0.024	0.024	0.024	0.002	0.005	0.004

Energy [W]	7.02E+02	6.53E+02	2.45E+03	2.21E+03	2.17E+03	6.65E+02	4.92E+01	7.36E+02	1.08E+03
H [kJ/kmol]	9003.3	9003.3	26061.4	23542.4	23170.7	8526.8	9003.3	28308	41357
S [kJ/kmol-K]	171.691	171.691	210.827	207.69	207.235	170.593	171.691	214.653	236.243
MW	28.85	28.85	27.31	27.31	27.31	28.85	28.85	18.02	22.7
Cp [kJ/kmol-K]	29.253	29.253	34.229	33.627	33.537	29.213	29.253	36.658	42.935
Thermal Conductivity [W/m-K]	0.0258	0.0258	0.0623	0.0569	0.0561	0.0247	0.0258	0.1341	0.1134
Viscosity [Pa-s]	1.86E-05	1.86E-05	3.66E-05	3.41E-05	3.37E-05	1.79E-05	1.86E-05	3.46E-05	4.39E-05
Z Factor	0.9998	0.9998	1.0003	1.0003	1.0003	0.9996	0.9998	1.0002	1.0001

Stream Name	**/anodetoab**	**/cathodein**	**Cathode Exhaust**	**/cathodetoab**	**System Exhaust**	**/f1**	**/f2**	**/f3**	**/f7**
VapFrac	1	1	1	1	1	0	0	0	1
T [C]	841	800	864	63	213	20	200	200	320
P [kPa]	105	105	105	105	103	118	117	117	117
Mole Flow [kgmole/h]	0.09	0.26	0.25	0.25	0.34	0	0	0	0
Fraction [Fraction]									
HYDROGEN	0.06	0	0	0	0	0	0	0	0
CARBON MONOXIDE	0.02	0	0	0	0	0	0	0	0
CARBON DIOXIDE	0.15	0	0	0	0.05	0	0	0	0
WATER	0.6	0	0	0	0.19	0	0	0	0
OXYGEN	0	0.21	0.17	0.17	0.11	0	0	0	0
NITROGEN	0.17	0.79	0.83	0.83	0.66	0	0	0	0
METHANE	0.01	0	0	0	0	0	0	0	0
HYDROGEN SULFIDE	0	0	0	0	0	0	0	0	0
n-NONANE	0	0	0	0	0	0.02	0.02	0.02	0.02
n-DECANE	0	0	0	0	0	0.01	0.01	0.01	0.01
n-UNDECANE	0	0	0	0	0	0	0	0	0
n-DODECANE	0	0	0	0	0	0	0	0	0

n-TRIDECANE	0	0	0	0	0	0	0	0	0
n-TETRADECANE	0	0	0	0	0	0	0	0	0
n-PENTADECANE	0	0	0	0	0	0	0	0	0
n-HEXADECANE	0	0	0	0	0	0.01	0.01	0.01	0.01
n-HEPTADECANE	0	0	0	0	0	0.01	0.01	0.02	0.02
n-OCTADECANE	0	0	0	0	0	0.03	0.03	0.03	0.03
n-NONADECANE	0	0	0	0	0	0.07	0.07	0.07	0.07
n-EICOSANE	0	0	0	0	0	0.14	0.14	0.14	0.14
n-PENTYLBENZENE	0	0	0	0	0	0.08	0.08	0.08	0.08
n-HEXYLBENZENE	0	0	0	0	0	0.06	0.06	0.06	0.06
n-HEPTYLBENZENE	0	0	0	0	0	0.05	0.05	0.05	0.05
n-OCTYLBENZENE	0	0	0	0	0	0.05	0.05	0.05	0.05
n-NONYLBENZENE	0	0	0	0	0	0.05	0.05	0.05	0.05
n-DECYLBENZENE	0	0	0	0	0	0.05	0.05	0.05	0.05
n-UNDECYLBENZENE	0	0	0	0	0	0.12	0.12	0.12	0.12
n-DODECYLBENZENE	0	0	0	0	0	0.19	0.19	0.19	0.19
NAPHTHALENE	0	0	0	0	0	0.01	0.01	0.01	0.01
1-METHYLNAPHTHALENE	0	0	0	0	0	0	0	0	0
1-ETHYLNAPHTHALENE	0	0	0	0	0	0.01	0.01	0.01	0.01
1-PROPYLNAPHTHALENE	0	0	0	0	0	0.01	0.01	0.01	0.01
1-n-BUTYLNAPHTHALENE	0	0	0	0	0	0.01	0.01	0.01	0.01
PHENYL MERCAPTAN	0	0	0	0	0	0.01	0.01	0	0
ETHANE	0	0	0	0	0	0	0	0	0
PROPANE	0	0	0	0	0	0	0	0	0
n-BUTANE	0	0	0	0	0	0	0	0	0
n-PENTANE	0	0	0	0	0	0	0	0	0
n-HEXANE	0	0	0	0	0	0	0	0	0
n-HEPTANE	0	0	0	0	0	0	0	0	0
n-OCTANE	0	0	0	0	0	0	0	0	0

Mass Flow [kg/h]	2.13	7.54	7.1	7.1	9.22	0.23	0.23	0.23	0.23
Std Gas Volume Flow [SCMD]	5.32E+01	1.49E+02	1.41E+02	1.41E+02	1.92E+02	5.87E-01	5.87E-01	5.79E-01	5.79E-01
Std Liq Volume Flow [m3/hr]	0.004	0.022	0.021	0.021	0.024	0	0	0	0
Energy [W]	1.05E+03	2.38E+03	2.40E+03	6.72E+02	1.38E+03	-5.68	2.03E+01	2.03E+01	5.51E+01
H [kJ/kmol]	40359.5	32848.4	34934.2	9767.9	14734.3	-19827	70715.5	71611.1	194892.1
S [kJ/kmol-K]	235.397	210.12	211.49	173.772	193.391	517.183	755.096	763.407	988.379
MW	22.7	28.85	28.68	28.68	27.31	219.64	219.64	221.06	221.06
Cp [kJ/kmol-K]	42.684	33.511	33.75	29.295	31.538	419.926	572.475	577.22	573.726
Thermal Conductivity [W/m-K]	0.1108	0.0732	0.0763	0.0276	0.0369	0.1324	0.1021	0.1021	0.0232
Viscosity [Pa-s]	4.32E-05	4.55E-05	4.69E-05	1.96E-05	2.39E-05	3.66E-03	3.77E-04	3.78E-04	8.59E-06
Z Factor	1.0001	1.0003	1.0003	1	1	0.0125	0.0089	0.009	0.9283

Stream Name	**Fuel In**	**/mixtoab**	**/sulfurrem**	**/w1**	**/w3**	**/wa1**	**/waf1**	**Water In**	**/wf5**
VapFrac	0	1	1	0	1	1	1	0	1
T [C]	20	323	200	20	300	234	250	20	527
P [kPa]	101	105	117	118	117	107	107	101	105
Mole Flow [kgmole/h]	0	0.34	0	0.05	0.05	0.07	0.07	0.05	0.07
Fraction [Fraction]									
HYDROGEN	0	0.02	0	0	0	0	0	0	0
CARBON MONOXIDE	0	0	0	0	0	0	0	0	0
CARBON DIOXIDE	0	0.04	0	0	0	0	0	0	0
WATER	0	0.17	0	1	1	0.72	0.71	1	0.71
OXYGEN	0	0.12	0	0	0	0.06	0.06	0	0.06
NITROGEN	0	0.65	0	0	0	0.22	0.22	0	0.22

METHANE	0	0	0	0	0	0	0	0	0
HYDROGEN SULFIDE	0	0	0	0	0	0	0	0	0
n-NONANE	0.02	0	0	0	0	0	0	0	0
n-DECANE	0.01	0	0	0	0	0	0	0	0
n-UNDECANE	0	0	0	0	0	0	0	0	0
n-DODECANE	0	0	0	0	0	0	0	0	0
n-TRIDECANE	0	0	0	0	0	0	0	0	0
n-TETRADECANE	0	0	0	0	0	0	0	0	0
n-PENTADECANE	0	0	0	0	0	0	0	0	0
n-HEXADECANE	0.01	0	0	0	0	0	0	0	0
n-HEPTADECANE	0.01	0	0	0	0	0	0	0	0
n-OCTADECANE	0.03	0	0	0	0	0	0	0	0
n-NONADECANE	0.07	0	0	0	0	0	0	0	0
n-EICOSANE	0.14	0	0	0	0	0	0	0	0
n-PENTYLBENZENE	0.08	0	0	0	0	0	0	0	0
n-HEXYLBENZENE	0.06	0	0	0	0	0	0	0	0
n-HEPTYLBENZENE	0.05	0	0	0	0	0	0	0	0
n-OCTYLBENZENE	0.05	0	0	0	0	0	0	0	0
n-NONYLBENZENE	0.05	0	0	0	0	0	0	0	0
n-DECYLBENZENE	0.05	0	0	0	0	0	0	0	0
n-UNDECYLBENZENE	0.12	0	0	0	0	0	0	0	0
n-DODECYLBENZENE	0.19	0	0	0	0	0	0	0	0
NAPHTHALENE	0.01	0	0	0	0	0	0	0	0
1-METHYLNAPHTHALENE	0	0	0	0	0	0	0	0	0
1-ETHYLNAPHTHALENE	0.01	0	0	0	0	0	0	0	0
1-PROPYLNAPHTHALENE	0.01	0	0	0	0	0	0	0	0
1-n-BUTYLNAPHTHALENE	0.01	0	0	0	0	0	0	0	0
PHENYL MERCAPTAN	0.01	0	1	0	0	0	0	0	0

ETHANE	0	0	0	0	0	0	0	0	0
PROPANE	0	0	0	0	0	0	0	0	0
n-BUTANE	0	0	0	0	0	0	0	0	0
n-PENTANE	0	0	0	0	0	0	0	0	0
n-HEXANE	0	0	0	0	0	0	0	0	0
n-HEPTANE	0	0	0	0	0	0	0	0	0
n-OCTANE	0	0	0	0	0	0	0	0	0
Mass Flow [kg/h]	0.23	9.22	0	0.89	0.89	1.46	1.69	0.89	1.69
Std Gas Volume Flow [SCMD]	5.87E-01	1.94E+02	7.51E-03	2.82E+01	2.82E+01	3.94E+01	4.00E+01	2.82E+01	4.00E+01
Std Liq Volume Flow [m3/hr]	0	0.025	0	0.001	0.001	0.003	0.003	0.001	0.003
Energy [W]	-5.69E+00	1.72E+03	1.43E-01	-5.23E+02	2.68E+02	3.17E+02	3.72E+02	-5.23E+02	6.09E+02
H [kJ/kmol]	-19841	18165.4	39079.5	-37973.8	19441	16475.8	19059.3	-37974.7	31154.3
S [kJ/kmol-K]	517.15	199.856	151.26	60.129	212.11	207.161	219.184	60.126	237.808
MW	219.64	27.04	110.18	18.02	18.02	21.09	23.99	18.02	23.99
Cp [kJ/kmol-K]	419.911	32.147	158.159	94.895	36.15	33.893	41.064	94.895	46.166
Thermal Conductivity [W/m-K]	0.1324	0.0475	0.0211	0.5985	0.0437	0.0375	0.0378	0.5985	0.0656
Viscosity [Pa-s]	3.67E-03	2.84E-05	1.09E-05	1.00E-03	2.03E-05	2.04E-05	2.00E-05	1.00E-03	3.06E-05
Z Factor	0.0108	1.0002	0.9686	0.0009	0.9974	0.9986	0.9984	0.0008	0.9998

Appendix B

Mass, Momentum and Heat Transport

This section includes the relevant properties expressions applied in the development of the component model discussed in Chapter 4. Relevant property expressions are provided for gas densities, heat capacities, thermal conductivities, mass transfer or diffusion coefficients and dynamic viscosities. Effective properties and single species properties are listed.

Mixture Molecular Weight

$$M_{mix} = \sum M_i \, c_i / \sum c_i \quad \text{(C.1.1)}$$

Mixture Density

$$\rho_{mix} = P M_{mix} / RT \quad \text{(C.1.2)}$$

Catalyst Layer Density

$$\rho_{eff} = \rho_s (1 - \phi) \quad \text{(C.1.3)}$$

Species Weight Fraction

$$wt_i = c_i M_i / M_{mix} \sum c_i \quad \text{(C.1.4)}$$

Thermal Conductivity as a Function of Temperature and Pressure [67, 80] [W/m.K]

$$k_{H2O} = 5.3\text{E-}04 + \left(4.7093\text{E-}05\right)T + \left(4.9551\text{E-}08\right)T^2 \quad \text{(C.1.5)}$$

$$k_{CO2} = -1.2\text{E-}02 + (1.0208\text{E-}04)T - \left(2.2403\text{E-}08\right)T^2 \quad \text{(C.1.6)}$$

$$k_{CO} = 1.58\text{E-}03 + (8.2511\text{E-}05)T - (1.9081\text{E-}08)T^2 \quad \text{(C.1.7)}$$

$$k_{H2} = 3.951\text{E-}02 + (4.5918\text{E-}04)T - (6.4933\text{E-}08)T^2 \quad \text{(C.1.8)}$$

$$k_{O2} = 1.21\text{E-}03 + (8.6157\text{E-}05)T - (1.3346\text{E-}08)T^2 \quad \text{(C.1.9)}$$

$$k_{N2} = 3.09\text{E-}03 + (7.593\text{E-}05)T - (1.1014\text{E-}08)T^2 \quad \text{(C.1.10)}$$

$$k_{C14} = -1.8\text{E-}03 + (1.0242\text{E-}05)T + (7.7727\text{E-}08)T^2 \quad \text{(C.1.11)}$$

One approximation for the conductivity of gaseous mixtures is the Wassiljewa equation [68] at low pressures conditions.

$$k_{mix} = \sum_{i=1}^{n} \frac{X_i k_i}{\sum_{j=1}^{n} X_i A_{ij}} \quad \text{(C.1.12)}$$

$$A_{ij} = \frac{\left[1 + \left(\mu_i / \mu_j\right)^{0.5} \left(M_j / M_i\right)^{0.25}\right]^2}{\left[8\left(1 + \left(M_i / M_j\right)\right)\right]^{0.5}} \quad \text{(C.1.13)}$$

$$A_{ji} = A_{ij} \frac{\mu_j}{\mu_i} \frac{M_i}{M_j} \quad \text{(C.1.14)}$$

where A_{ii} or $A_{jj} = 1$.

Heat Capacity as a Function of Temperature and Pressure [67, 80] [J/mol/K]

$$C_{pH2O} = 33.933 - (8.4186\text{E-}03)T + (2.9906\text{E-}05)T^2 - (1.7825\text{E-}08)T^3 + (3.6934\text{E-}12)T^4 \quad \text{(C.1.15)}$$

$$C_{pCO2} = 27.437 + (4.2315\text{E-}02)T - (1.9555\text{E-}05)T^2 + (3.9968\text{E-}09)T^3 - (2.9872\text{E-}13)T^4 \quad \text{(C.1.16)}$$

$$C_{pCO} = (29.556 - (6.5807\text{E-}03)T + (2.013\text{E-}05)T^2 - (1.2227\text{E-}08)T^3 + (2.2617\text{E-}12)T^4 \quad \text{(C.1.17)}$$

$$C_{pH2} = (25.399 + (2.0178\text{E-}02)T - (3.8549\text{E-}05)T^2 + (3.188\text{E-}08)T^3 - (8.7585\text{E-}12)T^4 \quad \text{(C.1.18)}$$

$$C_{pO2} = (29.526 - (8.8999\text{E-}03)T + (3.8083\text{E-}05)T^2 - (3.2629\text{E-}08)T^3 + (8.8607\text{E-}12)T^4 \quad \text{(C.1.19)}$$

$$C_{pN2} = (29.342 - (3.5395\text{E-}03)T + (1.0076\text{E-}05)T^2 - (4.3116\text{E-}09)T^3 + (2.5935\text{E-}13)T^4 \quad \text{(C.1.20)}$$

$$C_{pC14} = (115.50 + (0.60882)T + (6.8043\text{E-}04)T^2 - (9.709\text{E-}07)T^3 + (3.0756\text{E-}09)T^4 \quad \text{(C.1.21)}$$

The heat capacity of the mixture in [J/kg.K] is calculated based on component weight fractions.

$$C_{pMIX} = \sum wt_{fr,i}\left(C_{pi}/M_i\right) \quad \text{(C.1.22)}$$

Dynamic Viscosity as a Function of Temperature and Pressure [67, 80] [microPoise]

$$\mu_{H2O} = -36.826 + (0.429)T - (1.62\text{E-}05)T^2 \quad \text{(C.1.23)}$$

$$\mu_{CO2} = 11.811 + (0.49838)T - (1.0851\text{E-}04)T^2 \quad \text{(C.1.24)}$$

$$\mu_{CO} = 23.811 + (0.53944)T - (1.5411\text{E-}04)T^2 \quad \text{(C.1.25)}$$

$$\mu_{H2} = 27.758 + (0.212)T - (3.28\text{E-}05)T^2 \quad \text{(C.1.26)}$$

$$\mu_{O2} = 44.224 + (0.562)T - (1.13\text{E-}04)T^2 \quad \text{(C.1.27)}$$

$$\mu_{N2} = 42.606 + (0.475)T - (9.88\text{E-}05)T^2 \quad \text{(C.1.28)}$$

$$\mu_{C14} = -10.397 + (0.157)T + (1.0229\text{E-}06)T^2 \quad \text{(C.1.29)}$$

The mixture viscosity at low pressure can be evaluated using the expression by Herning and Zipperer *[68]*.

$$\mu_{mix} = \frac{\sum \mu_i X_i M_i^{0.5}}{X_i M_i^{0.5}} \quad \text{(C.1.30)}$$

Figure B-1 portrays the velocity profile in the reforming channel plus catalyst layer along the reactor length (for an average inlet velocity of 0.3 m/s). The velocity is zero at the channel wall (no-slip condition). There is a noticeable increase in velocity of the fluid from the catalyst layer pore network to the reforming channel. There is no change in velocity at the centerline of the channel as per the symmetry condition and, therefore, a zero momentum flux.

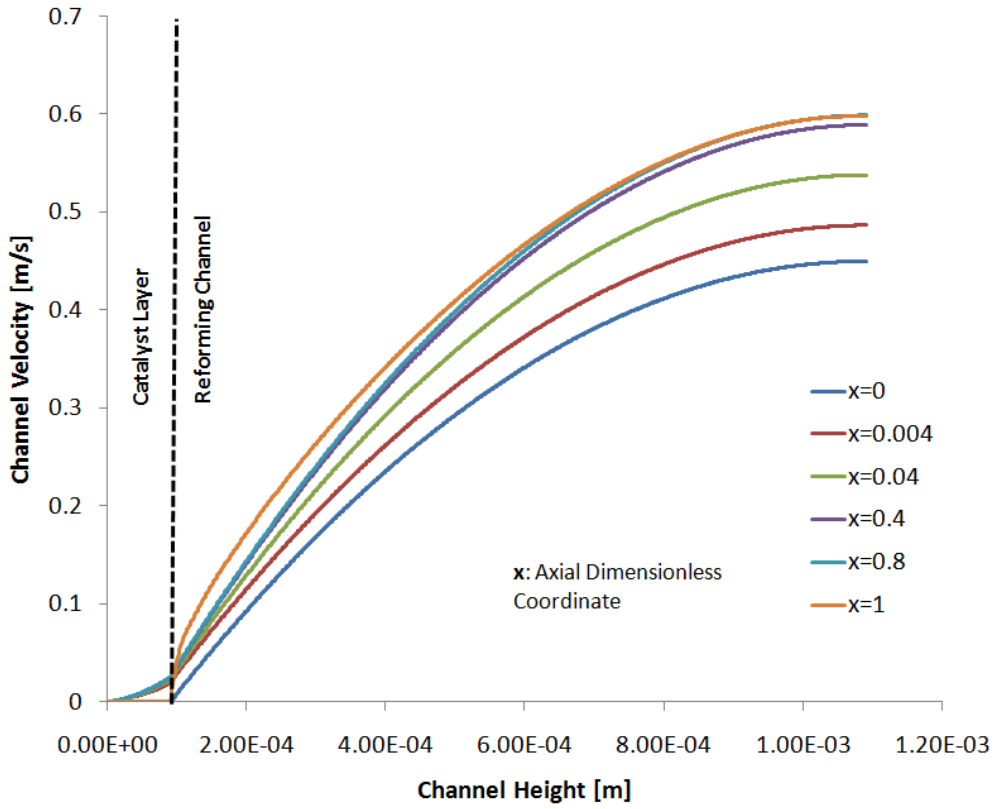

Figure B-1: Velocity Profile in Reforming Channel and Catalyst at different Axial Positions along the Reactor Length

A section of the original mesh (unstructured grid) used for the CFD computations in COMSOL Multiphysics™ (consisting of 40,051 triangular mesh elements) can be seen in Figure B-2. More mesh elements were added near the entrance of the reforming channel where momentum, mass and heat transfer gradients were more significant. Figures B-3 and B-4 show sample temperature and velocity profiles in the reactor sub-domains for the initial conditions described in Table 4.1-2.

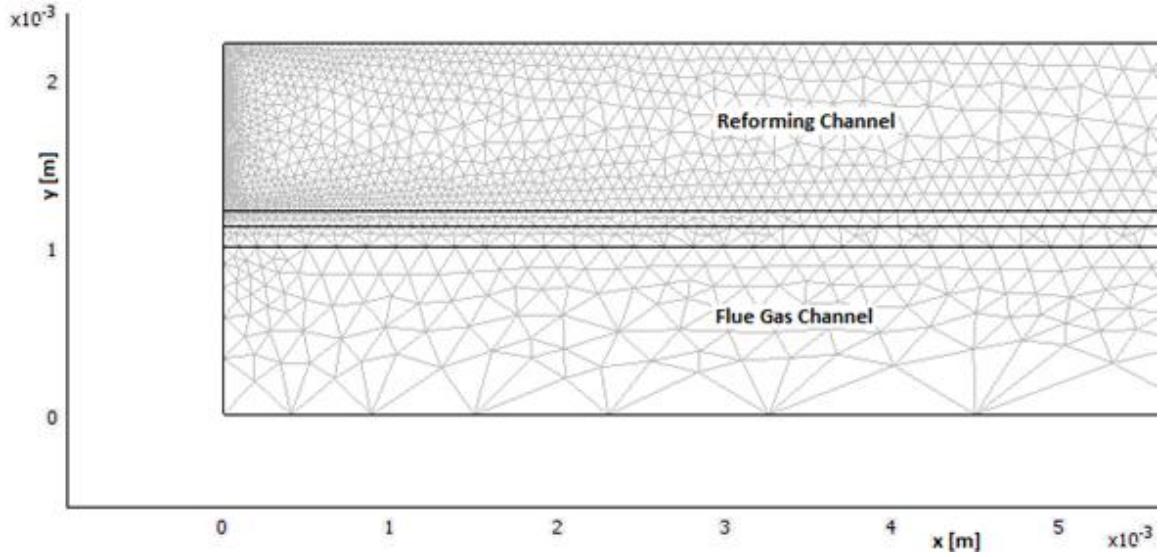

Figure B-2: Diagram of Mesh (from COMSOL Multiphysics™) used in Simulation of CPR

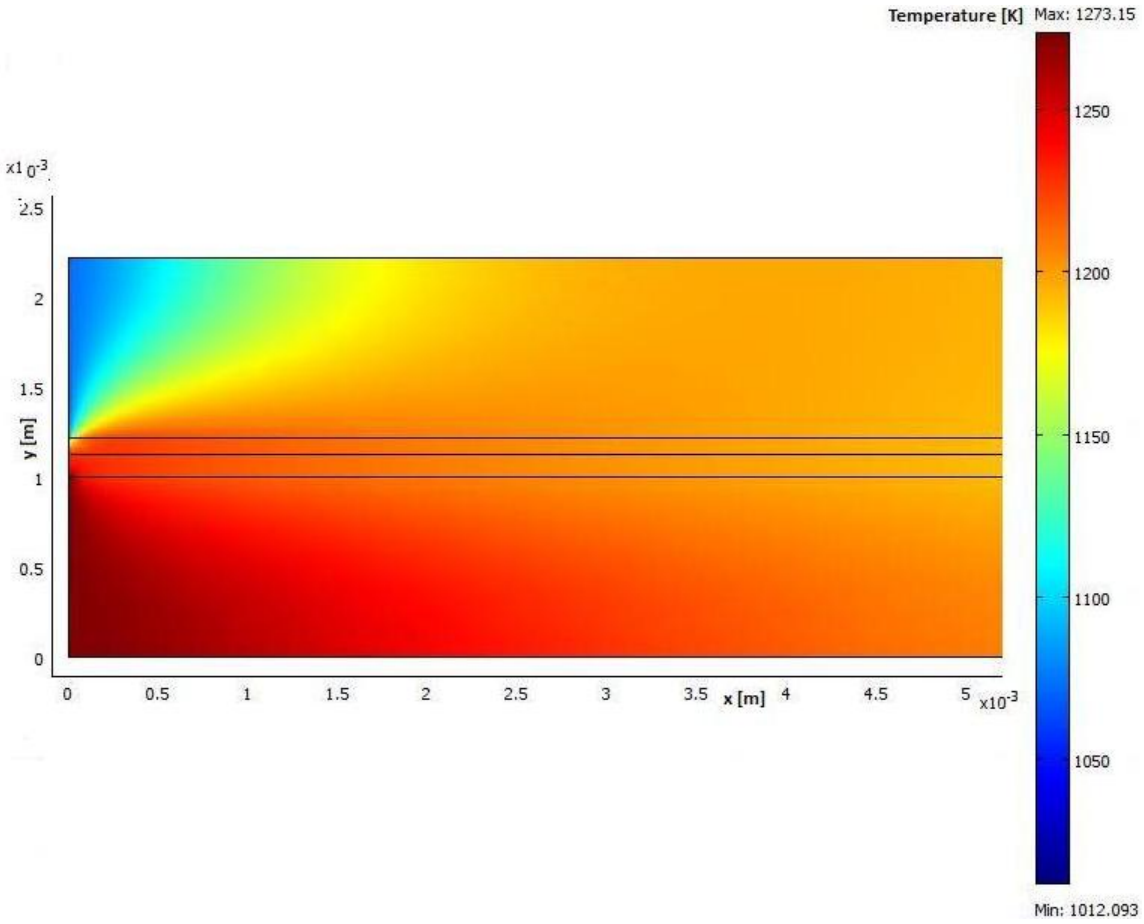

Figure B-3: CPR Temperature Map

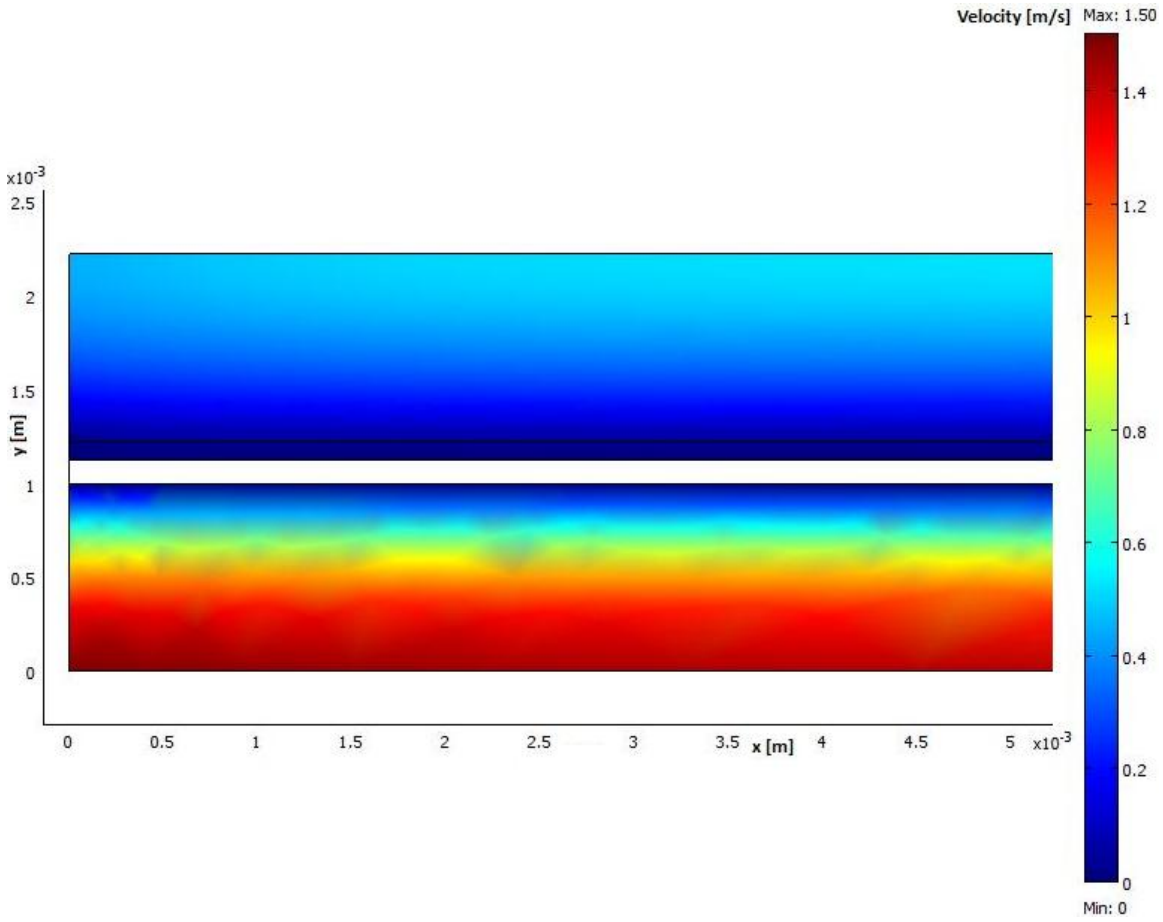

Figure B-4: CPR Velocity Map

Appendix C

Multi-Scale Modeling Tool Documentation

Setting up the Interface

- Install Matlab™ 2009a/b or higher with Spreadsheet Link EX toolbox.
- Install COMSOL™ 3.5a or higher with Matlab™ option. Specify the Matlab™ path if it is not automatically detected. Ensure that Office 97 or later installed on your system.
- Install VMGSim™ 6.0 and Microsoft Visual Studio Professional™ (2002, 2003 or 2007).
- Open Excel™ and click the Office button. Go to *Excel Options → Add Ins* and check Spreadsheet Link EX for use with MATLAB™. This creates an interface to communicate with Matlab™ from within Excel™. Close the Excel™ application.
- Run or double-click on the COMSOL 3.5a with MATLAB icon. This will initiate a Matlab™ client session followed by COMSOL™. Click OK on the COMSOL™ screen and a new *.mph file will be created. The COMSOL™ with Matlab™ functionality allows COMSOL™ *.mph files to be saved as *.m files that can be directly run in Matlab™.
- In Matlab™, change the workspace to where the cmevmg.rar (*please contact author for the rar file*) file is located and extract the files to the workspace.

- When using VMGSim™ for the first time, go to *File → New Project* to open a new project. Click on *Tools → Options*, and then on *Visio PFD* under *Configuration*. Set the *Visio Version* to the version that you have installed and close the program.
- Open the VMGSim™ file entitled *CPR.vmp* in the workspace. This will open up a Process Flow Diagram (PFD) and a corresponding embedded Excel™ worksheet for the Catalytic Plate Reactor (CPR) Excel™ Unit Operation (EUO) example. As seen in the PFD, the CPR is categorized by the EUO as well as a set of four streams, two of which represent a hot flue gas being cooled and the second two being a cold fuel/steam mixture being heated and reformed to hydrogen. Also note that a new Matlab™ Automation Server (AS) window is opened alongside the vmp file and is associated with the spreadsheet.
- In the associated spreadsheet, the cells under the columns *Inputs* and *Outputs* initially have unsolved Matlab™ formulas. Press CTRL+ALT+F9 in the *unitop* tab to activate the VMGSim™ spreadsheet for data transfer with Matlab™. This will do a forced recalculation of all formulas in the worksheet and thus all cells containing Matlab™ formulas should also be reevaluated. Additionally, click on *Verify Links* in the VMGSim™ file EUO (will need to double-click on the EUO for this), as this will ensure that data transfer between the PFD and the spreadsheet is activated.

- In the Matlab™ client session command window, first run the setup.m script. This will allow the client to get a handle on the running instance of the Matlab™ AS. The configuration allows the client to send and retrieve data from the server workspace. To check if the server is running, type in the AS window:

  » enableservice('AutomationServer')

  An answer of 1 indicates the service is enabled.

- Run run.m in the Matlab™ client. The m-file script runs continuously unless it is terminated by the user. In the script, the VMGSim™ material stream input values to the CPR (flow rate, temperature and pressure) are continuously retrieved from the AS and compared with the original values. If the material stream input values are modified in VMGSim™, the COMSOL™ m-file script is trigged in the run.m script using the new input values. The 2D model is solved.

- Once the model has finished solving, the averaged output values of flow rate, pressure and temperature are sent back to the AS and finally to the VMGSim™ PFD.

- The additional information below explains the modifications to the CPR.m example file that is automatically generated in COMSOL™. To save the 2D model in COMSOL™ as an m-file, go to *File → Save As* after opening the original *.mph file with the *COMSOL with Matlab* icon.

Modifications to CPR.m

Reading CPR unit operation material stream input values from Matlab™ AS

Using the Spreadsheet Link EX function, *MLPutMatrix* (see the Mathworks website for further information), values are first placed into the AS workspace directly from the Excel™ spreadsheet. Similarly, values are retrieved by the Excel™ spreadsheet from the AS workspace, via the *MLGetMatrix* function. In the Matlab™ client, the values are retrieved from the AS using the *GetWorkspaceData* command and converted into strings. varname is the variable name and unit is the associated unit for the variable, ie [K] for temperature variable. varindex is the variable index in the fem.const cell array. hl is the handle on the server instance:

```
% Get a handle on the server instance from the Matlab™ client session
hl = actxGetRunningServer('matlab.application');
% Retrieve input values for fem.const
z = hl.GetWorkspaceData('varname','base');
var = mat2str(z);
fem.const { varindex } = [var,'unit'];
```

The fem.const cell array contains a list of constants (constant values and units) in the CPR model. The constants required as input values from VMGSim™ and retrieved from the AS are defined in the fem.const cell array as follows:

```
fem.const = { .....
 'varname','[]', .....
……};
```

Computing average properties at the outlet

The CPR m-file uses the following to determine the average properties at the outlet boundary of the 2D domain. A post-processing plot of the boundary is generated from the m-file, after which the script below retrieves the resulting data to compute the average value of the property.

```
% Load libraries required for generating figure
figure;
% Get handle on figure
h = gcf;
 % Finds all lines in the figure window
line = findall(h, 'Type', 'Line');
% Extract X and Y data values from the first line:
x_line1 = get(line(1), 'xdata');
y_line2 = get(line(1), 'ydata');
 % Store as matrix and compute average surface property
matrixdata = [x_line1;y_line2];
matrixdata(:,isnan(matrixdata(1,:)))=[];
result = unique(matrixdata','rows');
```

```
averagex = mean(result);

avg = averagex(1,2);

% Write values to Matlab™ AS workspace

hl.PutWorkspaceData('varname','base',avg);
```

Forced recalculation of the worksheet

Once the averaged output property values are exported to the Matlab™ AS, the spreadsheet is not automatically updated with the new output values. A forced recalculation of the worksheet is, therefore, required (equivalent of the manual operation CTRL+ALT+F9 on the worksheet). hdl is the handle on Excel™ worksheet and is defined at the beginning of the of the script. The forced recalculation proceeds after the output property values have been exported to the AS.

```
% Get handle to the open Excel™

hdl, = actxGetRunningServer('Excel.Application');

hdl.Application.CalculateFull;
```

setup.m

```
% Run and Enable Matlab™ Automation Server (AS)

as = actxserver('matlab.application');

% Get a handle on the server instance from the Matlab™ client session

hl = actxGetRunningServer('matlab.application');
```

run.m

```
% Retrieve current workspace variables from AS
z = hl.GetWorkspaceData(' varname ','base');
varname _current = mat2str(z);
while(1==1)
 % no_of_seconds or number of seconds
  excel_pause = no_of_seconds;
  pause(excel_pause);
  % Fetch new modified data from AS
  z = hl.GetWorkspaceData(' varname','base');
  varname = mat2str(z);
  n= no_of_seconds;
  if(strcmp(varname _current, varname)==0)
      pause(n);
      break;
  end
end
CPR;
run;
```